Mesoscopic simulations of electrohydrodynamic phenomena

Dissertation

zur Erlangung des Doktorgrades

vorgelegt von

Jens Smiatek
Theorie der Kondensierten Materie
Fakultät für Physik
Universität Bielefeld

begutachtet durch

Prof. Dr. Friederike Schmid
Prof. Dr. Peter Reimann

vorgelegt am

28. Januar 2009

Gedruckt auf alterungsbeständigen Papier gemäss ISO 9706.

Was ist ist
Was nicht ist ist möglich

- Blixa Bargeld (1996)

Zusammenfassung

Mesoskopische Simulationsmethoden erlauben die numerische Berechnung des dynamischen Verhaltens eines Systems auf langen Zeit- und grossen Längenskalen. Insbesondere bei der Simulation von Phänomenen in der Mikrofluidik finden diese Methoden vielfache Anwendungsmöglichkeiten, da sie die hydrodynamischen Eigenschaften des Systems korrekt reproduzieren. Der Schwerpunkt dieser Arbeit liegt auf der Simulation von elektrohydrodynamischen Phänomen in Mikro-Kanälen mittels der Dissipative Particle Dynamics (DPD) Methode. Da Mikro-Kanäle sich durch ein grosses Oberflächen zu Volumen-Verhältnis auszeichnen, stellt hierbei die korrekte Beschreibung und Charakterisierung der hydrodynamischen Randbedingungen einen wichtigen Aspekt dar. Hierzu wird eine neue Methode, die Tunable-Slip Boundaries präsentiert, welche ermöglicht, effektive Randbedingungen bei hydrodynamischen Flussprofilen zu simulieren. Innerhalb dieses Ansatzes kann eine analytische Theorie entwickelt werden, die erlaubt, die grundlegenden Parameter der Slip length und der Position der hydrodynamischen Randbedingungen zu berechnen und damit vorhersagen zu können. Verschiedene Oberflächen können somit durch gezieltes Einstellen dieser Parameter modelliert werden.
Elektrohydrodynamische Phänomene treten insbesondere bei der Simulation des elektroosmostischen Flusses in den Vordergrund. Auf der Mikroskala stellen diese eine einfache experimentelle Möglichkeit dar, Flussprofile durch Anlegen eines äusseren elektrischen Feldes zu erzeugen. Auf die Simulation und Charakterisierung des elektroosmotischen Flusses wird detailliert eingegangen. Analytische Gleichungen unter Berücksichtigung von verschiedenen hydrodynamischen Randbedingungen werden präsentiert und mit den numerischen Resultaten verglichen. Die Ergebnisse werden zusätzlich mit den Resultaten der Lattice-Boltzmann Methode ergänzt, welche eine weitere mesoskopische Simulationstechnik darstellt. Es wird ein generelles Schema aufgezeigt, welches erlaubt, vergleichbare Flussprofile in beiden Simulationsmethoden zu erzeugen. Die Simulationen werden dabei in verschiedenen elektrostatischen Regimes durchgeführt, wobei die Ergebnisse eine gute Übereinstimmung mit den Standardtheorien aufweisen und der Einfluss der elektrostatischen Reibung gering ist.
Weiterhin wird die Dynamik von Polyelektrolyten in freier Salzlösung untersucht. Hierbei wird ein Übergang zwischen verschiedenen dynamischen Regimes beobachtet, welcher bisher in dieser Form noch nicht vorhergesagt worden ist. Die Ergebnisse zeigen, dass der Übergang rein elektrostatischer Natur ist und daher bei einem ungeladenen Polymer nicht zu beobachten ist. Die Charakterisierung und Erläuterung dieses Effektes beschliessen das Kapitel über Polyelektrolyte in freier salziger Lösung.
Zusätzlich werden die verschiedenen Erkenntnisse und Methoden zur Simulation von Polyelektrolyten in Mikrokanälen unter dem Einfluss äusserer elektrischer Felder kombiniert. Hierbei wird deutlich, dass der elektroosmotische Fluss massive Auswirkungen auf die Dynamik und die Migration des Polyelektrolyten hat. In Anwesenheit bestimmter Randbedingungen kann dieser Effekt so stark werden, dass eine negative Mobilität des Polyelektrolyten, durch Kombination von elektrophoretischer und elektroosmotischer Mobilität, entgegen der angelegten Kraft erzielt wird.

Contents

1 Introduction

How much there is to see - Just open your eyes.
- Eric Bazilian (1987)

It has been known for a long time that organic molecules form the atomistic fundaments of life [1]. Natural macromolecules like Deoxyribonucleic acid (DNA), Ribonucleic acid (RNA) and proteins fulfill different functions like transport of oxygene, storing the genetic code and steering of various cell mechanisms. The interdisciplinary research of chemists, physicists and microbiologists has lead to a deeper insight into these functions and the involved macromolecules with all their fascinating characteristics. The broad variability of macromolecular properties further motivates the industry to exploit these features in technical products by synthesis of novel designed molecules.
Natural rubber has been known for a long time but it was a long way to synthesise the first macromolecules like nylon, polyvinyl chloride or polyethylene. The surplus of synthetic molecules in the modern world for such different objects like packaging material, prostheses, chewing gum or body armors even demonstrates the usage of the often applied synonym *plastic age*.
By investigating the atomistic details, it turns out that a macromolecule, also called polymer, is a molecular chain composed of many repeated structural units connected by covalent chemical bonds. These structural units are called monomers which are in many cases derivates of alkene or benzene for simple polymers like polyethylene or polystyrene [2]. The connection of monomers is realised by covalent binding and the process of subchain connection is called polymerisation or polycondensation. If the polymer is charged, for example by ionic sidegroups or gets charged in solution by dissociation, the macromolecule is called polyelectrolyte or polyion. Many biological polymers are highly charged, DNA and RNA being the most famous and fundamental ones. The behaviour of polyelectrolytes is in many cases different from that of the uncharged counterparts and offers a broad variety in physical properties.
The enormous progress in the development of modern computer technologies has helped to clarify open questions on static and dynamic properties of polymers. A complete new research method with computer simulations has been added to the traditional theoretical and experimental research. Due to these new techniques, more insight is gained into physical problems in all research areas ranging from particle to solid state physics. Especially in problems related to dynamical aspects, computer simulations are powerful tools to investigate basic principles.
The dynamical behaviour of polymers is often a highly debated topic. Many experimental methods like gel electrophoresis rely on the specific interactions of the macromolecule with the environment. The main goal of these techniques is to separate different frag-

ments by their length for sequencing or manipulating them. Recent success in clarifying the sequence of the genome would have not been possible without gel electrophoresis. Although the basic mechanisms are well understood, much scientific effort has been spent to develop novel separation methods, for example in microfluidic devices which are in some cases more favourable than standard techniques [1]. Recent reaseach focusses therefore on the applicability of aqueous buffer solutions in microfluidic arrays.
Novel methods are microchannels with specially formed obstacles or microstructured surfaces which separate polyelectrolytes due to steric hindrance [1]. It is clear that these objects have to be in the same length scale as the macromolecule which means in the micro- or nanometer scale. The naive way of separating polyelectrolytes in free salt solution electrophoresis is not possible due to the fact that the electrophoretic mobility becomes length independent for long chains [1, 3, 4].
Several modern efficient separation methods are therefore realised to overcome this situation, which all have in common the usage of external electric fields to drive the polyelectrolyte through the environment. Mesoscopic simulation methods have helped to clarify the dynamical behaviour and therefore to develop novel devices. The long time and length scale which is accessible and the inherent hydrodynamic characteristics of these methods are the main reasons for the broad applicability in scientific numerical research [5]. A popular mesoscopic method is Dissipative Particle Dynamics (DPD) which is used in this work.
Whereas the dynamical behaviour of polyelectrolytes in free solution electrophoresis is mainly understood [1], the presence of boundaries alters the whole dynamics of the macromolecule drastically. Recent experimental work has been published, where polyelectrolyte dynamics in microchannels in the presence of electroosmotic effects show an unexpected behaviour [6]. For those reasons, a detailed treatment of electrohydrodynamic interactions in modern simulations has to be included, although indeed it is often neglected.
The main goal of this work focusses on the investigation of the explicit coupling of electrohydrodynamic effects in the micrometer scale in confined geometries as well as for polyelectrolytes in free salt solution. Fig. 1.1 shows a schematic illustration of the working plan and the different stages that have to be combined. A main topic is the modelling of a microchannel in the presence of electrohydrodynamic boundary effects.
The simulation methods will briefly be introduced in the next chapter. The third chapter focusses on hydrodynamic boundary conditions in the micrometer scale. An approach of modelling arbitrary boundary characteristics in a mesoscopic simulation method is presented. Within this approach, it is possible to derive an analytic theory for the boundary parameters.
The simulation and analysis of the counterion-induced electroosmotic flow as a main electrokinetic transport phenomenon is presented in the fourth chapter. Together with the corresponding applied hydrodynamic boundary conditions, several effects on the flow profiles as well as different electrostatic coupling regimes are investigated. An analytical theory for the counterion-induced electroosmotic flow for different boundary conditions in the weak-coupling regime is presented. Furthermore Lattice-Boltzmann simulation results from Dr. Marcello Sega at the FIAS Frankfurt, are compared to the results ob-

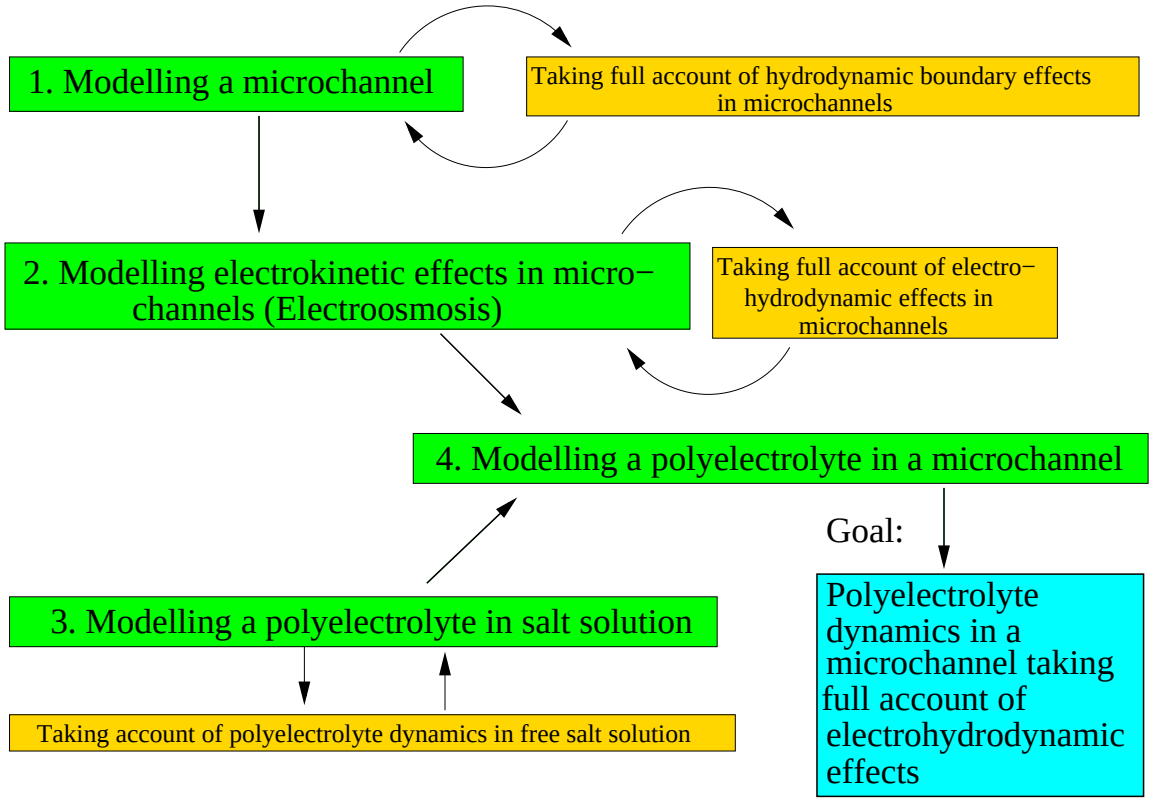

Figure 1.1: Schematic illustration of the working plan.

tained with the Dissipative Particle Dynamics method. A general mapping scheme of both methods is introduced.
The fifth chapter considers polyelectrolyte dynamics in free salt solution. Numerical results evidence that polyelectrolyte dynamics in absence of external electric fields differ from the predicted behaviour on a certain time and length scale. A tentative explanation of this effect is presented.
The results for polyelectrolyte electrophoresis in small microchannels are presented in the last chapter in analogy to the experiments published by Mathé *et al.* in [6]. The drastic influence of the electroosmotic flow on the total polyelectrolyte mobility is investigated in detail. An outlook of possible future work is presented in the conclusions.

2 Simulation methods

Fighting off the diseased programming.
- Serj Tankian (2001)

The basic mesoscopic simulation methods are introduced in this chapter. In addition to Dissipative Particle Dynamics (DPD), the simulation techniques of Langevin Dynamics and Lattice-Boltzmann method are presented in a brief section due to their additional appearance in this work. The Langevin equation is the basis of the tunable-slip boundaries approach which is presented in chapter 3, whereas the results of Lattice-Boltzmann simulations are compared to the results of DPD simulations in chapter 4. Furthermore the framework of electrostatic m-body solvers is shown. This chapter closes with a brief introduction into the software simulation package ESPResSo.

2.1 Mesoscopic simulation methods

The dynamical behaviour of soft matter systems like polymers in solution, colloidal suspensions or microemulsions is strongly influenced by hydrodynamic interactions. The explicit dynamical behaviour of the solvent is not of interest as it typically occurs on a shorter time scale compared to the dynamics of the macroobject [7]. Bridging this time- and length scale gap lead to the development of Brownian Dynamics simulations (BD) with the main drawback that hydrodynamic interactions are neglected. Taking these interactions into account within BD simulations [8] remains computationally unsatisfying, due to the long range $(1/r)$-decay of the Rotne-Prager-Tensor [9, 10]. Efficient coarse-grained model schemes of the liquid, so called mesoscopic simulation approaches have been invented in the last decades to overcome this situation.
Several methods like Lattice Gas Automata [11], Lattice-Boltzmann method (LB) [12, 13, 14], Dissipative Particle Dynamics (DPD) [15, 16, 17, 18] and Multi-Particle Collision Dynamics (MPC) [19, 20] are used to model the solvent in a coarse-grained fashion. In contrast to all-atom Molecular Dynamics simulations these approaches give access to much longer time- and length scales [5] and are therefore preferable to simulate a system's long-time behaviour.
Although the theoretical background of these methods is well understood, the lattice and off-lattice and thermal/athermal character impedes a general straightforward mapping between them. Comparable results of specific soft matter problems obtained by different simulation methods are therefore scarce.

2.2 Dissipative Particle Dynamics (DPD)

Dissipative Particle Dynamics (DPD) was originally developed by Hoogerbrugge and Koelman [15, 16] as a combination of Lattice Gas Automata characteristics and Molecular Dynamics methods. Compared to atomistic Molecular Dynamics simulations, this method gives access to much longer time- and length scales and is therefore suited to study the long-time behaviour of soft matter systems and transport phenomena. It is coarse-grained, momentum-conserving, Galilean invariant and creates a well-defined canonical ensemble.
The basic DPD equations are given by the forces on one particle, which involve two-particle interactions that are given by

$$\vec{F}_i^{DPD} = \sum_{i \neq j} \vec{F}_{ij}^C + \vec{F}_{ij}^D + \vec{F}_{ij}^R \tag{2.1}$$

with the conservative force $\vec{F}_{ij}^C$

$$\vec{F}_{ij}^C = -\vec{\nabla}_{ij} U_{ij}(r_{ij}), \tag{2.2}$$

which is often of the form [18]

$$\vec{F}_{ij}^C = a_{ij} \left(1 - \frac{r_{ij}}{r_c^c}\right) \cdot \hat{r}_{ij} \tag{2.3}$$

with the repulsion parameter a_{ij}, the cutoff radius r_c^c and the distance r_{ij} between interacting particles. The dissipative force $\vec{F}_{ij}^D$ reads

$$\vec{F}_{ij}^D = -\gamma_{DPD} \omega_D(r_{ij})(\hat{r}_{ij} \cdot \vec{v}_{ij})\hat{r}_{ij} \tag{2.4}$$

with the friction coefficient γ_{DPD}, whereas the additional random force $\vec{F}_{ij}^R$ is given by

$$\vec{F}_{ij}^R = \sigma \omega_R(r_{ij}) \check{\zeta}_{ij} \hat{r}_{ij}. \tag{2.5}$$

with the weighting function

$$\omega_D(r_{ij}) = [\omega_R(r_{ij})]^2 \equiv \omega_{DPD}(r_{ij}) \tag{2.6}$$

as a necessary relation for a well-defined canonical ensemble [17, 18]. The symmetric random number $\check{\zeta}_{ij} = \check{\zeta}_{ji}$ with zero mean and unit variance ensures the conservation of momentum and the weighting function is arbitrary and often chosen linear [21]. It depends on the interparticle distance r_{ij} and the cut-off radius r_c. The strength of the interaction is steered by the distance of the particles with

$$\omega_{DPD}(r_{ij}) = \begin{cases} 1 - \frac{r_{ij}}{r_c} & : r_{ij} < r_c \\ 0 & : r_{ij} \geq r_c \end{cases} \tag{2.7}$$

while the amplitude of the Gaussian white noise in Eqn. (2.5) is given by

$$\sigma^2 = 2\gamma_{DPD} k_B T \tag{2.8}$$

with the Boltzmann constant k_B and the temperature T. Eqn. (2.1) can be integrated by an ordinary Molecular Dynamics integration scheme like the Velocity-Verlet algorithm [5] which is used in the ESPResSo package.

2.3 Integration scheme for particle-based simulation methods

In order to simulate a dynamical behaviour, the forces have to be integrated numerically to get access to the updated positions and velocities of the particles. Several sophisticated integration schemes have been presented over the last decades for particle-based methods which differ in their long and short time accuracy [5].
Various requirements have to be fulfilled by a successful integration scheme:

- The exact trajectory of the system should be reproduced as closely as possible
- The algorithm should be symplectic which means that the Liouville equation [22] is fulfilled for Hamiltonian dynamics
- The algorithm should be computationally cheap

One of the most famous algorithms are the Verlet- respectively Velocity-Verlet algorithm which fulfill all these requirements.
The Verlet-algorithm is an iterative scheme

$$\vec{r}_i(t+\delta t) = 2\vec{r}_i(t) - \vec{r}_i(t-\delta t) + \frac{\delta t^2}{m_i}\vec{F}_i(t) + \mathcal{O}(\delta t^4) \tag{2.9}$$

with the particle positions $\vec{r}_i$, the timestep δt, mass m_i and forces $\vec{F}_i$. Considering the dynamical behaviour, it is also possible to compute the velocity

$$\vec{v}_i(t) = \frac{\vec{r}_i(t+\delta t) - \vec{r}_i(t-\delta t)}{2\delta t} + \mathcal{O}(\delta t^2) \tag{2.10}$$

which allows to derive a complete dynamical description of the system.
The DPD simulations presented in this work are integrated by using the Velocity-Verlet algorithm.
The basic algorithm is

$$\vec{r}_i(t+\delta t) = \vec{r}_i(t) + \delta t\, \vec{v}_i(t) + \frac{\delta t^2}{m_i}\vec{F}_i(t) + \mathcal{O}(\delta t^3) \tag{2.11}$$

with the corresponding velocity

$$\vec{v}_i(t+\delta t) = \vec{v}_i(t) + \frac{\delta t}{2m_i}(\vec{F}_i(t) + \vec{F}_i(t+\delta t)) + \mathcal{O}(\delta t^3). \tag{2.12}$$

Although the presented methods are quite simple, it can be shown that the conservation of phase space density is fulfilled and symplecticity is guaranteed [5].

2.4 Langevin Dynamics

Brownian motion of suspended particles was first observed in the nineteenth century [23, 24, 25]. Paul Langevin derived a phenomenological equation to formerly describe

the motion of colloidal particles in solution. In its natural form, the equation does not include hydrodynamic effects like hydrodynamic interactions.
The Langevin equation reads [24, 25]

$$\vec{F}_i = \vec{F}_i^D + \vec{F}_i^R \tag{2.13}$$

with the stochastic force

$$\vec{F}_i^R = -\gamma_L \vec{v}_i \tag{2.14}$$

and the random force

$$< F_{i\alpha}^R(t) F_{j\beta}^R(t') >= 2\gamma_L k_B T \; \delta_{ij}\delta_{\alpha\beta}\delta(t-t') \tag{2.15}$$

in terms of delta-correlated Gaussian white noise with the average random force $< \vec{F}_i^R(t) >= 0$. The dissipative force is a damping force which describes the effective friction of the particle with the environment, whereas the random force can be seen as the reason for the jiggle-motion, which was primarily observed in Brownian motion. The formal identity to the DPD equation (Eqn. (2.1)) is obvious, whereas the integration of the forces can be achieved in analogy to the DPD method with the Verlet-, respectively the Velocity-Verlet algorithm.

2.5 Lattice-Boltzmann method (LB)

In contrast to DPD the Lattice-Boltzmann method can be seen as a discrete formulation of the Boltzmann equation on a lattice. By means of a Chapman-Enskog expansion, this leads to the Navier-Stokes equation in the incompressible limit [13, 14]. The basic evolution equation for the number of particles $n_i(\vec{r}, t)$ in a volume a^3 on a grid point $\vec{r}$ at time t is given by

$$n_i(\vec{r} + \vec{c}_i a,\, t+\tau) = n_i(\vec{r}, t) + \sum_{j=1} L_{ij}(n_j(\vec{r}, t) - n_j^{eq}(\rho, \vec{u})) \tag{2.16}$$

with the lattice spacing a and the velocities $\vec{c}_i \frac{a}{\tau}$, concerning the time step τ and a vector $\vec{c}_i$ leading to the $i-$th neighbour on the grid with unit lattice constant. The relaxation of n_i in the last term towards the local pseudo equilibrium distribution $n_j^{eq}(\rho, \vec{u})$ is given by the connection to the constant matrix L_{ij} which resembles the Bhatnagar-Gross-Krook (BGK) collision operator [26, 27] in the continuum Boltzmann equation.
The local pseudo equilibrium $n_j^{eq}(\rho, \vec{u})$ depends on the density $\rho(\vec{r}, t) = \sum_i n_i(\vec{r}, t) m/a^3$ as well as on the fluid current $\vec{j}(\vec{r}, t) = \rho\vec{u} = \sum_i n_i(\vec{r}, t)\vec{c}_i m/(\tau a^2)$ with the particle mass m. The functional form for the pseudo-equilibrium distribution is often chosen to

$$n_i^{eq}(\rho, \vec{u}) = \rho(A_q + B_q(\vec{c}_i \cdot \vec{u}) + C_q u^2 + D_q(\vec{c}_i \cdot \vec{u})^2) \tag{2.17}$$

where the constants A_q, B_q, C_q, D_q, which depend on the sublattice q and the magnitude of $\vec{c}_i$ satisfy the correct description of a global macroscopic hydrodynamic behaviour.
Local mass and momentum conservation is guaranteed by coupling fluctuations only to

the fluxes of the conserved variables [26]. The fluctuating Lattice-Boltzmann equation is then given by

$$n_i(\vec{r}+\vec{c}_i a, t+\tau) = n_i(\vec{r},t) + \sum_{j=1} L_{ij}(n_j(\vec{r},t) - n_j^{eq}(\rho,\vec{u})) + n_i'(\vec{r},t) \tag{2.18}$$

with the stochastic term

$$n_i'(\vec{r},t) = -D_q \sum_{\alpha\beta} \sigma'_{\alpha\beta} c_{i\alpha} c_{i\beta} \tag{2.19}$$

and the random stress fluctuation

$$< \sigma'_{\alpha\beta}(\vec{r},t)\sigma'_{\gamma\delta}(\vec{r}',t') >= A\delta_{\vec{r}\vec{r}'} \cdot \delta_{tt'} \left(\delta_{\alpha\gamma}\delta_{\beta\delta} + \delta_{\alpha\delta}\delta_{\beta\gamma} - \frac{2}{3}\delta_{\alpha\beta}\delta_{\gamma\delta} \right) \tag{2.20}$$

which fulfills the fluctuation dissipation relation. The noise strength A reads

$$A = \frac{2\eta_s k_B T \lambda^2}{a^3 \tau} \tag{2.21}$$

with λ as a non-trivial eigenvalue, belonging to the eigenvector $c_{i\alpha}c_{i\beta}$ of the relaxation matrix L_{ij} [28] and the shear viscosity η_s.
A delicate task for lattice-based simulations is the correct coupling between the discrete nodes of the solvent and the continuous positions of the soluted particles. This requirement can be fulfilled by a modified Langevin equation [26, 29]

$$\vec{F}_{fl} = -\zeta_{LB}[\vec{V} - \vec{u}(\vec{R},t)] + \vec{f} \tag{2.22}$$

with a random force $\vec{f}$ and a coupling constant ζ_{LB}. The absolute velocity of the particle $\vec{V}$ in the friction term is substituted by the interpolated velocity relative to the fluid $\vec{V} - \vec{u}(\vec{R},t)$. As always the random force fulfills the fluctuation dissipation relation $< f_\alpha(t) f_\beta(t') >= \sigma_{LB}^2 \delta_{\alpha\beta}\delta(t-t')$ with an amplitude $\sigma_{LB}^2 = 2\zeta_{LB}k_BT$ in terms of white noise.

2.6 Efficient calculation of electrostatic interactions

The calculation of electrostatic interactions is a crucial task in computer simulations. All interactions of charged particles with each other and even its periodic images have to be computed due to the long-range character. If n_c is the number of charged particles, this leads to $\mathcal{O}(n_c^2)$ operations which have to be calculated in one simulation step [30]. The need for effective calculation schemes is therefore obvious.
An efficient calculation scheme is the Ewald-summation technique, which was primarly invented for the study of liquid crystals [30, 31]. A cubic simulation box with volume $V = L^3$ and periodic boundaries, where the charge of one particle is $Z_i e$, is considered. The electrostatic energy for this system is given by

$$\psi = \frac{1}{2} \sum_{i,j=1}^{n_c} \sum_{\vec{n}\in\mathbb{Z}^3} \frac{Z_i e \cdot Z_j e}{|\vec{r}_{ij} + \vec{n}L|} \tag{2.23}$$

due to periodic images at distances nL. As mentioned above, the long-range character $\sim 1/r$ forbids the implementation of a primitive cutoff radius. Ewald splitted this factor in two parts to overcome this situation according to

$$\frac{1}{r} = \frac{f(r)}{r} + \frac{1-f(r)}{r} \tag{2.24}$$

where the function $f(r)$ can be chosen freely. The first part $f(r)/r$ should be negligible for distances larger than a certain cutoff-radius whereas the long-range part $(1-f(r))/r$ is disregarded on the short scale. Thus both terms can be calculated separately. The traditional choice for $f(r)$ is the complementary error function

$$\mathrm{erfc}(\alpha) = \sqrt{\frac{4}{\pi}} \int_{\alpha}^{\infty} dt\ e^{-t^2} \tag{2.25}$$

which allows an efficient and fast calculation procedure [32]. The Fourier transformed charge density for the long range part can then be assigned to a grid by sophisticated methods [33]. The calculation of the short-range part follows Eqn. (2.25).
This method, which is called P3M [5, 33] needs only $\mathcal{O}(n_c \log n_c)$ computations for a timestep, which is a milestep in contrast to $\mathcal{O}(n_c^2)$.
Another approach to effectively compute Eqn. (2.23) is presented in the MMM-family of algorithms [34]. Here the Coulomb sum is transformed in a series of fast decaying functions by use of a convergence factor which can be easily evaluated. The basic equation reads

$$\tilde{\psi} = \frac{1}{2} \lim_{\beta \to 0} \sum_{i,j=1}^{n_c} \sum_{\vec{n} \in \mathbb{Z}^3} \frac{Z_i e \cdot Z_j e}{|\vec{r}_{ij} + \vec{n}L|} e^{-\beta(|\vec{r}_{ij} + \vec{n}L|)} \tag{2.26}$$

which is used in the MMM3D method [34, 35, 36]. Electrostatic interactions in slabwise devices with $2D + h$ geometries can easily be calculated by using MMM2D [37, 38] as well as by the P3M method with an electrostatic layer correction (ELC) [39]. The special case of only one periodic dimension can be caluclated with MMM1D [40, 41]. Detailed comparison and description of the methods can be found in [32].

2.7 The software package ESPResSo

All simulations in this work have been carried out by extensions of the software package ESPResSo (An **E**xtensible **S**imulation **P**ackage for **Res**earch on **So**ft matter) [42, 43, 44]. ESPResSo was mainly developed for coarse-grained mesoscopic simulation approaches. One of the programs advantages is its high performance MPI-parallelisation implemented for simulations on supercomputers. Users can furthermore change and extend the program code to adopt it for their own purposes. ESPResSo incorporates several simulation techniques like Lattice-Boltzmann, Dissipative Particle Dynamics, Stochastic Dynamics as well as pure Molecular Dynamics techniques. Another feature are the several implemented electrostatic algorithms like MMM1D, MMM2D, MMM3D, P3M, ELC and screened Debye-Hückel potentials, which allow to choose between the fastest calculation

methods available. In summary, ESPResSo provides a well founded basis code for high performance computing on parallel clusters. The steering of the simulations is based on a TCL (Tool Command Language) script [45]. For starting a simulation, no explicit knowledge of implementation details is needed. Even newcomers in the methods of computer simulations can succesfully run a simulation after a short time.
Several tools for analysis are additionally included in the program. ESPResSo is under public license and free to download [42]. Users that develop new ideas are invited to submit their source code, written in the programming language C to be incorporated after testing in the newest release version. The development of ESPResSo continues and a number of extensions is already planned.

3 Modelling a microchannel: Tunable-slip boundaries

Slipping on the friction slide.
- Trey Anastasio (1993)

Due to the development of modern microfluidic devices like micro-arrays (Fig. 3.1) and their large applicabilty in such different fields as polymer separation and micromanipulation of macromolecules, the fluid mechanics on these micro- and nano length scales have become of great interest. In the last years much effort has been spent on the simulation of fluid flows in the submicrometer scale to discover even more efficient and simple geometries. Different flow profiles like pressure-driven flows [46] as well as electroosmotic flows [47] have been considered in various numerical studies. A main task in simulating fluid flows is the correct consideration of the boundaries due to the large surface-to-volume ratio. Neglecting the specific chemical properties of the surface, the hydrodynamic boundary conditions can be described by simple but effective equations. In general two main methods are in use. The most famous one, which is mainly used

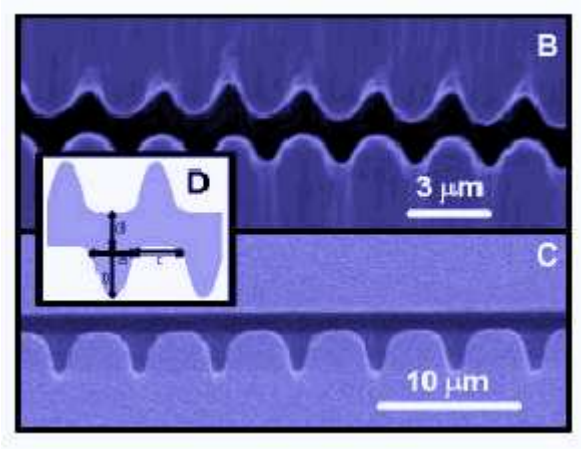

Figure 3.1: Structured microdevice used for polymer separation [48].

in textbooks [49, 50] is the no-slip boundary condition. This condition implies that the fluid velocity $v_x(z)$ totally vanishes

$$v_x(z)|_{z=z_B} = 0 \tag{3.1}$$

at the hydrodynamic boundary positions z_B for a flow profile in x-direction. This equation gives a correct description of almost all macroscopic boundary conditions but it fails in the micrometer scale. Several factors like finite microscopic friction and the conservation of momentum lead to the conclusion that the fluid velocity does indeed not totally vanish, which is called *slippage* [51, 52, 53, 54]. This effect can be described by the consideration of viscous stresses and their equality at the hydrodynamic boundary positions [53].
The viscous stress of the surface σ_{xz}^B exerted by microscopic friction on the fluid particles

$$\sigma_{xz}^B = \zeta_B v_x(z) \tag{3.2}$$

is proportional to an *a priori* unknown boundary friction coefficient ζ_B and the fluid velocity $v_x(z)$. The additional viscous bulk stress arising from the fluid σ_{xz}^F is given by

$$\sigma_{xz}^F = \eta_s \frac{\partial}{\partial z} v_x(z) \tag{3.3}$$

with the shear viscosity η_s. At the hydrodynamic boundaries both viscous stresses have to agree due to the stability condition [50] with $\sigma_{xz}^F|_{z=z_B} = \sigma_{xz}^B|_{z=z_B}$. Combining Eqn. (3.2) and Eqn. (3.3) yields

$$v_x(z)|_{z=z_B} = \delta_B \left(\frac{\partial v_x(z)}{\partial z} \right)_{z=z_B} \tag{3.4}$$

with the slip length

$$\delta_B = \frac{\eta_s}{\zeta_B} \tag{3.5}$$

which, in principle can be hardly calculated due to the unknown wall friction coefficient ζ_B. The *partial-slip boundary condition* (Eqn. (3.4)) further includes the special limit of the no-slip boundary condition for the slip length $\delta_B = 0$. This effective description holds for several applications although it is based on phenomenological equations.
The interpretation of Eqn. (3.4) can be given in terms of a linear extrapolation of the fluid velocity at the boundaries to the point inside the wall, where the velocity vanishes. The distance between this point and the hydrodynamic boundary positions is the slip length δ_B. Fig. 3.2 presents a schematic illustration.
In the last years a number of experimental results have shown [55, 56, 57] that slippage is a present effect on nearly all surfaces at the microscale. With this condition, the Navier-Stokes equation

$$\rho \left(\frac{\partial}{\partial t} + \vec{v} \cdot \vec{\nabla} \right) \vec{v} = \rho \vec{F}^{ext} - \vec{\nabla} P + \eta_s \Delta \vec{v}, \tag{3.6}$$

with mass density ρ, external force $\vec{F}$ and pressure P, which is valid in the bulk incompressible fluid [50] is not applicable in close vicinity to the boundaries. It has to be extended by an effective description due to an additional microscopic friction for this region (*cf.* Fig. 3.2).

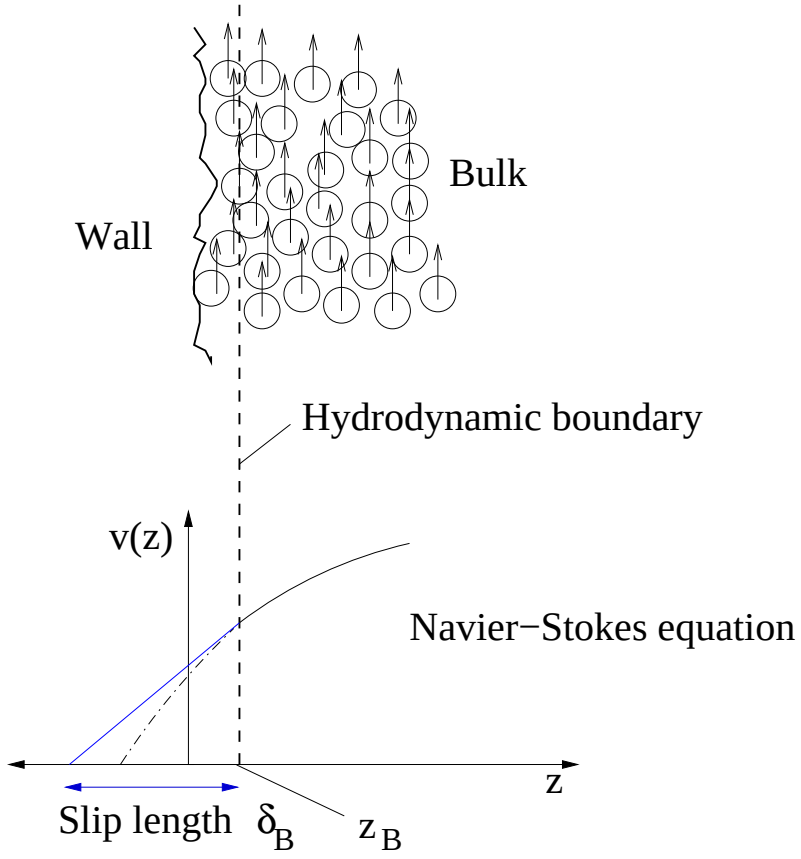

Figure 3.2: **Top:** Coarse-grained schematic illustration of fluid flow in close vicinity to the boundaries. The hydrodynamic boundary is not identical to the fluid-solid interface due to atomistic roughness. **Bottom:** Flow velocity in dependence of the z-position. In close vicinity to the boundary positions, the Navier-Stokes equation is not valid anymore. An extrapolition of the flow profile determines the slip length.

For an experimentalist, it is nearly impossible to determine the hydrodyamic boundaries and the slip length directly because of the unknown boundary characteristics. Much theoretical and numerical work has been published in the last years to investigate the effects of these parameters in detail.
A calculation scheme in terms of a Green-Kubo theory was presented by L. Bocquet and J.-L. Barrat [58]. In addition further detailed Lattice-Boltzmann simulations [59, 60, 61] have lead to a semi-analytic theory which explains the results of recent experiments [62, 63, 64]. Although the simulations were successful, a complete explanation based on physical facts is still missing. The features of hydrophobic and hydrophilic surfaces have additionally shown that the fluid behaviour close to the boundaries is influenced in various ways [65]. Despite the interesting physical mechanisms, this chapter focusses on

an effective implementation of the boundary conditions to derive a fluid-wall slippage behaviour in mesoscopic computer simulations.
Recent publications on computer simulations of microchannel flows focus on boundary conditions in several ways. Implementing microscopic friction on the fluid particles by freezing regions of the fluid [66] is an often used approach. Another approach was published by Pivkin and Karniadakis [67] in 2005. They incorporated fixed particles in the walls to realise a stationary embedded layer around the boundaries. Friction is imparted to the fluid flow by particle collisions of the free liquid with the embedded layer. The walls are modelled by hard repulsive planes in combination with bounce-back boundary conditions.
Bounce-back boundary conditions have been used in lattice based simulation methods for a long time and allow to realise nearly no-slip boundary conditions [68]. This method reverses the normal and the tangential component of the velocity such that the particles are reflected in their original direction. Further reflection methods are given by specular reflection and Maxwellian reflection. Specular reflection reverses the normal component of the velocity and supports slippage whereas Maxwellian reflection reintroduces the particles back into the flow with a random velocity, following a Maxwell-Boltzmann distribution centered around the wall velocity. In addition to the controversal physical interpretation, spurious artefacts like temperature perturbations have been reported for these methods [68, 69].
The approach presented in this chapter offers the possibility to tune the slip length systematically from full- to no-slip. An analytic expression can be derived that allows a detailed calculation of the parameters given in Eqn. (3.4). Parts of this chapter have been published in [70, 71]. The source code of this method has been implemented in the simulation software package ESPResSo which is under public license [42, 43, 44].

3.1 The method of the tunable-slip boundary conditions

The hydrodynamic boundary conditions at the surface result from interactions between the fluid particles and the walls. Depending on the microscopic structure of the wall-fluid interface, these interactions can be quite complex. In the tunable-slip boundary approach, the channel walls are modelled by impermeable surfaces and the unknown atomistic forces are replaced by an effective coarse-grained coordinate-dependent friction force between the fluid particles and the walls, which can be interpreted in terms of a viscous layer. Viscous friction leads to a dissipation of the kinetic energy in this layer and therefore to a decelerated velocity of the fluid particles in close vicinity to the boundaries. The resulting slip length finally depends on the strength of this friction force. With increasing friction strength, the value of the slip length decreases. This idea can be applied very generally to off-lattice as well as lattice-based simulation methods. The friction force is implemented by introducing spatially varying Langevin forces

$$\vec{F}_i^{VL} = \vec{F}_i^{D} + \vec{F}_i^{R}, \tag{3.7}$$

where the dissipative contribution

$$\vec{F}_i^D = -\gamma_L \, \omega_L(z) \; (\vec{v}_i - \vec{v}_{wall}) \tag{3.8}$$

couples to the relative velocity $(\vec{v}_i - \vec{v}_{wall})$ of the particle with respect to the velocity of moving objects, for example channel walls in shear flow. The locally varying 'viscosity' $\gamma_L \omega_L(z)$ depends on the wall-particle distance z_i and the cutoff distance z_c. The weighting function $\omega_L(z)$ is positive for $z_i < z_c$ and zero for $z_i \geq z_c$ with

$$\omega_L(z) = 1 - \frac{z_i}{z_c} \tag{3.9}$$

in a linear dependence. Otherwise, it can be chosen freely. The physical picture implies that the friction increases with respect to the surface. The prefactor γ_L can be used to tune the strength of the friction force and hence the value of the slip length. To preserve global temperature T and to ensure a correct equilibrium distribution, a random force obeying the fluctuation-dissipation relation has to be added,

$$F_{i,\alpha}^R = \sqrt{2\gamma_L \, k_B T \, \omega_L(z)} \, \chi_{i,\alpha} \tag{3.10}$$

with $\alpha = x, y, z$, where k_B is the Boltzmann constant and $\chi_{i,\alpha}$ a Gaussian distributed random variable with mean zero and unit variance. The moments for the random variable are given by $\langle \chi_{i,\alpha} \rangle = 0$ and $\langle \chi_{i,\alpha} \chi_{j,\beta} \rangle = \delta_{ij} \delta_{\alpha\beta}$. Eqn. (3.7) can be used to model interactions with immobile walls, such as channel boundaries, as well as interactions with surfaces of mobile and/or rotating objects, for example colloids.
Eqn. (3.7) is coupled to the inter-particle DPD-forces (Eqn. (2.1)) to give a total force

$$\vec{F}_i = \vec{F}_i^{DPD} + \vec{F}_i^{VL} \tag{3.11}$$

which acts on the particles depending on their relative positions. The forces on a particle outside the viscous layer with $z_i \geq z_c$ are therefore solely given by Eqn. (2.1).
As it has been known for a long time [72], Langevin Dynamics do not conserve momentum. In close vicinity to the channel walls, the Stokes equation is not valid anymore such that the particle's momentum is transferred to the viscous layer. This means that only the bulk region has to be considered for hydrodynamic calculations of flow profiles whereas the region inside the layer has to be disregarded. Therefore the range of the layer has to be small compared to the diameter of the channel for studying a correct global hydrodynamic behaviour.

3.2 The simulation model

Periodic boundary conditions are in use for the $x-$ and the $y-$direction. The $z-$direction is confined by two impermeable surfaces which act on the particles by a purely repulsive Lennard-Jones(LJ)-potential [73] of the form

$$U_{ij} = 4\epsilon \left[\left(\frac{\sigma}{r} \right)^{12} - \left(\frac{\sigma}{r} \right)^{6} \right] \tag{3.12}$$

with one molecular diameter σ and the energy parameter ϵ. The natural units in the simulation are $\sigma = 1$, $\epsilon = 1$ and the mass is set to unity $m = 1$. The cutoff length r_c^r of the repulsive potential in Eqn. (3.12) is 1.0σ and the z-width L of the box is 10σ. The cutoff length z_c for the viscous layer is set to 2.0σ, the cutoff-length of the DPD interactions r_c is fixed to 1.0σ. There are no interparticle conservative forces in the DPD-Fluid such that an ideal gas is simulated. In all simulations the timestep δt is set to $0.01\sigma(m/\epsilon)^{1/2}$. The number density ρ and the friction coefficients γ_{DPD} and γ_L vary. A schematic illustration of the system is shown in Fig. 3.3.

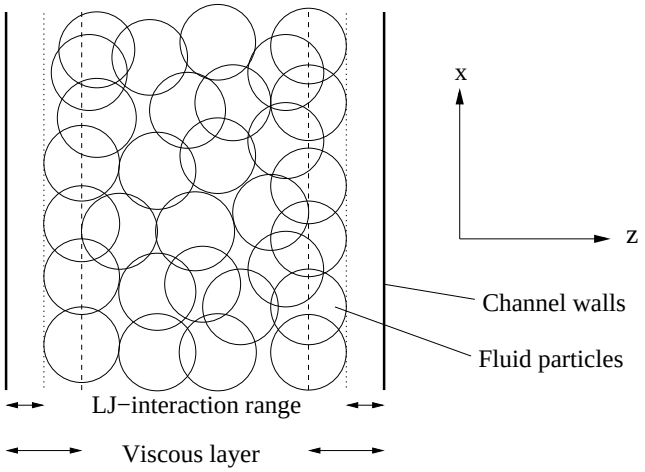

Figure 3.3: Illustration of the simulation system.

3.3 Test case: Plane Poiseuille and Plane Couette Flow

The model was tested by two special cases, namely the Plane Poiseuille (PPF) and the Plane Couette Flow (PCF) [49, 50]. At low Reynolds number, the basic Navier-Stokes equations (Eqn. (3.6)) for a non-turbulent Newtonian incompressible fluid can be reduced to the Stokes equation [50]

$$\eta_s \Delta \vec{v} = -\rho \vec{F}^{ext} \tag{3.13}$$

with the external force $\vec{F}^{ext}$ in absence of pressure gradients. The Plane Poiseuille Flow results from the application of an external force or a hydrostatic pressure gradient on the confined fluid. Integration of the Stokes equation and application of the partial-slip boundary conditions of Eqn. (3.4) yields

$$v_x(z) = \frac{\rho F_x^{ext}}{2\eta_s}(z_B^2 - z^2 + 2\delta_B|z_B|) \tag{3.14}$$

for the flow profile in $z-$direction in presence of the external force F_x^{ext}, which is schematically presented on the left side of Fig. 3.4. The flow profile for the special case of no-slip

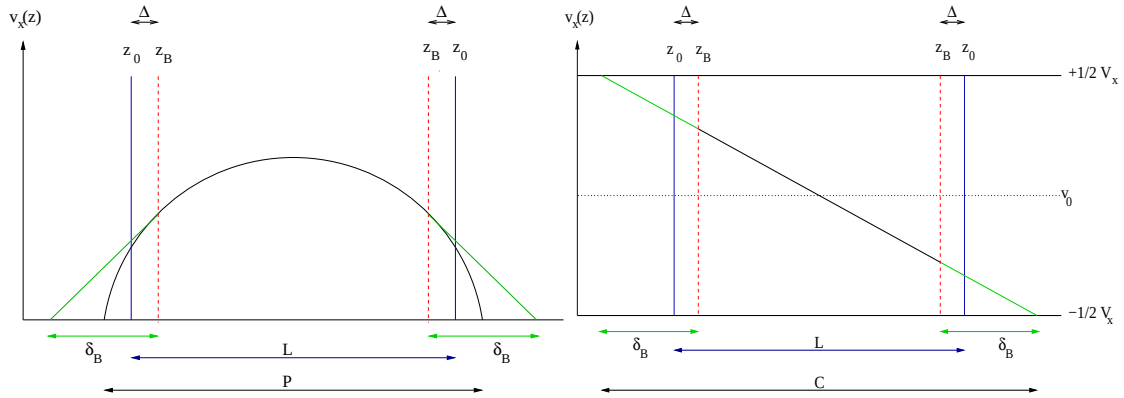

Figure 3.4: **Left:** The flow profile $v_x(z)$ of the Plane Poiseuille Flow is presented with the hydrodynamic boundaries z_B, the position of the physical walls z_0, the slip length δ_B, the width of the channel L, the width of the parabolic flow profile P and Δ as the distance between the hydrodynamic boundary positions and the physical walls. **Right:** The profile $v_x(z)$ of the Plane Couette Flow is shown in dependence of the boundary velocity difference V_x and the width of the linear flow profile C.

boundary conditions is given by $\delta_B = 0$. In absence of external forces or pressure gradients but with moving boundaries, a Plane Couette Flow (PCF) in the fluid can be induced. The Stokes equation for the PCF is given by

$$\eta_s \Delta \vec{v} = 0 \tag{3.15}$$

with the modified partial-slip boundary conditions

$$\frac{1}{2} V_x \mp v_x(z)|_{z=\pm z_B} = \delta_B \frac{\partial}{\partial z} v_x(z)|_{z=\pm z_B} \tag{3.16}$$

in dependence of the surface velocity difference V_x. Integrating the Stokes equation twice with respect to the boundary conditions, the flow profile of the PCF reads

$$v_x(z) = \frac{z V_x}{2(|z_B| + \delta_B)} \tag{3.17}$$

where the characteristic linear flow profile, depending on the system parameters is presented on the right side of Fig. 3.4. To verify the tunable-slip boundaries approach of section 3.1, both flow profiles can be seen as ideal test cases due to their analytical solubility.

3.4 Fluid density and flow profiles

An important criterion for a correct simulation of the flow profiles is a constant density. The left side of Fig. 3.5 presents an exemplary fluid density profile for $\rho = 3.75\sigma^{-3}$ with

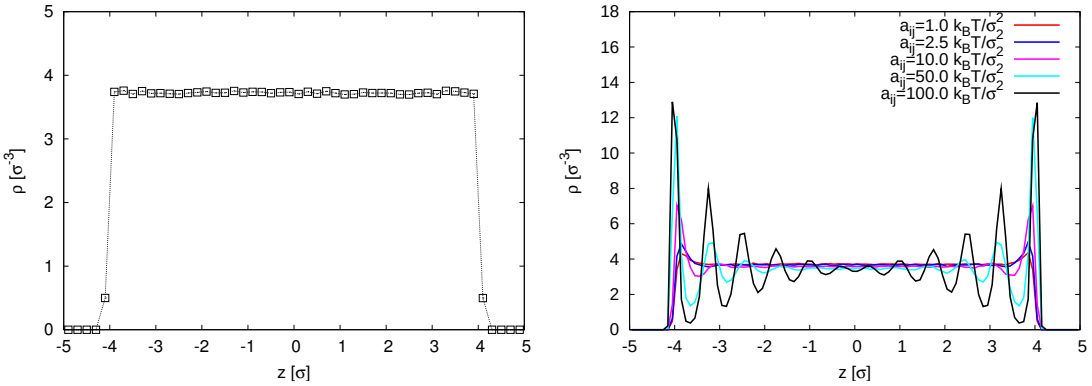

Figure 3.5: **Left:** Exemplary fluid density profile with $\rho = 3.75\sigma^{-3}$ in presence of tunable slip boundaries. The fluid density is nearly constant all over the channel. The deviations are explained in the text. **Right:** Fluid density profile with $\rho = 3.75\sigma^{-3}$ and conservative interactions (Eqn. (2.3)) with varying repulsion parameter a_{ij} and cutoff radius $r_c^c = 1.0\sigma$.

tunable-slip boundary interactions in absence of onservative interparticle forces. The fluid density is constant over the channel although fluctuations can be observed. Small deviations are obvious at $|z| \approx 4.0\sigma$ due to the finite character of the repulsive interactions of the wall on the fluid particles. The range of the interactions with 1.0σ leads to an effective wall position at $z_0 = 4.0\sigma$.
Although the particles are simulated as an ideal gas, the influence of conservative interparticle forces is of main interest. An often used soft conservative phenomenological force for DPD simulations is given by Eqn. (2.3). As the right side of Fig. 3.5 shows, the demand of a constant density is perturbed due to the presence of conservative interparticle interactions with increasing a_{ij}. The particles form distinct layers inside the channel. In all simulation runs, conservative forces between the fluid particles are therefore neglected as long as not otherwise stated.
Further influence of the conservative force on the shear viscosity and the hydrodynamic boundary conditions will be investigated in detail in the future [75]. The corresponding preliminary flow profiles are presented in appendix D.
The left side of Fig. 3.6 presents a simulated normalised Plane Poiseuille Flow profile in absence of conservative interparticle interactions. The dashed line shows a parabolic fit with $f(z) = a \cdot (z^2 - (P/2)^2)$ adopted from Eqn. (3.14). Deviations can be seen at $|z| \approx 4.0\sigma$ due to the diminished density in coincidence to Fig. 3.5 and the presence of the viscous layer. On the right side of Fig. 3.6 an exemplary flow profile for a simulated Plane Couette Flow is shown. Identical parameter sets as for the Plane Poiseuille Flow have been used. At $z \approx 4.0\sigma$, the boundary requirements for a fluid-solid surface $\partial_z v_x(z_0) = 0$ [50] are fulfilled and no drastic deviations are obvious. The dashed line shows a linear fit of the form $f(x) = m \cdot z$ in correspondence to Eqn. (3.17). In sum-

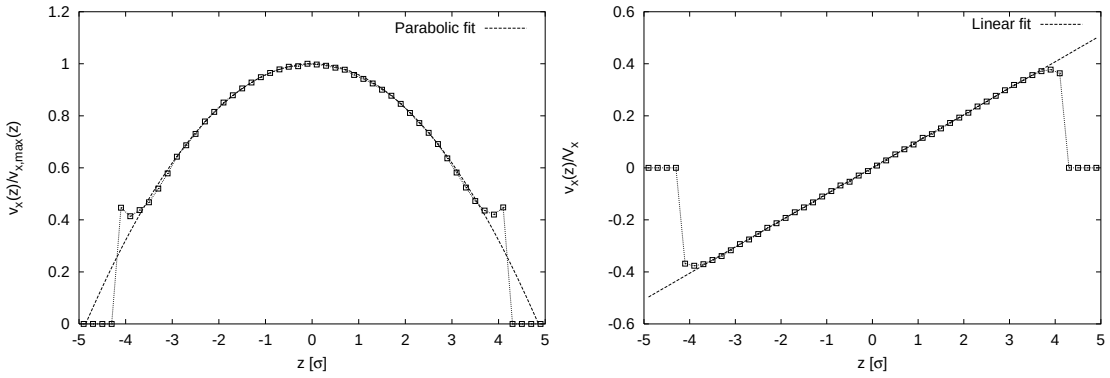

Figure 3.6: **Left:** Exemplary velocity flow profile for a normalised Plane Poiseuille Flow with $\rho = 3.75\sigma^{-3}$, $\gamma_{DPD} = 5.0(m\epsilon)^{1/2}/\sigma$ and tunable slip friction coefficient $\gamma_L = 1.0(m\epsilon)^{1/2}/\sigma$. The dashed line shows a fit to the theoretical profile. **Right:** Exemplary velocity flow profile for a normalised Plane Couette Flow with $\rho = 3.75\sigma^{-3}$, $\gamma_{DPD} = 5.0(m\epsilon)^{1/2}/\sigma$ and tunable slip friction coefficient $\gamma_L = 1.0(m\epsilon)^{1/2}/\sigma$. The dashed line shows a fit to the theoretical profile.

mary, the model of the tunable-slip boundaries produces correct results for the Plane Couette and the Plane Poiseuille Flow. No deviations for varying parameter sets have been observed for all simulated flow profiles.

3.5 Shear viscosity

An important parameter for characterising the properties of the fluid is the shear or dynamic viscosity η_s. In contrast to the Lattice-Boltzmann method, the shear viscosity is a derived parameter in DPD simulations which can be hardly tuned. For a determination of η_s, a Green-Kubo expression

$$\eta_s = \frac{V}{k_B T} \int_{t_0}^{\infty} dt < \mathcal{P}_{\alpha\beta}(t)\ \mathcal{P}_{\alpha\beta}(t_0) > \tag{3.18}$$

with the components of the pressure tensor $\mathcal{P}_{\alpha\beta}$ and the volume V can be evaluated [30]. Another possibility is measuring the amplitude $\alpha = \rho F_x^{ext}/2\eta_s$ of the Plane Poiseuille Flow (Eqn. (3.14)). By fitting the flow profile, the shear viscosity η_s can be determined to

$$\eta_s = \frac{\rho F_x^{ext}}{2\alpha} \tag{3.19}$$

with the flow magnitude α, which can be evaluated easily.
Theoretical considerations about the shear viscosity in Dissipative Particle Dynamics are based on a sophisticated mean-field approach [76], or on the other hand by a simple derivation, which is based on the direct calculation of the corresponding shear stresses

[18, 77]. The shear viscosity calculated by the different force contributions is then given by [18]

$$\begin{aligned} \eta_s &= \eta_K + \eta_D \\ &= \frac{45}{4\pi}\frac{k_B T}{\gamma_{DPD} r_c^3} + \frac{2\pi}{1575}\rho^2 \gamma_{DPD} r_c^5 \end{aligned} \tag{3.20}$$

which can be compared to the numerical results.
The first term η_K is given due kinetic contributions whereas the second term η_D corresponds to the dissipative momentum transfer contributions inside the fluid. Although it has been reported [78], that Eqn. (3.20) is in rough agreement to the numerical results for moderate parameter values, deviations have been observed between the proposed measuring methods in the simulations of this work. The pressure tensor autocorrelation function is shown on the left side of Fig. 3.7 for a fluid density $\rho = 3.75\sigma^{-3}$ with friction coefficient $\gamma_{DPD} = 5.0(m\epsilon)^{1/2}/\sigma$.
Eqn. (3.18) yields a value of $\eta_s = (1.0366 \pm 0.0013)\sigma^{-2}\sqrt{m\epsilon}$ in agreement to Eqn. (3.20), which gives a calculated shear viscosity of $\eta_s = 0.9967\sigma^{-2}\sqrt{m\epsilon}$.
Determining the shear viscosity for identical parameter sets by the flow profile method and evaluation of Eqn. (3.19), produces results around $\eta_s \approx 1.34\sigma^{-2}\sqrt{m\epsilon}$ for varying forces $F_x = 0.01 - 0.1\epsilon/\sigma$, which are presented on the right side of Fig. 3.7. The shear

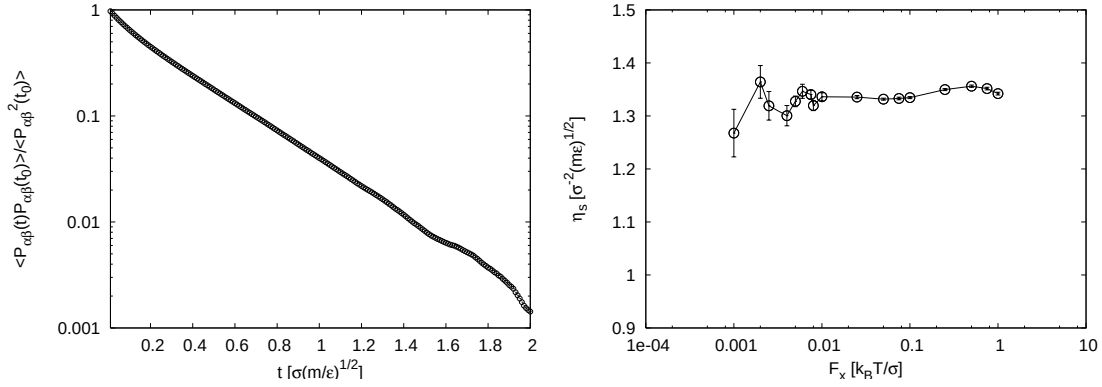

Figure 3.7: **Left:** Green-Kubo relation of the shear viscosity for a fluid density $\rho = 3.75\sigma^{-3}$ and friction coefficient $\gamma_{DPD} = 5.0(m\epsilon)^{1/2}/\sigma$. The autocorrelation function yields a value of $\eta_s = (1.0366 \pm 0.0013)\sigma^{-2}\sqrt{m\epsilon}$. **Right:** Shear viscosities for a density $\rho = 3.75\sigma^{-3}$ with $\gamma_{DPD} = 5.0(m\epsilon)^{1/2}/\sigma$ for varying external forces.

viscosity shows no obvious dependence on the external force which means that the discrepancy can apparently not be explained by finite deviations from the linear response result of Eqn. (3.18). It is obvious that the shear viscosity follows no strict behaviour at low force strengths. Further investigation of this effect has to be undertaken to clarify the differences. For all following simulation results, the shear viscosity has been calculated by Eqn. (3.19) for consistency due to the fact, that solely dynamical profiles are

of interest in this work. Further influence of the friction coefficient γ_{DPD} and the fluid density ρ on the shear viscosity in comparison to Eqn. (3.20) is presented in Fig. 3.8. Although the results are not exactly in agreement to the theory, the predicted behaviour

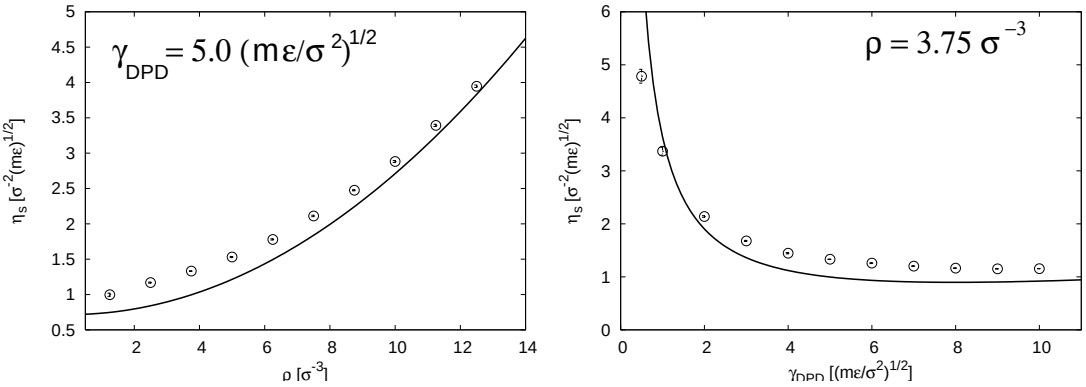

Figure 3.8: Shear viscosity η_s for varying fluid densities ρ and varying friction coefficientes γ_{DPD} in comparison to Eqn. (3.20) (black line). **Left:** Shear viscosity for fixed friction coefficient $\gamma_{DPD} = 5.0(m\epsilon)^{1/2}/\sigma$ and varying fluid densities $\rho = 1.25{-}12.5\sigma^{-3}$. **Right:** Shear viscosity for fixed fluid density $\rho = 3.75\sigma^{-3}$ and varying friction coefficients $\gamma_{DPD} = 0.5 - 10.0(m\epsilon)^{1/2}/\sigma$.

of the global trend is correctly reproduced, as it was still reported in [78].
It can be shown [79, 80] that the friction coefficient is proportional to $\gamma_{DPD} \sim \omega_0 \sim 1/t_0$ with the collision frequency ω_0 and the collision time t_0. Thus the kinetic part of the shear viscosity is inversely proportional to the collision frequency with $\eta_K \sim 1/\omega_0$ whereas the dissipative part is proportional to $\eta_D \sim \omega_0$. For low friction coefficients, the kinetic contributions dominate the shear viscosity due to an uneffective collisional momentum tranfer. The situation is different for larger friction coefficients and fluid densities.
Both lead to increasing contributions of the dissipative term in Eqn. (3.20) due to larger collision frequencies. The collisions furthermore become more effective due to the presence of large fluid densities, which results in a dominating dissipative contribution of η_D in Eqn. (3.20).
Although Eqn. (3.20) and further sophisticated methods as the results of [78] have shown, do not produce a perfect agreement, the underlying physical interpretation of kinetic and dissipative contributions can be reproduced in agreement to the numerical results.
In Fig. 3.9 the results of a Periodic Poiseuille Flow method, reported in [77] are presented for varying force strengths and time steps. The method is easy to implement and extremely efficient. The shear stress of the periodic Poiseuille Flow is exerted by the particles themselves. The simulation box is divided into subdomains, where opposite directions of the external force are applied. Due to the stability argument, the velocity vanishes at the boundaries of the subdomains at $z = 0\sigma$ [50].
No drastic deviations on the flow profiles due to varying forces and timesteps can be ob-

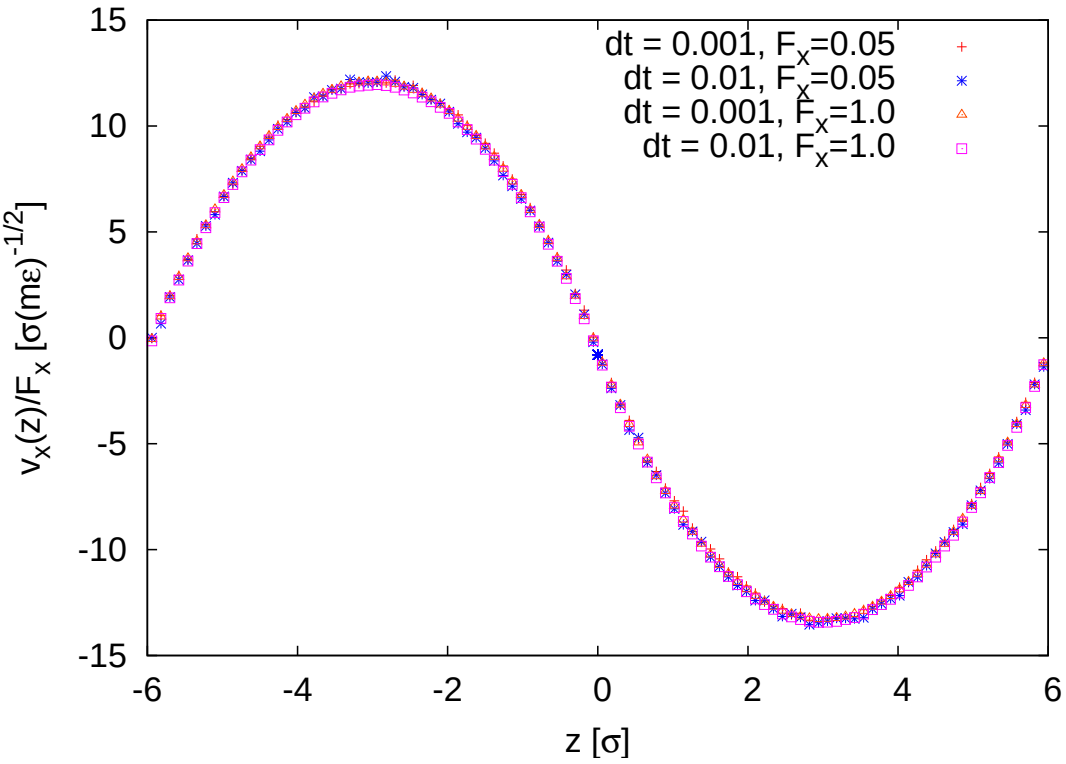

Figure 3.9: Flow profiles for periodic Poiseuille Flows [77] with a fluid density $\rho = 3.75\sigma$ and a friction coefficient $\gamma_{DPD} = 5.0(m\epsilon)^{1/2}/\sigma$.

served. Thus the shear viscosity can be considered as constant for moderate parameter sets in agreement to the right side of Fig. 3.7.

3.6 Calculation of the slip length and the hydrodynamic boundary positions

As it was mentioned in the introduction of this chapter, the flow behaviour is directly influenced by the slip length δ_B and the position of the hydrodynamic boundaries z_B. Calculating these parameters offers the possibility to directly compare the numerical results of the flow profile with analytic expressions.
It can be shown [81], that the slip length and the position of the hydrodynamic boundaries can be computed separately by a combination of the Plane Poiseuille and the Plane Couette Flow profile.
As Fig. 3.4 indicates, the width of the Couette flow C minus the distance between the walls L is given by

$$C - L = 2(\delta_B - \Delta), \tag{3.21}$$

with

$$\Delta = |z_0| - |z_B| \tag{3.22}$$

where $|z_0|$ denotes the position of the physical boundaries due to the finite range of the repulsive wall-fluid interactions.
The width of the parabolic flow profile P (*cf.* Eqn. (3.14)) yields

$$P = 2\sqrt{z_B^2 + 2\delta_B|z_B|} \tag{3.23}$$

which gives by comparison with Fig. 3.4

$$P^2 = 4z_B^2 + 8|z_B|\delta_B = (L - 2\Delta)^2 + 4(L - 2\Delta)\delta_B. \tag{3.24}$$

Calculating C^2 from Eqn. (3.21) and subtracting Eqn. (3.24) gives a final expression for the slip length δ_B

$$\delta_B^2 = \frac{C^2 - P^2}{4} \tag{3.25}$$

which can be easily evaluated by measuring the width of PCF and PPF profiles. In addition to Eqn. (3.25), the hydrodynamic boundary positions can be further calculated by Eqn. (3.21) and use of Eqn. (3.22) to

$$|z_B| = \frac{1}{2}(C - L) - \delta_B + |z_0|. \tag{3.26}$$

if the slip length is known.

3.7 Analytic theory for the boundary parameters

In this section an analytic expression for the calculation of the boundary parameters is presented. Within this approach, it is possible to tune the slip length systematically from full- to no-slip conditions. The detailed calculation can be found in the appendices A.1 and A.2. At this point, only the main results are presented.
Considering that the Stokes equation is still valid under the influence of the tunable-slip boundaries and under the condition that the fluid density is constant $\rho(z) = \rho_0$. Eqn. (3.13) then has to be extended by the average force exerted on the fluid particles in presence of the viscous layer (section 3.1) to

$$\eta_s \left(\frac{\partial^2 v_x(z)}{\partial z^2} \right) = \rho_0 \, \gamma_L \, \omega_L(z) \, v_x(z) - \rho_0 \, F_x^{ext} \tag{3.27}$$

with $< \vec{F}_i^R(t) >= 0$ and a reference wall velocity of $v_{x,wall} = 0$. For an effective description of slippage in terms of Eqn. (3.4), the total viscous force per area A

$$-\frac{< F_x >}{A} = \eta_s \left(\frac{\partial v_x^{(0)}(z)}{\partial z} \right)_{z=z_B} = \frac{\eta_s}{\delta_B} v_x^{(0)}(z_B) \tag{3.28}$$

exerted by the viscous layer has to be equal to the shear stress exerted on an unperturbed velocity profile $v_x^{(0)}(z)$ without tunable-slip boundary interactions. Explicit integration of Eqn. (3.28) yields

$$z_B = 0 \tag{3.29}$$

for the position of the hydrodynamic boundaries. This result is in agreement to the physical boundary positions if $z_0 = 0$ is assumed.
The slip length in general can be calculated by an evaluation of the flow velocity in terms of a Taylor-expansion. The following analytical equation for the slip length

$$\frac{\delta_B}{z_c} = \frac{1}{\alpha\ z_c \int_{z_0=0}^{z_c} \omega_L(z) dz} + \mathcal{O}(\alpha^0) \tag{3.30}$$

with

$$\alpha = \frac{\gamma_L\ \rho_0}{\eta_s} \tag{3.31}$$

can be derived. Furthermore for the special choice of a linear weighting function according to Eqn. (3.9), an approximate equation is given by

$$\frac{\delta_B}{z_c} = \frac{2}{\alpha {z_c}^2} - \frac{7}{15} - \frac{19\alpha z_c^2}{1800} + \mathcal{O}((\alpha z_c^2)^2). \tag{3.32}$$

In addition, it is also possible to solve for an exact equation

$$\frac{\delta_B}{z_c} = -1 + \frac{1}{(3\alpha z_c^2)^{1/3}} \frac{\Gamma\left(\frac{1}{3}\right)}{\Gamma\left(\frac{2}{3}\right)} \frac{I_{-2/3}\left(\frac{2\sqrt{\alpha} z_c}{3}\right)}{I_{2/3}\left(\frac{2\sqrt{\alpha} z_c}{3}\right)} \tag{3.33}$$

with the Gamma-function Γ and the second order Bessel functions I.
All expressions indicate, that the slip length is mainly influenced by the combined values of Eqn. (3.31) with the shear viscosity, the fluid density and the viscous friction coefficient. Thus the numerical results can be compared to the analytical expressions.

3.8 Numerical Results

3.8.1 Position of the hydrodynamic boundaries

The position of the hydrodynamic boundaries are derived by averaging the flow profiles of the Plane Poiseuille Flow for three external forces $F_x = 0.02, 0.035, 0.04\epsilon/\sigma$ and three wall velocity differencies $V_x = 1, 2, 3(m\epsilon)^{-1/2}$ for the Plane Couette Flow with varying viscous layer friction coefficients $\gamma_L = 0.1 - 1.0\sigma^{-1}(m\epsilon)^{1/2}$.
As it turned out, the friction coefficient γ_L does not perturb the position of the hydrodynamic boundaries for moderate values $\gamma_L < \gamma_{DPD}$. The left side of Fig. 3.10 presents the simulation results for a fixed fluid density $\rho = 3.75\sigma^{-3}$ with varying DPD friction coefficients γ_{DPD}. The coincidence of Eqn. (3.29) with $z_0 = 0\sigma$ is fulfilled for friction coefficients $\gamma_{DPD} > 3.0\sigma^{-1}(m\epsilon)^{1/2}$.

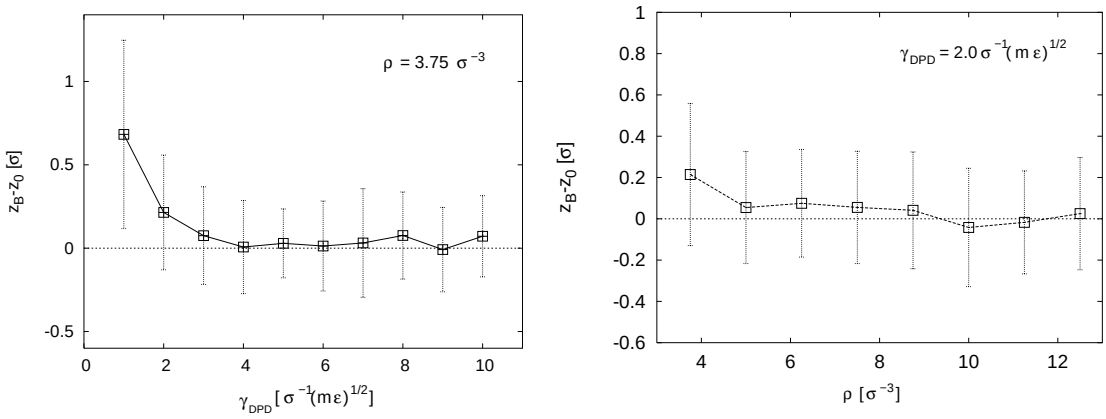

Figure 3.10: **Left:** Exemplary position of the hydrodynamic boundaries for a fixed fluid density $\rho = 3.75\sigma^{-3}$ and varying friction coefficients γ_{DPD}. The hydrodynamic boundary positions are calculated in distances to the physical positions of the walls z_0. **Right:** Exemplary position of the hydrodynamic boundaries for a fixed friction coefficient $\gamma_{DPD} = 2.0\sigma^{-1}(m\epsilon)^{1/2}$ and varying fluid densities ρ. The hydrodynamic boundary positions are calculated in distances to the physical positions of the walls z_0.

The right side of Fig. 3.10 presents identical results for a fixed friction coefficient $\gamma_{DPD} = 2.0\sigma^{-1}(m\epsilon)^{1/2}$ with varying fluid densities.
The results of Fig. 3.10 are in agreement with Eqn. (3.29) for moderate, not too small parameter values. The deviations can be explained by kinetic considerations.
For larger densities the behaviour of the particles become more fluid-like due to a diminished mean free path [53]. Thus molecular motion is replaced by collective motion for higher densities and the transport of momentum is dominated by diffusive transport. The Stokes equation (Eqn. (3.13)) is therefore valid. On the other hand, as it was mentioned in section 3.5, large friction coefficients in combination with increasing densities allow an effective collisional momentum transfer such as in real fluids. Again the Stokes equation can be used to correctly describe this regime and the validity of the approach presented in section 3.7 is guaranteed.

3.8.2 Slip length

Fig. 3.11 presents the values of the slip length with nearly all data points in good agreement to the analytic expression of Eqn. (3.32) except those whose hydrodynamic boundary positions differ to Eqn. (3.29) with $z_0 = 0$ (violet triangles in coincidence with Fig. 3.10). Thus the validity of Eqn. (3.29) gives a rough estimate if the numerical results of the slip length are in agreement to the theory.
As the inset of Fig. 3.11 further shows, no-slip boundary conditions can be obtained for certain parameter sets. It is obvious that the slip length can become zero (corresponding

to no-slip) or even negative (inset of Fig. (3.11)). It is shown in the appendix A.2 that a no-slip boundary condition is obtained at $\alpha = 3.973$ for the linear weight function of Eqn. (3.9). Negative slip lengths are encountered at even larger α. In this case, the hypothetical velocity flow profile changes sign close to the boundary. Indeed the true velocity profile never changes sign, hence the negative slip lengths do not correspond to unphysical situations.
It is obvious, that the proposed method can be applied over a wide range of parameter sets from full-slip with $\gamma_L = 0\sigma{-}1(m\epsilon)^{1/2}$ to no-slip. Therefore several boundary conditions can be investigated by an easy change of parameter sets. Thus, the efficient modelling of several surface characteristics is possible. Another advantage is the easy implementation and the applicability for curved geometries which has been published in [70]. Furthermore as the results of the next chapter will show, the applicability of the tunable-slip boundaries is even possible for the simulation of electrokinetic transport phenomena in confined geometries.

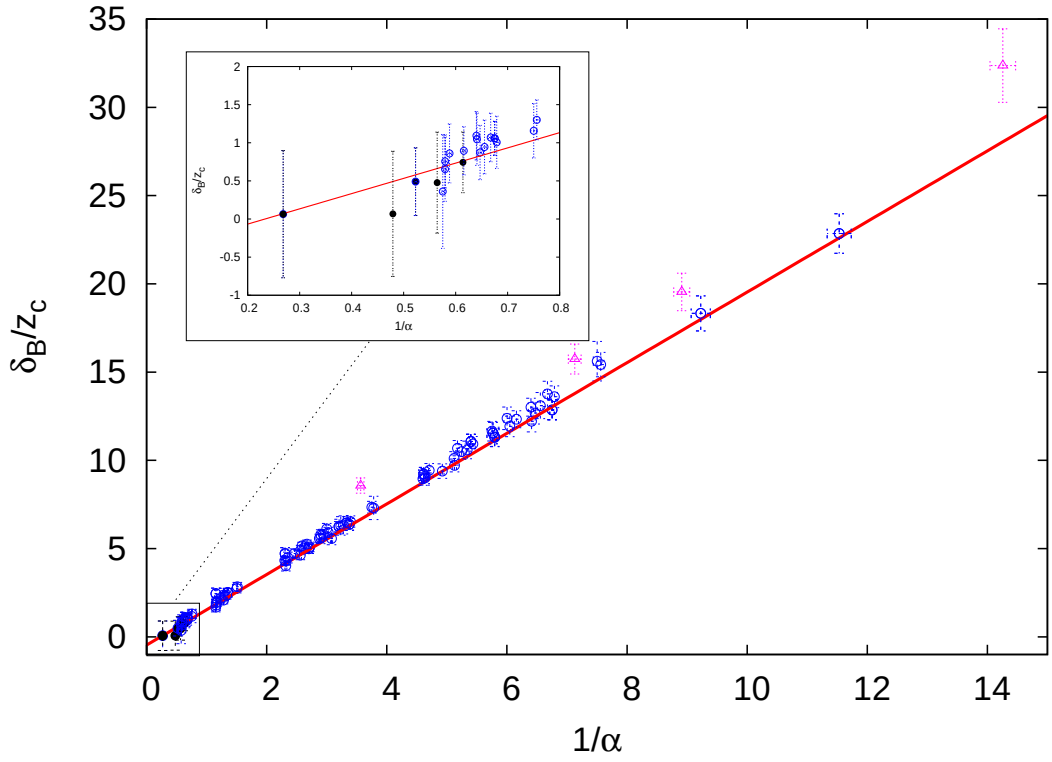

Figure 3.11: Slip length δ_B in units of z_c vs. α for varying values of the parameter triplet $(\rho, \gamma_{DPD}, \gamma_L)$ (in units of σ^{-3} or $\sqrt{m\epsilon}/\sigma$, respectively). Blue: series with ρ (3.75, 2-10, 0.1-1) and with γ_{DPD} fixed: (3.75-12.5, 2, 0.1-1). Black: selected triplet values: (6.35,5,1),(5,5,1), (11.25,2,1.1), (11.25,2,1.2), (3.75,10,2.5). Violet triangles: series corresponding to the point in Fig. 3.10, where the position of the hydrodynamic boundary deviates from theoretical expectation: (3.75,1,0.1-1). Red line: Theoretical prediction of Eqn. (3.32). The inset shows a blowup of the same data.

4 Modelling electrokinetic phenomena: The electroosmotic flow

Denkt an die Elektrolyte!
- Sven Regener (2001)

As it was mentioned in chapter 3, microgeometries are dominated by a large surface-to-volume ratio where surface friction effects play a crucial role in the characteristics of flow phenomena. In addition to hydrodynamic boundary effects, electrostatic interactions of the ions in the solution cause several phenomena which have been neglected in the last chapter. The present chapter takes these effects into consideration.
If a surface comes into contact with a solvent, most materials get charged due to the association or dissociation of ions [82]. This phenomenon is caused by the finite solubility of materials in liquids. The strength of the dissociation is determined by the dissociation constant K_D.
The following example reaction of carboxylide surface groups $R-COOH$ with water in chemical equilibrium shows

$$R-COOH+H_2O \rightleftharpoons R-COO^- + H_3O^+ \tag{4.1}$$

that a finite concentration of hydrogen ions is released into the solution. The concentration of the products is steered by K_D

$$K_D = \frac{c[H_3O^+]\cdot c[R-COO^-]}{c[R-COOH]\cdot c[H_2O]} \tag{4.2}$$

with constant concentrations c [83].
In addition to the dissociation of surface groups, the association of ions from the solution is also possible as well. The final result is a net rest charge at the surface which is balanced by an oppositely charged amount of counterions in the solution in front of the surface. The structure of the ion distribution is schematically shown in Fig. 4.1.
Introducing some definitions, all ions which are electrostatically bound to the surface are within the electric double layer [1]. The bare effective potential of the surface is diminshed due to the presence of the electric double layer and vanishes in the bulk region. The electric double layer can be divided into the Stern layer and the outer Helmholtz plane. In the outer Helmholtz plane, the ions are in rapid thermal motion in contrast to the Stern layer, where the ions stick to the surface. Thus, the ions of the Stern layer cannot be removed by pure thermal motion.
For an applied external force or pressure gradient, the bound ions of the Stern layer

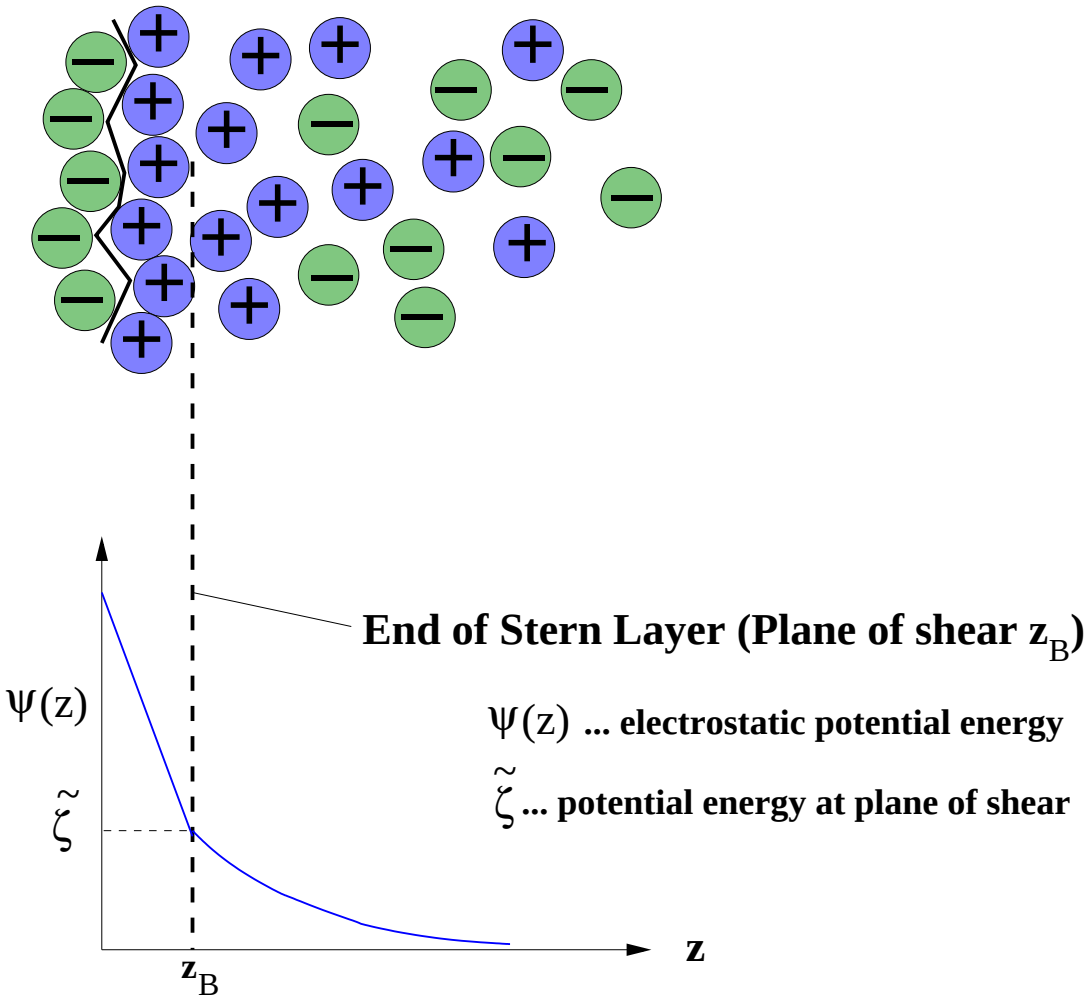

Figure 4.1: **Top:** Illustration of an electric double layer in front of a charged surface. **Bottom:** Distribution of the electrostatic potential $\psi(z)$ at different distances z with zeta potential $\tilde{\zeta}$ at the plane of shear z_B.

act as a plane of shear for the fluid flow. The potential which can be measured at this point is the zeta potential $\tilde{\zeta}$. The magnitudes of several electrokinetic flow profiles are influenced by this observable [84, 85]. Measuring the zeta potential is a delicate task for an experimentalist due to wetting properties or chemical patterning of the surface. These characteristics influence the results of electric conduction measurements which are needed for a determination of this potential [86].
In this chapter, simulations of the counterion-induced electroosmotic flow are presented. Analytical solutions in the electrostatic weak-coupling regime for the flow profiles, in the presence of partial-slip as well as no-slip boundary conditions are derived which are in good agreement with the numerical results. Additionally, a general scheme to

match mesoscopic simulation methods by comparing the results of Dissipative Particle Dynamics-simulation to coupled Langevin Dynamics / Lattice-Boltzmann simulations is presented. The results of the Lattice-Boltzmann simulation have been derived by Dr. Marcello Sega at the Frankfurt Institute of Advanced Studies (FIAS).

4.1 Theory of electrostatic effects in ionic solution

4.1.1 The Poisson-Boltzmann equation

A mathematical description of the electric double layer for moderate surface charge densities and moderate temperatures is possible in terms of a mean-field approach.
The Poisson-Boltzmann theory describes the distribution of counterions and the corresponding potential in front of charged objects by a combination of assumptions related to statistical mechanics and electrostatics. The theory neglects the excluded-volume effects of the counterions and regards them as pure point-like particles which are not correlated with each other. The derivation of the basic equation is motivated by the characteristics of the chemical equilibrium. The density of ionic species ρ_i is determined by the chemical potential μ_i

$$\mu_i(\vec{r}) = Z_i e\psi(\vec{r}) + k_B T \log \rho_i(\vec{r}) \tag{4.3}$$

with charge $Z_i e$, Boltzmann constant k_B, temperature T and electrostatic potential $\psi(\vec{r})$. [82, 83, 87]. Solving for $\rho_i(\vec{r})$ with constant chemical potential $\delta\mu_i(\vec{r}) = 0$, as required in chemical equilibrium yields

$$\rho_i(\vec{r}) = \rho_{0,i} e^{-Z_i e\psi(\vec{r})/k_B T} \tag{4.4}$$

with constant ion density $\rho_{0,i}$ for each species at $\psi(\vec{r}) = 0$. The distribution of ions is therefore given by a Boltzmann distribution at each point determined by the electrostatic potential $\psi(\vec{r})$.
The Poisson-Boltzmann equation

$$\Delta\psi(\vec{r}) = -\sum_i \frac{Z_i e}{\epsilon_r}\rho_i(\vec{r}) = -\sum_i \frac{Z_i e}{\epsilon_r}\rho_{0,i} e^{-\frac{Z_i e\psi(\vec{r})}{k_B T}} \tag{4.5}$$

can finally be derived by a combination of the Poisson equation

$$\Delta\psi(\vec{r}) = -\sum_i \frac{Z_i e}{\epsilon_r}\rho_i(\vec{r}) \tag{4.6}$$

with the dielectric constant ϵ_r summed over all ionic species [88] and Eqn. (4.4). Solving this equation is in many cases very complicated due to its second order inhomogeneous character. Nevertheless this equation plays a central role in theories for many biological processes, like molecular recognition and steering of cell processes [89].

4.1.2 Poisson-Boltzmann theory for microchannels

In the case of planar microchannels filled with liquid solution, the problem can be reduced to the solution of the Poisson-Boltzmann equation between two similarily and homogeneously charged surfaces. If additional salt ions are present, the solution of Eqn. (4.5) can solely be numerically derived if not drastic simplifications have to be taken into consideration.
For the case of pure counterions without additional salt ions, an analytical solution is given [82, 90] by assuming two planar homogeneously charged surfaces at $z = \pm a$. Due to the neglect of additional ionic species, the charge will be denoted by Ze for simplicity. The boundary conditions are given by symmetry in the middle of the channel to

$$\frac{\partial}{\partial z}\psi(z)|_{z=0} = 0 \tag{4.7}$$

and through electroneutrality at the surface plates

$$\frac{\partial}{\partial z}\psi(z)|_{z=a} = \frac{\partial}{\partial z}\psi(z)|_{z=-a} = \frac{\sigma_A}{\epsilon_r} \tag{4.8}$$

with the surface charge density σ_A.
The Poisson Boltzmann equation (Eqn. (4.5)) can be solved in a standard way [84] by the following identity

$$2\frac{\partial^2\psi(z)}{\partial z^2}\frac{\partial\psi(z)}{\partial z} = \frac{\partial}{\partial z}\left(\frac{\partial\psi(z)}{\partial z}\right)^2 \tag{4.9}$$

to

$$\psi(z) = -\frac{k_BT}{Ze}\log(\tan^2(\kappa z) + 1) = \frac{k_BT}{Ze}\log(\cos^2(\kappa z)) \tag{4.10}$$

for the potential distribution in a channel with the screening constant

$$\kappa^2 = \frac{(Ze)^2\rho_0}{2\epsilon_r k_BT} \tag{4.11}$$

where ρ_0 denotes the counterion density in the middle of the channel. Differentiation according to Eqn. (4.5) yields for the counterion distribution

$$\rho(z) = \frac{\rho_0}{\cos^2(\kappa z)} \tag{4.12}$$

and for the electric field

$$E(z) = -\frac{\partial}{\partial z}\psi(z) = -\frac{2\kappa k_BT}{Ze}\tan(\kappa z) \tag{4.13}$$

as the first derivative of Eqn. (4.10).
In addition to electrostatic attractions, it can be shown for the case of homogeneously charged walls that the counterion distribution follows entropic origins [82]. The electrostatic attraction of the surface drives the dissociated ions back instead of releasing them

into the solution. This is due to the fact that a net coulombic force for a electroneutral system always favour the association of counterions. Regarding the configurational entropy of the system, this quantity can solely be increased as demanded [22] by a repulsive osmotic pressure which forces the ions away from the surface. The osmotic pressure finally dominates the system and the counterions are repelled into the solution leading to the distribution of Eqn. (4.12).
As it was mentioned in the introduction of this subsection, the solution of Eqn. (4.5) in the presence of salt ions is obtained by simplifications. Neglecting the counterions and taking only the ions of a $(1:1)$ salt with valency $(-Z_1 = Z_2 = Z)$ in front of only one planar surface into consideration, the following identity [91]

$$\sinh p = \frac{e^{p} - e^{-p}}{2}, \tag{4.14}$$

can be applied and the following equation, instead of Eqn. (4.5)

$$\frac{\partial^2}{\partial z^2}\psi(z) = \frac{2Ze\rho_0}{\epsilon_r}\sinh\left(\frac{Ze\psi(z)}{k_BT}\right) \tag{4.15}$$

where $\rho_0 = \rho_{0,1} = \rho_{0,2}$ is the density of each species, can be derived. Integration between z and $z = 0$ and the use of Eqn. (4.9) yields

$$\left(\frac{\partial\psi(z)}{\partial z}\right)^2 = \frac{4\rho_0 k_BT}{\epsilon_r}\left[\cosh\left(\frac{Ze\psi(z)}{k_BT}\right) - 1\right] \tag{4.16}$$

which can be simplified by [91]

$$\sinh\left(\frac{p}{2}\right) = \pm\sqrt{\frac{1}{2}(\cosh(p) - 1)} \tag{4.17}$$

to

$$\frac{\partial}{\partial z}\psi(z) = -\sqrt{\frac{8\rho_0 k_BT}{\epsilon_r}}\sinh\left(\frac{Ze\psi(z)}{2k_BT}\right). \tag{4.18}$$

For low potential energies $|Ze\psi| \ll k_BT$, the substitution

$$\sinh\left(\frac{Ze\psi(z)}{2k_BT}\right) \approx \frac{Ze\psi(z)}{2k_BT} \tag{4.19}$$

is valid and Eqn. (4.18) is then simplified to

$$\frac{\partial}{\partial z}\psi(z) = -\sqrt{\frac{2(Ze)^2\rho_0}{\epsilon_r k_BT}}\psi(z) \tag{4.20}$$

which can be integrated between z and a to give

$$\psi(z) = \psi_a e^{-k_D(z-a)} \tag{4.21}$$

with

$$k_D^{-1} = \sqrt{\frac{\epsilon_r k_B T}{2(Ze)^2 \rho_0}}. \tag{4.22}$$

Eqn. (4.21) can also be derived by a strict Taylor expansion (linearisation) of Eqn. (4.5) with the assumption that the electric energy is small compared to the thermal energy $|Z_i e\psi| \leq k_B T$. Applying this expansion for a general salt solution with N ionic species yields

$$\frac{\partial^2}{\partial z^2}\psi(z) = -\frac{1}{\epsilon_r}\sum_i^N \left(Z_i e \rho_{i,0} - \frac{(Z_i e)^2 \rho_{i,0}\psi(z)}{k_B T} \right) \tag{4.23}$$

which by the condition of electroneutrality

$$\sum_i^N Z_i e \rho_{i,0} = 0 \tag{4.24}$$

reads

$$\frac{\partial^2}{\partial z^2}\psi(z) = \kappa_D^2 \psi(z). \tag{4.25}$$

with the definition of the Debye-Hückel length

$$\kappa_D^{-1} = \sqrt{\frac{\epsilon_r k_B T}{\sum_i^N (Z_i e)^2 \rho_{i,0}}}. \tag{4.26}$$

which is the general form of Eqn. (4.22). Solving for the potential, in agreement to Eqn. (4.21) yields

$$\psi(z) = \psi_a e^{-\kappa_D (z-a)} \tag{4.27}$$

where the effective screening of the electrostatic interactions is obvious.

4.2 Theory of the electroosmotic flow (EOF)

The presence of ions in the solution can be used to enhance electrostatically driven fluid flows which are on the micrometer scale experimentally easier to derive than pressure- or shear driven flows [47].
If an external electric field acts on the solution, the ions move in the direction of the electric field corresponding to their charge. By dragging the solvent particles along, a net fluid flow as a collective phenomenon forms, which is called the electroosmotic flow (EOF).

4.2.1 Electroosmotic flow with salt ions

Detailed analytical solutions for the flow profiles in the presence of salt can only be derived in terms of the zeta potential and the Debye-Hückel theory [84] according to

section 4.1.2. Combining the Stokes equation (Eqn. (3.13)) with the Poisson equation (Eqn. (4.6)) gives

$$\frac{\partial^2}{\partial z^2} v_x(z) = -\frac{\epsilon_r E_x}{\eta_s} \frac{\partial^2}{\partial z^2} \psi(z) \tag{4.28}$$

which can be solved for the velocity $v_x(z)$ by inserting Eqn. (4.27). Integration with respect to z and using the no-slip boundary condition (*cf.* chapter 3) at z_B together with the corresponding zeta potential $\tilde{\zeta}$ and the boundary condition $\partial_z v_x(0) = 0$ (Eqn. (4.7)) yields

$$v_x(z) = -\frac{\epsilon_r \tilde{\zeta}}{\eta_s} E_x (e^{-\kappa_D (z+z_B)} + e^{-\kappa_D (z_B - z)} - 1 - e^{-2\kappa_D z_B}) \tag{4.29}$$

where the electroosmotic mobility with $v_x = \mu_{EOF} E_x$ for no-slip boundary conditions (Eqn. (3.1)) in the middle of the channel is given by

$$\mu_{EOF} = -\frac{\epsilon_r \tilde{\zeta}}{\eta_s} (2e^{-\kappa_D z_B} - e^{-2\kappa_D z_B} - 1) \tag{4.30}$$

where $\tilde{\zeta}$ is defined at the hydrodynamic boundary positions z_B, which act as the plane of shear (*cf.* chapter 3) for the flow profile.
By applying partial-slip boundary conditions (*cf.* Eqn. (3.4)), it is also possible to derive an expression for $v_x(z_B)$ by differentiation of Eqn. (4.29) to

$$v_x(z_B) = \frac{\epsilon_r \tilde{\zeta} \delta_B \kappa_D}{\eta_s} E_x (e^{-2\kappa_D z_B} - 1) \tag{4.31}$$

which is added to Eqn. (4.29) and enhances the flow profile due to slippage effects. The normalised electroosmotic flow profile as derived by DPD simulations is shown in Fig. 4.2 where it is obvious that the corresponding plug-like flow profile as predicted by Eqn. (4.29) can be reproduced.

4.2.2 Counterion-induced electroosmotic flow

In contrast to the salt case, detailed analytic expressions in a slit channel for the counterion-induced electroosmotic flow where salt ions are neglected, can explicitly be derived. In agreement to the former case, a combination of the Stokes equation (Eqn. 4.28) and the Poisson equation (Eqn. 4.6) with $Z_i = Z$ per definition, can be used for a straightforward integration between z and $z_0 = 0$ by use of the symmetry condition (Eqn. 4.7) with $\partial_z v_x(0) = 0$. Second integration between z and the hydrodynamic boundary positions z_B with the partial-slip boundary condition (Eqn. (3.4)) finally yields

$$\begin{aligned} v_x(z) &= \frac{\epsilon_r k_B T}{Ze\eta_s} E_x \left(\log(\cos^2(\kappa z_B)) - \log(\cos^2(\kappa z)) \right) \\ &\quad + \delta_B \partial_z v_x(z)|_{z=z_B} \end{aligned} \tag{4.32}$$

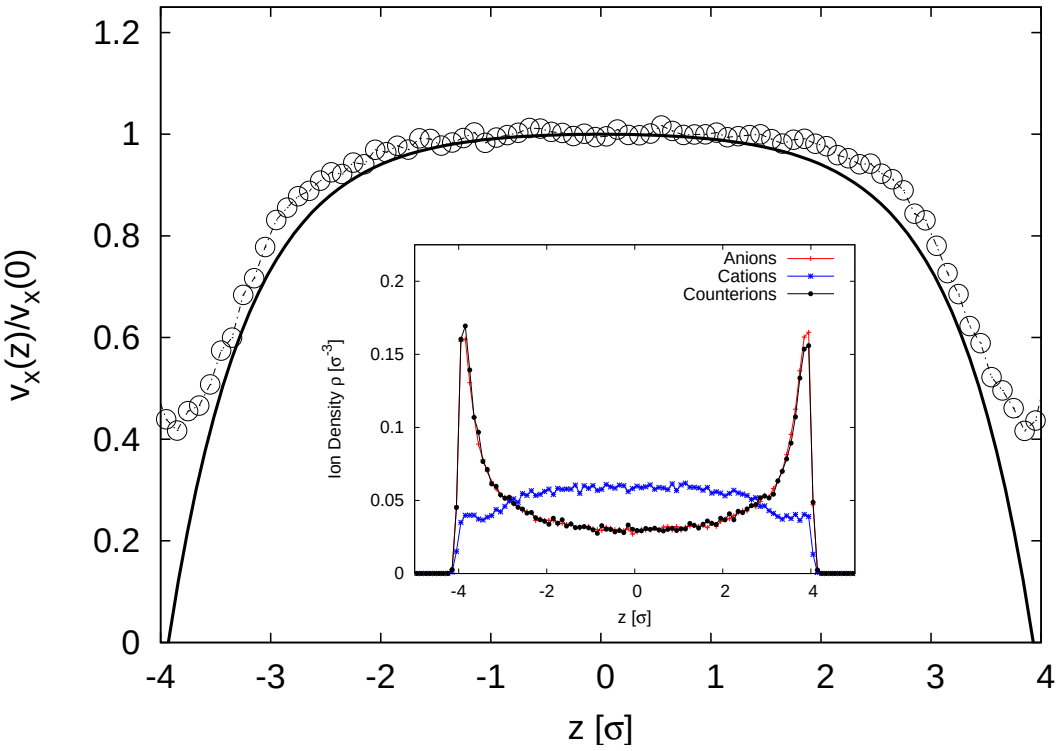

Figure 4.2: Normalised electroosmotic flow profile for a salt concentration $\rho_s = 0.053\sigma^{-3}$ with counterion density $\rho_c = 0.0525\sigma^{-3}$, surface charge density $\sigma_A = 0.208e/\sigma^2$ and external electric field $E_x = 1\epsilon/e\sigma$ ($\kappa_D^{-1} = 0.71\sigma$). The solvent density is $\rho = 3.75\sigma^{-3}$ with friction coefficient $\gamma_{DPD} = 5.0\sigma^{-1}(m\epsilon)^{1/2}$. The black line shows the theoretical prediction of Eqn. (4.29) divided by $v_x(0)$. The hydrodynamic boundaries are at $|z_B| = 3.866$ in agreement to section 4.5.2. **Inset:** Corresponding local salt and counterion density between two similar inhomogeneously charged surfaces with surface charge density $\sigma_A = 0.208e\sigma^{-2}$ for monovalent charges.

with the flow magnitude depending on the slip length δ_B. Explicit calculation gives

$$v_x(z) = \frac{\epsilon_r k_B T}{Ze\eta_s} E_x(\log(\cos^2(\kappa z_B)) - \log(\cos^2(\kappa z)) + 2\kappa\delta_B \tan(\kappa z_B)). \tag{4.33}$$

as the final expression for the flow profile in an electrostatic weak-coupling expression evaluated by the Poisson-Boltzmann theory, where ϵ_r can also be expressed in terms of the Bjerrum length

$$\lambda_B = \frac{e^2}{4\pi\epsilon_r k_B T}. \tag{4.34}$$

and the definition of κ is given in Eqn. (4.11).

4.3 Electrostatic coupling regimes

Electrostatic interactions between charged objects can be divided due to their strength into several regimes. In agreement to the simulation results of the counterion induced electroosmotic flow presented later in this chapter, additional salt charges will be neglected. Thus for reasons of simplicity, the charge will be denoted by Ze.
Different electrostatic coupling regimes can be realised by changing the surface charge density, multivalent counterions or varying temperatures. A parameter to distinguish between these limits is the electrostatic coupling constant

$$\Xi = 2\pi Z^3 \lambda_B^2 \sigma_A, \tag{4.35}$$

which determines the strength of the electrostatic interactions between the ions and the surface with the surface charge density σ_A [92, 93, 94]. Low values of Ξ correspond to a diffusive counterion layer while large values correspond to a nearly flat, highly adsorbed and massively correlated counterion layer where the lateral distance a' between the counterions is large.
The weak coupling limit with Ξ_{WC} is given for moderate surface charge densities and monovalent ions whereas the strong coupling limit with Ξ_{SC} is realised for high surface charge densities, lower temperatures or multivalent charges. The counterion distribution in both regimes can be calculated analytically, whereas in the intermediate regime with Ξ_{IC} for low surface charge densities and multivalent ions, a full analytical derivation is complicated and still missing [95]. The distinction of the regimes by concrete values of Ξ is possible in the case of only one single charged plate, where it has been shown that the strong-coupling theory is valid for $\Xi > 1$ [95].
In contrast to that, a separation by values of Ξ in very narrow nanochannels does not make sense due to the rivaling plate distance d and the lateral distance a' between the ions. Although the ions are highly correlated and adsorbed, the perturbations of the close opposite layer are drastic due to overlapping effects. Thus a rough estimate of the strong coupling regime in nanochannels is then only valid for the ratio $d/a' < 1$ [93]. This ratio indicates highly correlated ions whose repulsion dominates the ordering of the layer, as it is required by the strong coupling theory. A flat layer is then given for $\Xi \sim (a'/\mu)^2 \gg 1$ with the Gouy-Chapman length

$$\mu = \frac{1}{2\pi Z \lambda_B \sigma_A} \tag{4.36}$$

which gives an estimate of the width of the counterion layer [95]. Thus, both conditions have to be fulfilled to satisfy the description in terms of the strong coupling theory [93]. The standard Poisson-Boltzmann theory fails in the case of high surface charge densities, larger Bjerrum lengths due to multivalent charges or lower temperatures. The ions are highly correlated and mean-field approaches, like the Poisson-Boltzmann theory have to be replaced by field-theoretic methods. It has been shown, that these methods are asymptotically correct in the strong coupling regime [92, 93, 94] and produce reasonable results.

Special attention has been spent on completely decoupled counterion layers which are given if the plate distance d is much larger than the Gouy-Chapman with $d \gg \mu$ [93]. The counterion density distribution between two planar highly charged surfaces then reads [93]

$$\rho(z) = \frac{2\pi\lambda_B\sigma_A^2}{(1-e^{-d/\mu})}\left(e^{-(z+d/2)/\mu} + e^{-(d/2-z)/\mu}\right) \tag{4.37}$$

corresponding to two independent counterion layers with an exponential decay.

4.4 Comparison between Lattice-Boltzmann and DPD simulations.

As it was mentioned in Chapter 2, detailed comparative studies between the results of different mesoscopic simulation methods are scarce. The problem is related to different interpretations of the input and output parameters. Therefore the choice of a simulation method for a specific system is often a choice of personal preferences. Nevertheless, producing comparable results between different simulation methods is in general desirable. As it was mentioned in the introduction of this chapter, a general mapping scheme between Lattice-Boltzmann (LB) and DPD methods is presented to bridge this gap. The technique of the LB method was briefly introduced in Chapter 2. All LB simulation results have been derived by Dr. Marcello Sega. In the following, the principles of this parameter mapping scheme will be presented.

4.4.1 Parameter mapping

The fundamental relation in microchannel hydrodynamics is the Stokes equation (3.13). The parameters of this equation have necessarily to agree for a comparison of hydrodynamic simulation methods and the corresponding results.
As a fundamental parameter, the solvent density ρ is easy to match in DPD- and LB-simulations because it is a free-to-choose input parameter. The difficulty lies in the tuning of the shear viscosity η_s. In contrast to DPD, this parameter is an input parameter in the LB method.
As Eqn. (3.20) and Fig. 3.7 in the DPD method have indicated, the shear viscosity is mainly influenced by the friction coefficient γ_{DPD}, the solvent density ρ, the temperature T and the cut-off range of the DPD-interactions r_c. Therefore it is efficient to measure the shear viscosity in DPD-simulations for a well-chosen parameter set and match it in the LB method afterwards. The shear viscosity can be determined by the methods proposed in chapter 3.
Fixing all necessary parameters for the Stokes equation, a specific parameter of a coupled Langevin/LB-method has to be tuned additionally. The delicate coupling of the discrete particles on the solvent nodes has to be fulfilled *via* a modified Langevin equation as it was shown in Eqn. (2.22). Therefore the intrinsic effective diffusion coefficient D of each particle has to be tuned by varying the coupling constant ζ_{LB} until it is in agreement to the effective diffusion coefficient of a particle in the DPD simulations.

Regime	Ξ	$\mu[\sigma]$	$\sigma_A[e\sigma^2]$	Ze
Poisson-Boltzmann	1.307	0.764	0.208	1
Intermediate	4.189	0.955	0.088	2

Table 4.1: Coupling constant Ξ, Gouy-Chapman length μ, surface charge density σ_A and charge Ze for the different simulation setups.

The coincidence can be checked by comparing the velocity autocorrelation function of a particle in both methods which is connected to the diffusion coefficient D by a Green-Kubo expression [30].

4.4.2 Simulation details

Simulations have been performed for the weak-coupling (Poisson-Boltzmann regime) as well as for the intermediate coupling regime. The cubic simulation box ($12\sigma \times 12\sigma \times 12\sigma$) is periodic in x- and y-direction and confined by impermeable walls in z-direction. The positions of the walls are at $z_{wall} = 0\sigma$ and $z_{wall} = 10\sigma$. Electrostatics are calculated by P3M [33] and the ELC-algorithm [39] for $2D + h$ slabwise geometries.
The remaining difference of 2σ in z-direction is due to the electrostatic gap size of the ELC-algorithm. The walls act on the fluid particles respectively the ions *via* a WCA-potential [73]

$$U_{WCA} = 4\epsilon \left[\left(\frac{\sigma}{r}\right)^{12} - \left(\frac{\sigma}{r}\right)^{6} \right] + \epsilon \tag{4.38}$$

with the energy parameter ϵ and the cut-off distance $r_{WCA} = 2^{1/6}\sigma$. The Coulomb potential is expressed in terms of the Bjerrum length with $\lambda_B = 1.0\sigma$.
The effective density of the solvent particles is given by $\rho = 3.75\sigma^{-3}$ with a friction coefficient $\gamma_{DPD} = 5.0\sigma^{-1}(\sigma\epsilon)^{1/2}$, a cutoff radius of the DPD interactions $r_c = 1.0\sigma$ and a mass m set to unity. The temperature is $T = 1.0\epsilon/k_B$ and the DPD timestep is $\delta t = 0.01\sigma(m/\epsilon)^{1/2}$.
Tunable-slip boundary conditions are in use with friction coefficients $\gamma_L = 0.96$, 1.4049, 3.1 and 6.1 $\sigma^{-1}(m\epsilon)^{1/2}$ for no-slip and partial-slip boundary conditions. The range of the viscous interactions is $z_c = 2.0\sigma$.
Conservative interparticle interactions for the ions are given by the above mentioned WCA-potential with identical parameters. For the counterion-induced electroosmotic flow in the Poisson-Boltzmann limit, the counterion density is $\rho_c = 0.0525\sigma^{-3}$ with a unit charge $Ze = -1$. The resulting coupling constant $\Xi = 1.307$ is moderate for the weak coupling regime.
The intermediate coupling regime is given by the counterion density $\rho_c = 0.0104\sigma^{-3}$ with charge $Ze = -2$ which corresponds to a coupling constant of $\Xi_{IC} = 4.189$. The corresponding parameters are presented in Table 4.1.
Simulations are further performed for inhomogeneously and homogeneously charged walls. Inhomogeneously charged walls are given by placing discrete and fixed charges

randomly all over the walls whereas homogeneously charged walls are given for uncharged walls. This becomes obvious by calculating the electric potential in the channel, which is constant in the case of two planar homogeneously and similarly charged walls. All simulations with homogeneously charged walls have been performed by the MMM2D-method [37] which relies on the MMM-Family of electrostatic interaction solvers [34, 35, 36]. Fig. 4.3 presents a schematic illustration of the simulation box.

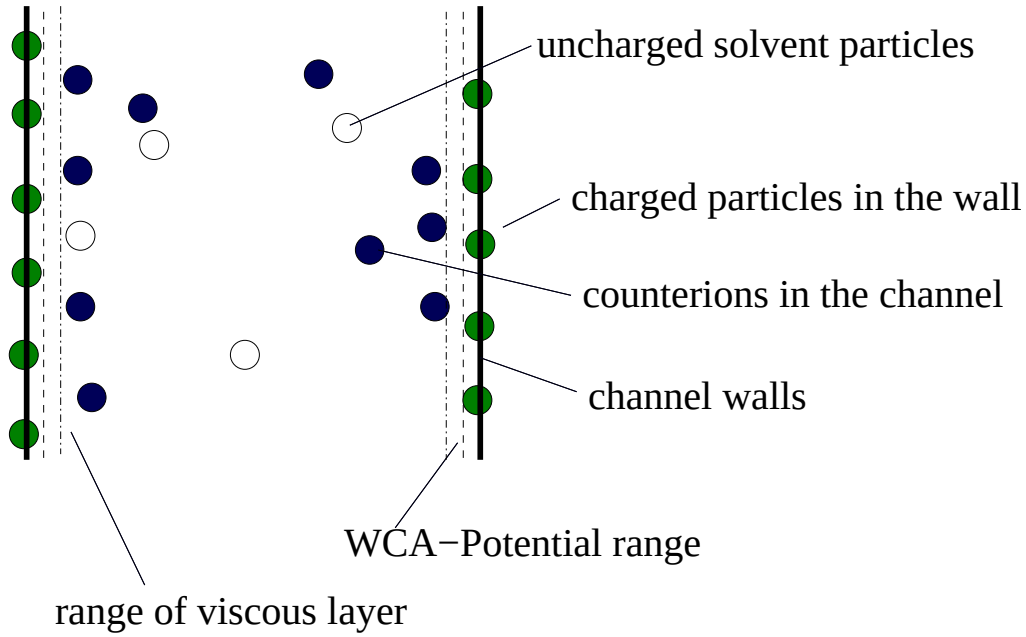

Figure 4.3: Schematic illustration of the simulation box. Discrete charges are placed randomly all over the wall for inhomogeneously charged walls. The same number of charges is placed in the bulk due to electroneutrality. Uncharged particles interact only by DPD interactions with the charged particles. Tunable-slip boundaries are applied.

The LB simulations were carried out using the lattice $D3Q19$. The walls for the ions are placed as in the DPD simulations at $z_{wall} = 0$ and 10σ. The solvent does not interact with the walls due to the discrete positions of the 24^3 solvent nodes. The grid spacing of the LB fluid is $a = 0.5\sigma$. The coupling constant of the fluid with the ions is $\zeta_{LB} = 1.98\sigma^{-1}(m\epsilon)^{1/2}$, which was derived by the proposed mapping scheme (see section 4.5.2).
The timestep for the motion of the ions is $\delta t = 0.01\sigma(m/\epsilon)^{1/2}$ as well as for the fluid $\tau = 0.01\sigma(m/\epsilon)^{1/2}$. Bounce-back boundary conditions are applied on the fluid at the wall positions to create no-slip boundary conditions.

Methods	DPD+TSC	LB+BBC	DPD+TSC+CS	LB+BBC+CS
Time/step [s]	0.09	0.01	0.22	0.14

Table 4.2: Time needed for computing a single integration step in the DPD method with tunable-slip boundary conditions (DPD+TSC) and electrostatics (DPD+TSC+CS) in comparison to the LB method with bounce-back boundary conditions (LB+BBC) and electrostatics (LB+BBC+CS).

4.5 Numerical Results

4.5.1 Computational cost

An important criterion for choosing a method is its computational cost and efficiency. The time was measured to calculate a single time step in both methods on an Athlon© MP2200+ CPU. The first two columns of Table 4.2 present the time needed for the calculation of a single time step of an uncharged system with 4320 solvent particles (DPD), respectively 1728 solvent nodes (LB) in the above mentioned microgeometry with hydrodynamic boundary conditions.
The LB method is nine times faster than the DPD-method but these values are strongly dependend on the number of chosen solvent particles, respectively chosen solvent nodes. The last two colums present the values for a charged system in the Poisson-Boltzmann limit. It is evident that an important amount of time is spent on the calculation of the electrostatic interactions for 60 ions and 60 counterions (surface ion density $\sigma_s = 0.208\sigma^{-2}$) even for optimal parameter values (Ewald parameter $\alpha = 2.1875$ (Eqn. (2.25)), accuracy 10^{-4}, mesh size 32^3). This indicates, that if electrostatic interactions are considered, both methods are nearly comparable in their computational cost and efficiency although it has to be noticed that the efficiency of P3M strongly depends on the chosen parameter values.

4.5.2 Fluid Properties

Shear viscosity

Calculating the shear viscosity by fitting a Plane Poiseuille Flow (Eqn. (3.19)) with present counterions of density $\rho_c = 0.0525\sigma^{-3}$, which is shown in Fig. 4.4, yields a value of $\eta_s = (1.334 \pm 0.003)\sigma^{-2}(m\epsilon)^{1/2}$.
The electrostatic interactions do not alter the shear viscosity significantly due to nearly identical flow profiles. Therefore the results of the charged system are in good agreement to the results derived in chapter 3.
The influence of counterions and electrostatic interactions on the shear viscosity plays no important role for such low counterion densities. Thus the same shear viscosity as in the uncharged case can be assumed. The values for the slip length as measured by a combination of the Plane Poiseuille and the Plane Couette Flow (chapter 3) are presented in Table 4.3 and compared to the theoretical results of Eqn. (3.32). All measured values

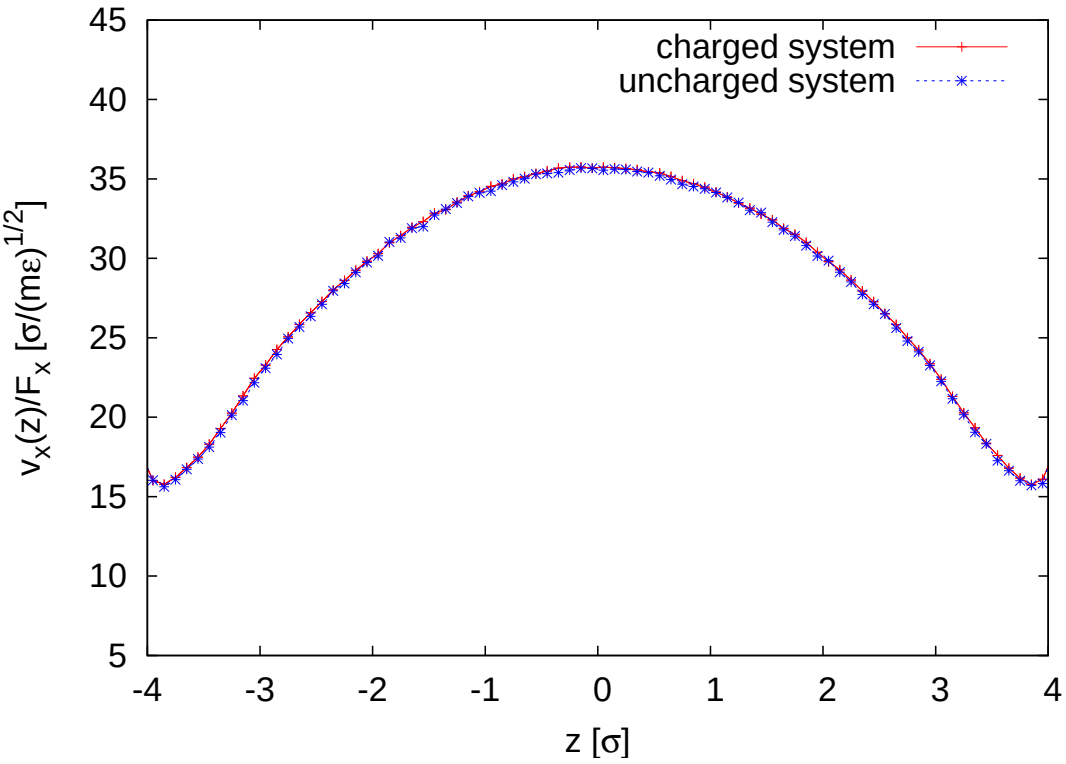

Figure 4.4: Plane Poiseuille Flow with partial-slip boundary conditions ($\gamma_L = 0.96\sigma^{-1}(m\epsilon)^{1/2}$) for a combination of counterions and solvent in contrast to an uncharged fluid Plane Poiseuille Flow. The shear viscosity is derived by a parabolic fit on the flow profile to $\eta_s = (1.334 \pm 0.003)\sigma^{-2}(m\epsilon)^{1/2}$.

are in good agreement to the theory. The hydrodynamic boundary positions determined by the same methods are at $|z_B| = (3.866 \pm 0.265)\sigma$ which roughly corresponds to the results derived in section 3.8.1. The identical value of the shear viscosity was applied in the LB simulations.

Diffusion coefficient

As it was discussed in section 4.4, the effective single diffusion coefficient D has to be calculated for a single tracer particle in the DPD-method and has to be matched to the results of the LB method afterwards. The diffusion coefficient can be calculated by means of a Green-Kubo expression [30] for the velocity autocorrelation function (VACF)

$$D = \frac{1}{3}\int_{t_0}^{\infty} dt < \vec{v}(t)\vec{v}(t_0) > \tag{4.39}$$

$\gamma_L[\sigma^{-1}(m\epsilon)^{1/2}]$	0.96	1.4049	3.1	6.1
δ_B (measured) $[\sigma]$	1.399 ± 0.385	0.782 ± 0.246	0.248 ± 0.231	0.000 ± 0.197
δ_B (Eqn.(3.32)) $[\sigma]$	1.249	0.780	0.226	0.000

Table 4.3: Slip lengths for different layer friction coefficients γ_L. Measured results are compared to the theoretical results of Eqn. (3.32)

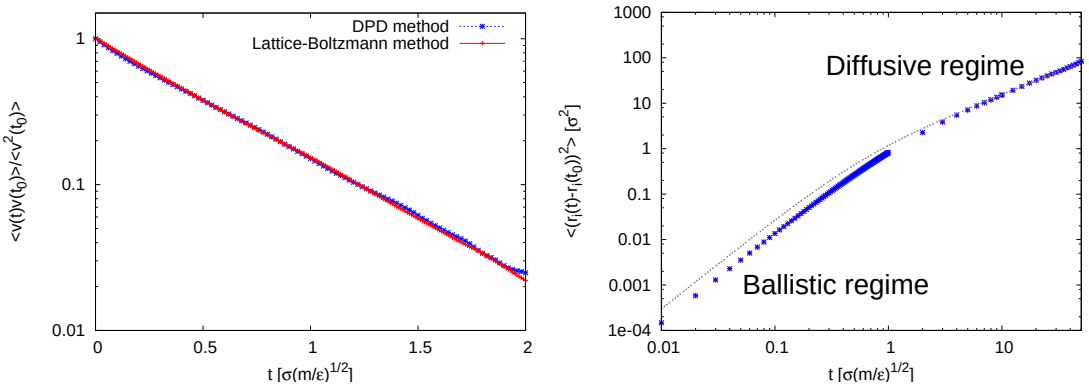

Figure 4.5: **Left:** Normalised velocity autocorrelation function for a DPD-fluid particle with fluid density $\rho = 3.75\sigma^{-3}$, DPD friction coefficient $\gamma_{DPD} = 5.0\sigma^{-1}(m\epsilon)^{1/2}$ and for a LB-fluid particle with identical fluid density and coupling constant $\zeta_{LB} = 1.98\sigma^{-1}(m\epsilon)^{1/2}$. The characteristic decay time for the DPD-method is $\tau_{DPD} = (0.5162 \pm 0.0008)\sigma(m/\epsilon)^{1/2}$ with $D_{DPD} = (0.2581 \pm 0.0004)\sigma^(m/\epsilon)^{-1/2}$ and for the LB-method $\tau_{LB} = (0.5218 \pm 0.0006)\sigma(m/\epsilon)^{1/2}$ with $D_{LB} = (0.2609 \pm 0.0003)\sigma(m/\epsilon)^{-1/2}$. **Right:** Mean square displacement for a fluid DPD particle (blue stars) and for a coupled Langevin/LB particle (red crosses) in comparison to the theoretical prediction. (grey line). The ballistic regime ($\sim t^2$) is given for $0 \leq t \leq 0.75\sigma(m/\epsilon)^{1/2}$ while diffusive behaviour ($\sim t$) takes over at times $t \approx 10\sigma(m/\epsilon)^{1/2}$. The Diffusion constant in DPD is $D_{DPD} = (0.2698 \pm 0.0002)\sigma(m/\epsilon)^{-1/2}$ and for LB $D_{LB} = (0.2617 \pm 0.0005)\sigma(m/\epsilon)^{-1/2}$, calculated by linear regression.

with the corresponding results of $D_{DPD} = (0.2581 \pm 0.0004)\sigma/\sqrt{m/\epsilon}$ and a characteristic decay time of $\tau_{DPD} = (0.5162 \pm 0.0008)\sigma(m/\epsilon)^{1/2}$, which is shown on the left side of Fig. 4.5. The corresponding diffusion coefficient in the LB method can be derived for a coupling constant $\zeta_{LB} = 1.98\sigma^{-1}(m\epsilon)^{1/2}$ with $\tau_{LB} = (0.5218 \pm 0.0006)\sigma(m/\epsilon)^{1/2}$ as the characteristic decay time and $D_{LB} = (0.2609 \pm 0.0003)\sigma(m/\epsilon)^{-1/2}$ for the resulting diffusion coefficient.
An equivalent calculation of the diffusion coefficient D is also possible by

$$D = \lim_{t \to \infty} \frac{< (\vec{r}_i(t) - \vec{r}_i(t_0))^2 >}{6t}. \tag{4.40}$$

	$D[\sigma(m/\epsilon)^{-1/2}](4.40)$	$D[\sigma(m/\epsilon)^{-1/2}](4.39)$	$\eta_s[\sigma^{-2}(m\epsilon)^{1/2}]$	$\rho[\sigma^{-3}]$
DPD	0.2698 ± 0.0002	0.2581 ± 0.0004	1.334 ± 0.003	3.75
LB	0.2617 ± 0.0005	0.2609 ± 0.0003	1.33	3.75

Table 4.4: Diffusion coefficients D of a single tracer particle measured by the mean square displacement and the velocity autocorrelation function, shear viscosity η_s and solvent density ρ for friction coefficients $\gamma_{DPD} = 5.0\sigma^{-1}(m\epsilon)^{1/2}$ and $\zeta_{LB} = 1.98\sigma^{-1}(m\epsilon)^{1/2}$.

which is the mean-square displacement of a single solvent particle [30]. The results are shown on the right side of Fig. 4.5. The full-time mean-square displacement of a single particle can be computed analytically by using the effective friction coefficient $\Gamma_e = k_B T/D$. The mean-square displacement is then given by [96]

$$\begin{aligned} < (\vec{r}_i(t) - \vec{r}_i(t_0))^2 > &= 6\,\frac{k_B T}{m\Gamma_e}t + \frac{<\vec{v}^2(t_0)>}{\Gamma_e^2}(1 - e^{-\Gamma_e t})^2 \\ &\quad -\frac{k_B T}{m\Gamma_e^2}(3 - 4e^{-\Gamma_e t} + e^{-2\Gamma_e t}) \end{aligned} \tag{4.41}$$

which is shown as the grey line in Fig. 4.5 (right side). As standard theories indicate [24], diffusive behaviour dominates over the ballistic regime after a characteristic time which is around $t \geq 10\sigma(m/\epsilon)^{1/2}$ for the chosen parameter sets.
Ballistic motion which is proportional to $\sim t^2$ is found for $0 \leq t \leq 0.75\sigma(m/\epsilon)^{1/2}$ whereas at later times diffusive motion takes over. A linear regression fixes the diffusion coefficient by the mean-square displacement method to $D_{DPD} = (0.2698 \pm 0.0002)\sigma(m/\epsilon)^{-1/2}$ which is in agreement to the Green-Kubo results of Fig. 4.5 (left side). The values of the LB method are given for $D_{LB} = (0.2617 \pm 0.0005)\sigma(m/\epsilon)^{-1/2}$ which is in agreement to the results of the diffusion coefficient derived in the DPD method.
Matching the important hydrodynamic and dynamic parameters in both methods, it is possible to simulate the counterion-induced electroosmotic flow and to compare the results of both methods. Table 4.4 displays all comparable values of the diffusion coefficient and the shear viscosity for the DPD and the LB method.

4.5.3 Counterion distribution in the weak coupling limit

The counterion-induced electroosmotic flow is simulated for several external electric field strengths. The ion density distribution should not be perturbed by the external perpendicular electric field as the left side of Fig. 4.6 for field strengths $E_x = 0.1 - 1.0\epsilon/e\sigma$ indicates. The accessible z-range of the channel between $-4.0\sigma \leq z \leq 4.0\sigma$ due to the finite range of the WCA-interactions is completely filled with a locally varying counterion distribution. Due to the present mediate surface charge density and the resulting coupling constant $\Xi = 1.307$ as presented in Table 4.1, the Poisson-Boltzmann-Theory should be applicable to derive a correct description of the counterion density. The results of the calculation after Eqn. (4.12) with a counterion density in the middle of the

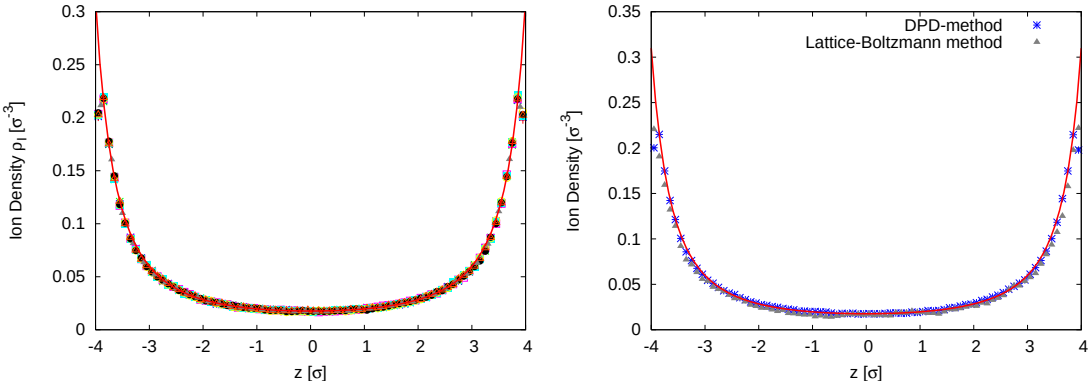

Figure 4.6: **Left:** Counterion density distribution in the fluid between two charged walls for external electric field strengths between $E_x = 0.1{-}1.0 k_B T/e\sigma$. The external perpendicular electric field does not perturb the ion density distribution. The red line presents the theoretical prediction of the Poisson-Boltzmann-Theory (Eqn. (4.12)) for an ion density of $\rho_0 = (0.0176 \pm 0.0001)\sigma^{-3}$ in the middle of the channel. **Right:** Counterion density distribution in the liquid between two charged walls in the Lattice-Boltzmann and the DPD-method. The red line shows the theoretical prediction of Eqn. (4.12).

channel of $\rho_0 = (0.0176 \pm 0.0001)\sigma^{-3}$ are shown as the red line on both sides of Fig. 4.6. The right side of Fig. 4.6 presents the comparison of the DPD- and the Lattice-Boltzmann results for the counterion density. The distribution does not depend on the simulation method as required. To summarise, the ion distribution in terms of the Poisson-Boltzmann theory is reproduced correctly.

4.5.4 Electric field and potential distribution in the weak coupling limit

In addition to the counterion distribution, the electric field $E(z)$ and the electric potential $\psi(z)$ have been measured by a test charge method. The results are shown on the left side of Fig. 4.7 and agree as well as the the counterion distribution to the predictions of the Poisson-Boltzmann theory with Eqn. (4.13) for the electric field. The same can be seen on the right side of Fig. 4.7, where the potential distribution after Eqn. (4.10) inside the channel is shown.
Thus, Poisson-Boltzmann Theory is indeed applicable in the weak coupling regime although the walls are modelled by inhomogeneously charged surfaces. Moderate surface charge densities, as they have been chosen in the simulations, protect the system to differ drastically from the mean field character.

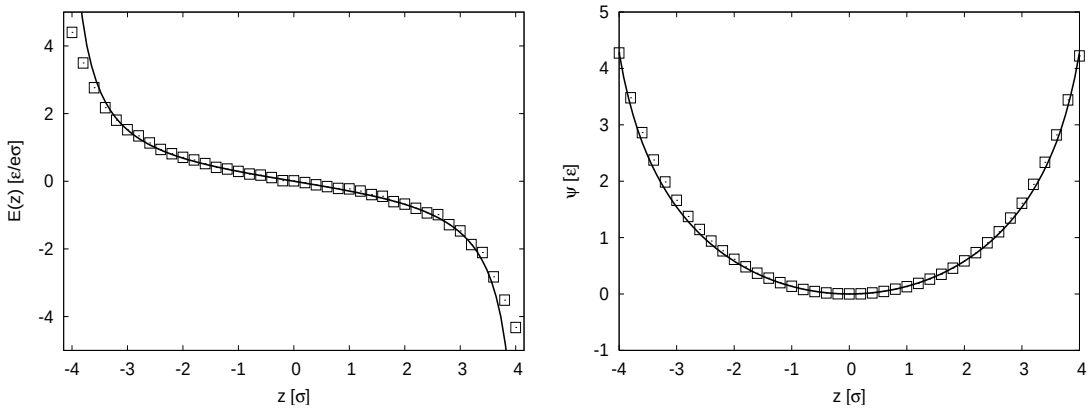

Figure 4.7: **Left:** Electric field $E(z)$ in the solvent measured by a test charge method. The dashed line shows the theoretical prediction of Eqn. (4.13). **Right:** Electric potential $\psi(z)$ in the solvent measured by a test charge method. The dashed line shows the theoretical prediction of Eqn. (4.10).

4.5.5 EOF-profiles in the weak coupling regime

The comparison of the DPD flow profiles together with Eqn. (4.33) in the weak-coupling regime is finally presented in Fig. 4.8 for varying field strengths E_x and several slip lengths.
Important parameters for a direct comparison of the EOF in different simulation methods are the position of the hydrodynamic boundaries z_B and the slip length δ_B. In section 3.8.1 it was shown, that the hydrodynamic boundary position of the DPD method strongly depends on the DPD friction coefficient γ_{DPD} and the fluid density. The slip lengths of Table 4.3, hydrodynamic boundary positions $|z|_B = (3.866 \pm 0.265)\sigma$ and the shear viscosity $\eta_s = (1.334 \pm 0.003)\sigma^{-2}(m/\epsilon)^{1/2}$ determined by the Couette and the Plane Poiseuille flow profile have been inserted into Eqn. (4.33) and compared to the simulation results. By performing simulations for field strengths $E_x = 0.8 - 1.0 k_B T/e\sigma$ according to $\delta_B = 0.00\sigma$ and $\delta_B = 0.248\sigma$, it is obvious that the electroosmotic mobility $\mu_{EOF} = v_x(z)/E_x$ remains constant for several values of the electric field as it was claimed in Eqn. (4.33).
It comes out that a slight increase of the slip length shifts the magnitude of the flow profiles drastically. The comparison of the DPD- and the LB-method flow profiles is finally presented in Fig. 4.9.
The corresponding hydrodynamic boundary position in the Lattice-Boltzmann method is at $|z_B| = 4.0\sigma$. This value differs to DPD where the hydrodynamic boundary positions are located at $|z_B| = (3.866 \pm 0.265)\sigma$.
To match both simulation methods, the effective channel width for the solvent is shifted in the DPD method to 8.28σ by keeping the global densities constant. Thus, the effective range of the tunable-slip interactions increases from 1 to 1.14σ. Following the

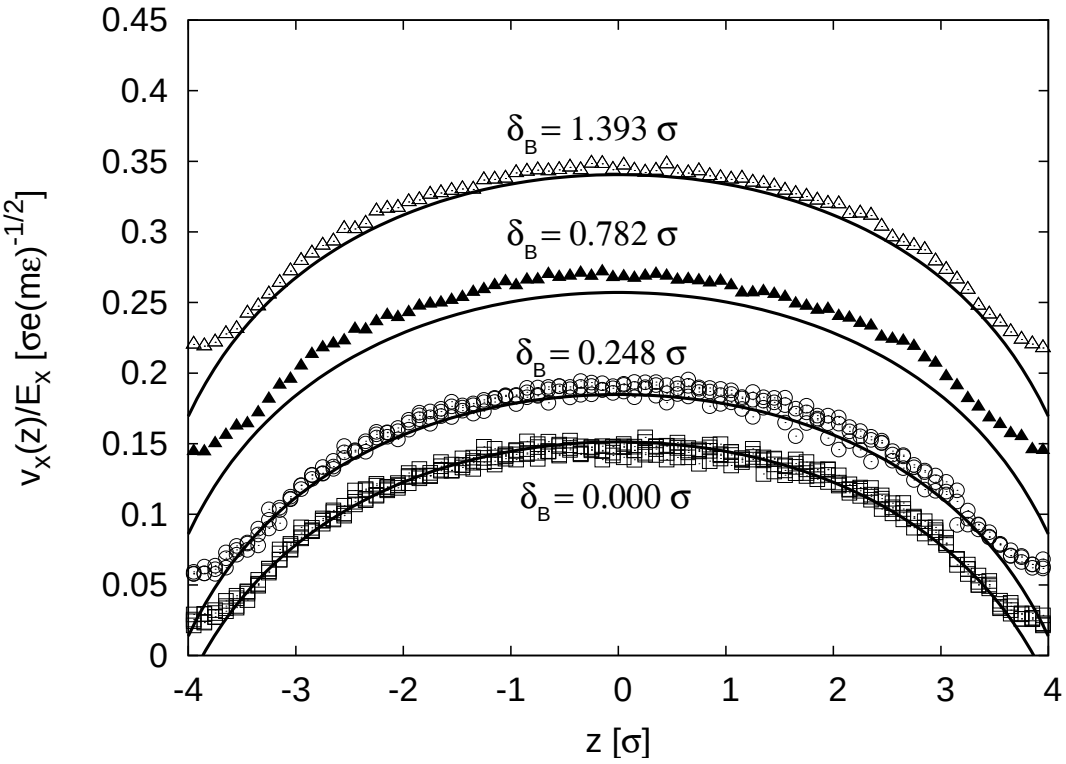

Figure 4.8: Flow profiles for the DPD- method with various field strengths $E_x = 0.8 - 1.0\epsilon/e\sigma$ for varying slip lengths in the weak coupling regime ($\Xi_{WC} = 1.31$). The hydrodynamic boundary positions for the DPD-method are at $|z_B| = (3.866 \pm 0.265)\sigma$. The straight lines represent the theoretical prediction of Eqn.(4.33).

analytic theory of Eqn. (3.32), this has to be combined with the weighting function $\omega_L(z) = (1 - z_i/z_c)$ and the corresponding modified effective cutoff radius $z_c = 1.14$. Inserting the corresponding values into Eqn. (3.32) and assuming no-slip boundary conditions leads to a layer friction coefficient of $\gamma_L = 3.46\sigma^{-1}(m\epsilon)^{1/2}$.
By independent DPD Plane Poiseuille and Plane Couette flow profiles, the slip length for this parameter set was determined to $\delta_B = (0.000 \pm 0.357)\sigma$ and the hydrodynamic boundary positions to $z_B = (4.030 \pm 0.357)\sigma$.
As Fig. 4.9 indicates, the flow profiles of both methods can therefore be tuned to be identical in the no-slip regime and in agreement to Eqn. (4.33) with the inserted values of $\delta_B = 0.0\sigma$ and $|z_B| = 4.0\sigma$. The slight differencies for $|z| \geq 3\sigma$ are artefacts of the tunable- slip boundary interactions, as it has been explained in section 3.1.
To summarize, the proposed mapping scheme is valid and the presented analytical theory for the counterion-induced electroosmotic flow in the weak-coupling regime is correct.

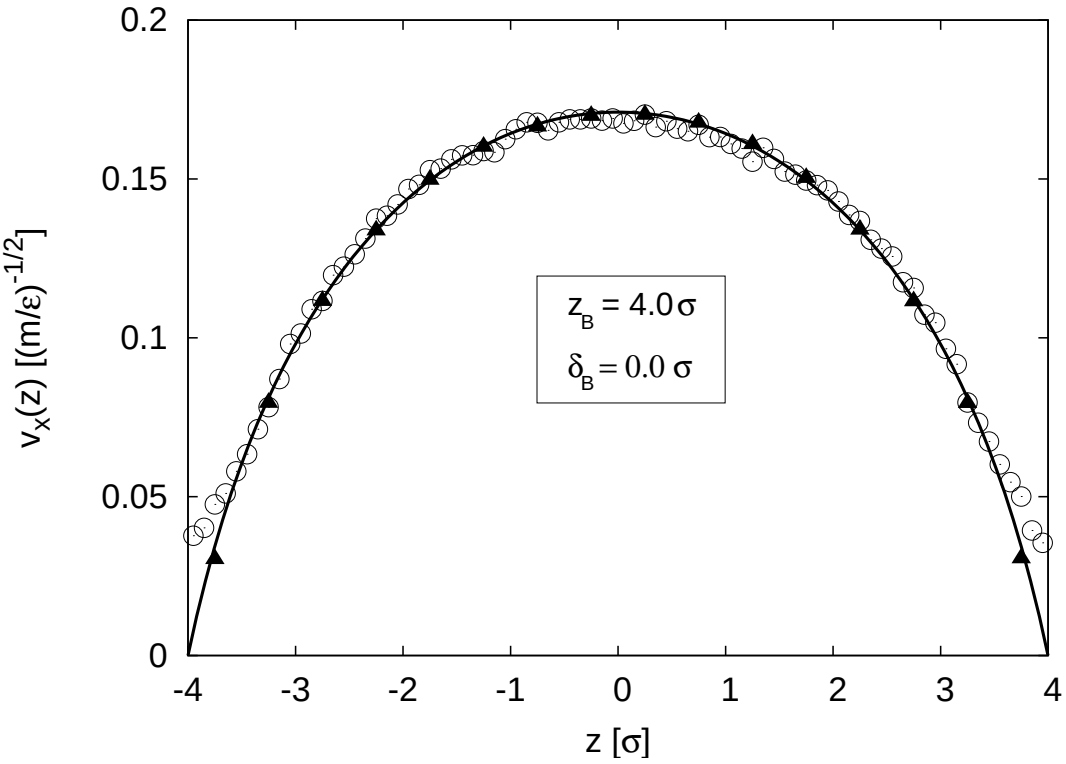

Figure 4.9: Flow profile for the DPD-(circles) and the LB-method (triangles) with no-slip boundary conditions and $E_x = 1.0\epsilon/e\sigma$. The straight line is the theoretical prediction of Eqn. (4.33) with $|z_B| = 4.0\sigma$ and $\delta_B = 0.0\sigma$.

4.6 Comparison between homogeneously and inhomogeneously charged walls

A question that remains is the influence of inhomogeneously, respectively homogeneously charged walls. All the results shown before are derived by placing discrete charges at the walls. As it has been mentioned in section 4.1.2, the counterion distribution is created by a combination of entropic arguments in addition to the electrostatic interaction between the counterions. Nevertheless, the calculation of the potential between two homogeneously and equally charged surfaces yields a constant value. Therefore homogeneously charged walls can easily be created by letting the walls uncharged.
The DPD simulations have been performed together with the MMM2D-algorithm [37] and the parameters given in Table 4.1 of the weak-coupling (Poisson-Boltzmann) regime. LB simulation results have not been investigated due to the special case of applying only no-slip boundary conditions. The ion density ρ_c is $0.0525\sigma^{-3}$ in all simulations.
Fig. 4.10 displays the results of the counterion distribution in the channel for homogeneously and inhomogeneously charged surfaces. The distribution is only slightly per-

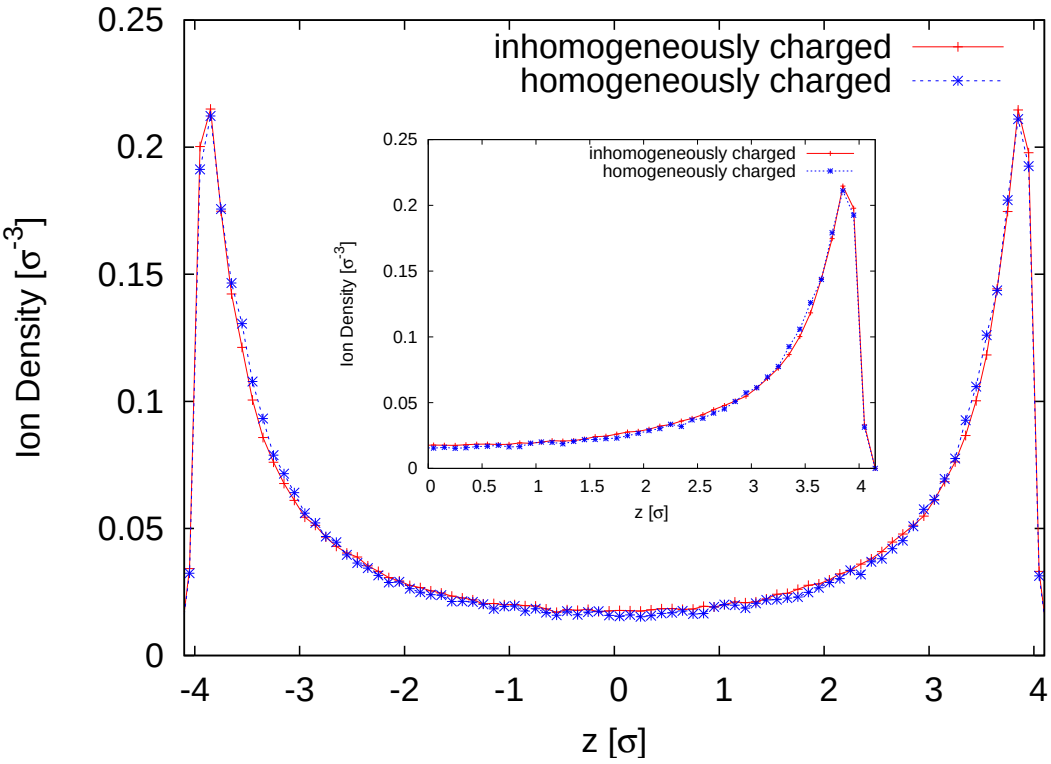

Figure 4.10: Counterion distribution with $\rho_c = 0.0525\sigma^{-3}$ for homogeneously and inhomogeneously charged walls in the weak-coupling regime. Slight deviations can be seen due to closely packed particles and the resulting excluded-volume interactions at inhomogeneously charged walls.

turbed by inhomogeneously charged walls due to the excluded-volume of the particles and the remaining attraction of the fixed discrete charges in the wall. This results in a slightly lower counterion density in the middle of the channel ρ_0 and a corresponding slightly larger counterion density in close vicinity to the channel walls for homogeneously charged surfaces.

Fig. 4.11 presents the corresponding results of the counterion-induced EOF for various slip lengths, in comparison of homogeneously and inhomogeneously charged walls and the corresponding values of Eqn. (4.33), with the same paramters applied as in Fig. 4.8. As it can be seen, it is not relevant if homogeneously and inhomgeneously charged walls are used for an external field strength of $E_x = 1.0\epsilon/e\sigma$ in the weak-coupling regime with $\Xi_{WC} = 1.307$. Electrostatic friction, which lowers the magnitude of the flow profiles is therefore not a significant effect in the weak coupling regime.

The previous results are therefore not inconsistent with the simulation results reported for the strong couling regime [97, 98]. It can be stated that electrofriction influences the flow profiles solely in stronger coupled electrostatic regimes with drastically larger cou-

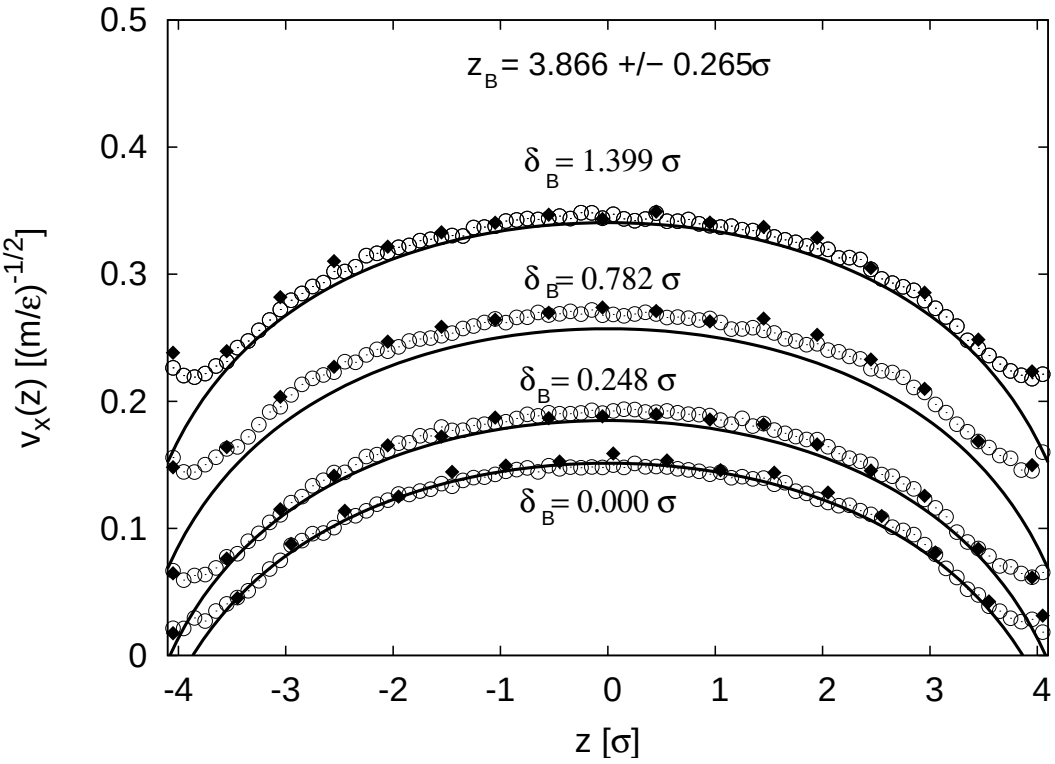

Figure 4.11: Flow profile for various slip lengths with homogeneously (circles) and inhomogeneously charged walls (black diamonds) and $E_x = 1.0\epsilon/e\sigma$ in the weak-coupling regime in comparison to the theoretical prediction of Eqn. (4.33).

pling constants Ξ. Homogeneously charged walls are therefore no specific requirement to achieve results in agreement to the analytical theory of Eqn. (4.33).

4.7 EOF-profiles in the intermediate coupling regime

In addition to the weak coupling regime, it is also interesting to investigate the dynamical behaviour in the intermediate coupling regime. As it was reported in section 4.2, a complete analytical calculation of the counterion density is still missing, although a promising approach has recently been published [99].
The comparability even in non analytic coupling regimes is an important question for the corresponding methods to test their applicability and validity. The comparison of the methods in the intermediate regime will be published in the future due to a lack of LB data [101].
The DPD simulations have been performed for divalent ions with the parameters given in Table 4.1 and a coupling constant $\Xi_{IC} = 4.189$. The parameters for the solvent remain

unchanged. The corresponding counterion density distribution is shown in Fig. 4.12

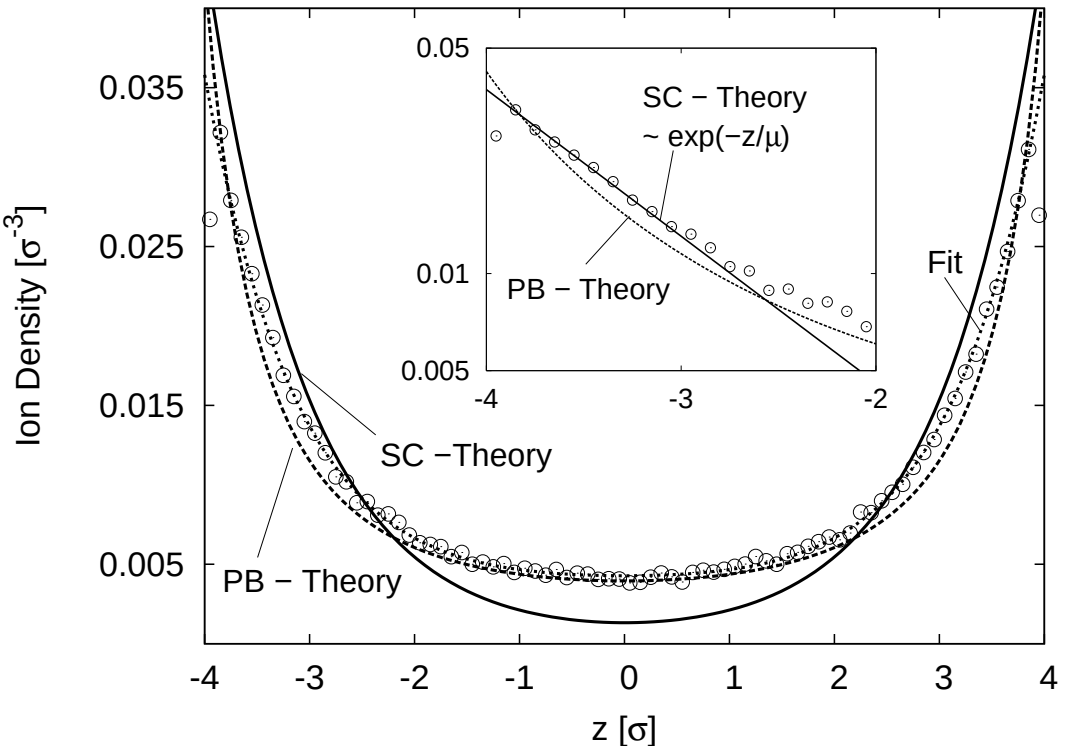

Figure 4.12: Counterion density distribution with $\rho_c = 0.0104\sigma^{-3}$ in the intermediate coupling regime with $\Xi_{IC} = 4.189$ for a surface ion density $\sigma_s = 0.042\sigma^{-2}$. The straight line shows the theoretical prediction of the strong-coupling limit (Eqn. (4.37)). Either strong coupling (straight line) nor Poisson-Boltzmann theory (dashed line) is able to reproduce the results exactly. The fit function is represented by the dotted line. **Inset:** Blowup of the z-range between -4.0 and -2.0σ in a logarithmical plot. The counterion density distribution decays exponentially proportional to the Gouy-Chapman length of $\mu = 0.955\sigma$.

where the results are not predictable by the strong coupling theory (Eqn. (4.37)), which is the straight line as well as for the Poisson-Boltzmann-Theory (Eqn. (4.12)) which is the dashed line. As the inset of Fig. 4.12 further shows, the decay of the counterion distribution at the walls obeys an exponential decay with the Gouy-Chapman length $\mu = 0.955\sigma$ (Eqn. (4.36)) as an indication for highly adsorbed counterions. This follows the predictions of the SC-Theory (Eqn. (4.37)) although a better description in the middle of the channel is given by the Poisson-Boltzmann theory with Eqn. (4.12), in agreement to [95]. Thus the intermediate regime includes both characteristics of the strong coupling- and the Poisson-Boltzmann regime.

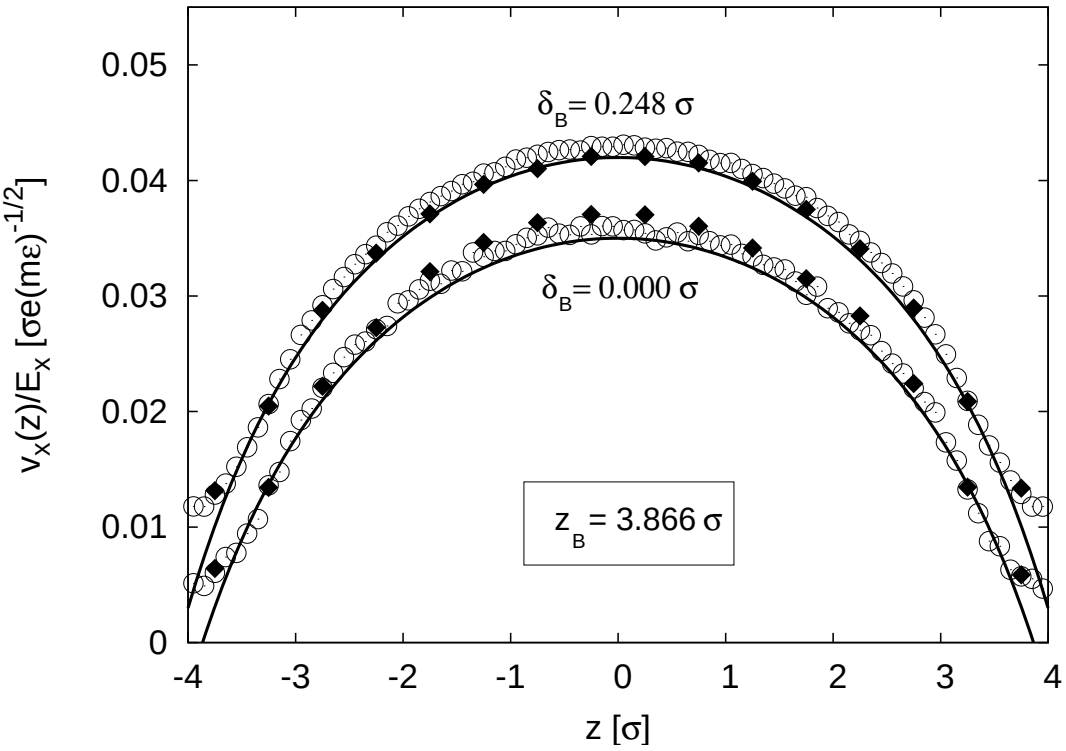

Figure 4.13: Counterion induced electroosmotic flow for the intermediate regime ($\Xi_{IC} = 4.189$) with $\rho_c = 0.0104\sigma^{-3}$, $E_x = 10.0\epsilon/e\sigma$ and surface ion density $\sigma_s = 0.042\sigma^{-2}$ with $\gamma_L = 6.1\sigma^{-1}(m\epsilon)^{1/2}$ ($\delta_B = (0.000 \pm 0.197)\sigma$) and $\gamma_L = 3.1\sigma^{-1}(m\epsilon)^{1/2}$ ($\delta_B = (0.248 \pm 0.231)\sigma$) for homogeneously (filled diamonds) and inhomogeneously charged walls (circles). The straight line shows the calculated flow profile for $|z_B| = 3.866\sigma$ and the corresponding slip lengths by integration of Eqn. (4.43)

This coincides with the results reported in [95, 100] where it has been shown that in the case of a single charged plate in the range

$$\sqrt{\Xi_{IC}} < z/\mu < \Xi_{IC} \tag{4.42}$$

neither Poisson-Boltzmann nor SC-Theory is applicable. Inserting the values of $\Xi_{IC} = 4.189$ and $\mu = 0.955$ in Eqn. (4.42) gives $z > 2\sigma$ respectively $z < -2\sigma$ in agreement to the results of Fig. 4.12.
Although no analytical theory is applicable, a purely heuristic test function, whose functional form is inspired by the predictions of the strong coupling theory (Eqn. (4.37))

$$\rho_c^t(z) = \rho_{(1)}^t \left(e^{-(z-d/2)/\mu} + e^{(z+d/2)/\mu} \right) + f_{corr}(z) \tag{4.43}$$

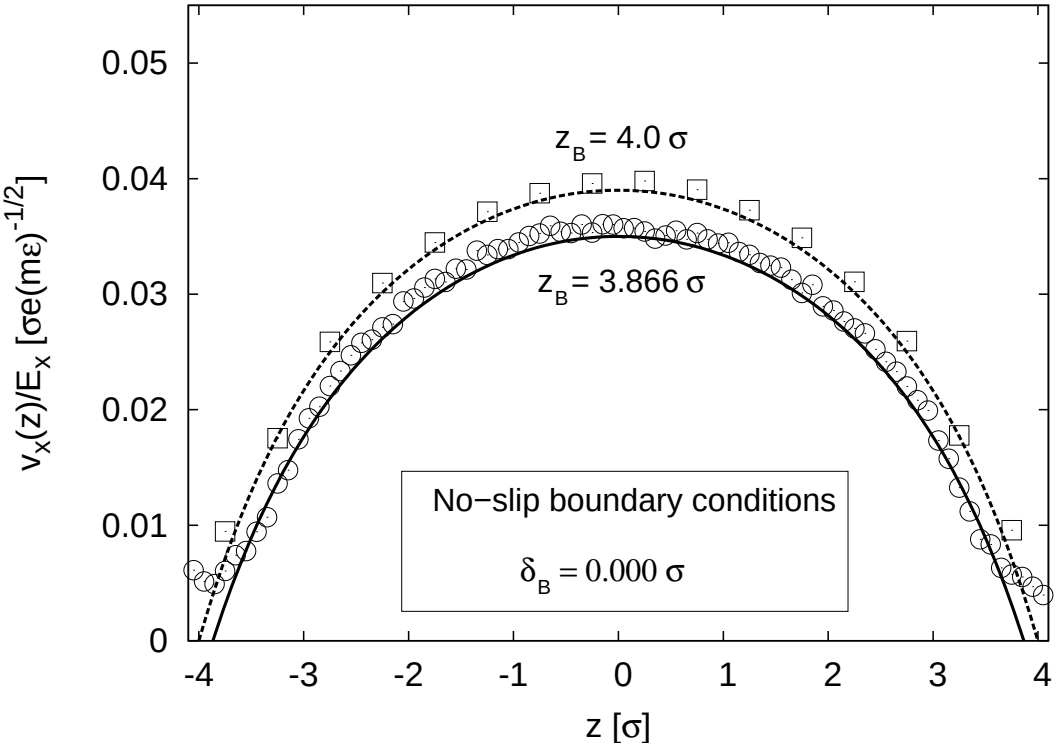

Figure 4.14: Counterion induced electroosmotic flow for the intermediate regime ($\Xi_{IC} = 4.189$) with $\rho_c = 0.0104\sigma^{-3}$, $E_x = 10.0\epsilon/e\sigma$ and surface ion density $\sigma_s = 0.042\sigma^{-2}$ with no-slip boundary conditions by $\gamma_L = 6.1\sigma^{-1}(m\epsilon)^{1/2}$ ($z_B = 3.866\sigma$, $\delta_B = (0.000 \pm 0.197)\sigma$) (circles) and $\gamma_L = 3.46\sigma^{-1}(m\epsilon)^{1/2}$ for an effective channel width of 8.24σ ($z_B = 4.0\sigma$, $\delta_B = (0.000 \pm 0.357)\sigma$) (squares). The straight line shows the calculated flow profile for the corresponding hydrodynamic boundary conditions.

with the fit parameter $\rho^t_{(1)}$ and the correction $f_{corr}(z)$, can be used to give an estimate for the counterion density. A good fit can be obtained by

$$f_{corr}(z) = \rho^t_{(2)} \cos(\phi z) \tag{4.44}$$

with the additional fit parameters ϕ and $\rho^t_{(2)}$. Applying the fit values

$$\rho^t_{(1)} = (8.31 \pm 0.10) \cdot 10^{-6}\sigma^{-3}$$

$$\rho^t_{(2)} = (3.18 \pm 0.05) \cdot 10^{-3}\sigma^{-3}$$

and

$$\phi = (0.416 \pm 0.022)\sigma^{-1}$$

yields the dotted line in Fig. 4.12. Fig. 4.13 finally presents the results for the EOF profile in the intermediate regime.
Integrating the counterion density by inserting Eqn. (4.43) into the Stokes equation (Eqn. (3.13)) and using the partial-slip boundary conditions (Eqn. (3.4)) yields the black line which nicely reproduces the numerical results with the parameters given in the caption. This result demonstrates that the Stokes equation (Eqn. (3.13)) is even valid in the intermediate coupling regime. Thus the boundary conditions of $|z_B| = (3.866 \pm 0.265)\sigma$ and the proposed slip lengths as obtained in the weak coupling regime remain unchanged. Even the influence of inhomogeneously charged surfaces does not lead to noticeable effects on the flow profiles, as Fig. 4.13 further indicates.
Fig. 4.14 displays the results for the intermediate EOF profiles for varying hydrodynamic boundary positions z_B. As in the weak-coupling regime (section 4.5.5), the effective channel width was shifted to 8.24σ, which results in varying boundary conditions $z_B \approx 4.0\sigma$. Inserting the unchanged values of Eqn. (4.43) and integrating the Stokes equation with partial-slip boundary conditions (Eqn. (3.4)) for $z_B = 4.0\sigma$ produces the dashed line, which is in good agreement to the numerical results. An exact agreement with the forthcoming LB simulations results is expected for this flow profile, if both methods are comparable even in non analytic coupling situations.
Summarising the results, mesoscopic simulation methods are powerful tools to reproduce the counterion-induced electroosmotic flow in good agreement to the analytical expressions in presence of no-slip as well as partial-slip boundary conditions. It has been shown, that the value of the slip length changes the magnitude of the profile drastically, even in presence of small slip lengths. This is in agreement with the predictions of Barrat *et al.* [65] and may facilitate flow profiles and its applications that could benefit on that. Perturbations which are related to inhomogeneously charged walls are minor effects which do not change the counterion distribution and the corresponding flow profiles in the Poisson-Boltzmann limit significantly. Therefore the effects of electrofriction are negligible in all previously considered coupling regimes.
A test function allows to fit the counterion distribution in the intermediate coupling regime although detailed analytic results are missing. Integrating this function with the corresponding parameter values in terms of the Stokes equation allows to predict the numerical results in good agreement to the theory. It is pointed out, that the coupling of electrohydrodynamic effects can be well calculated by standard theories even in non analytic coupling situations.
Comparing the different simulation methods, LB method and Dissipative Particle Dynamics show identical results in the weak coupling regime. This validates the presented mapping scheme.

5 Polymers and polyelectrolytes in free salt solution

Energy derives from both - the plus and negative.
- James Hetfield (1988)

Most macromolecules of biological relevance like DNA are highly charged polymers which are called polyelectrolytes or polyions. Since scientific progress in biotechnology has grown enormous over the last decades, the research on new and efficient separation techniques has become an important field in experimental as well as theoretical sciences [1]. Standard techniques for size dependent separation like gel-electrophoresis exploit the high charging of the macromolecule. Indeed the application of an external electric field is an easy task, which explains the broad use of these methods.
Although standard gel methods are versatile, the length dependent separation of DNA strands up to ~ 40000 was found to be impossible for these methods [102]. Furthermore it has been reported, that in general DNA length separation in gel electrophoresis is inefficient for more than 20000 base pairs [103]. The understanding of the dynamical behaviour of polyelectrolytes in free and confined salty solution to overcome this situation is nowadays an important challenge in soft matter sciences. Whereas the theory of gel-electrophoresis is well-understood, less is known about possible length dependent separation approaches in liquid solution [1].
The naive approach to apply an external electric field in free solution is easy to manage but unfortunately does not lead to a size- or shape dependent electrophoretic mobility of the polyelectrolyte [3, 4]. The diffusive behaviour of polyelectrolytes in a non-electric external field is dominated by hydrodynamic interactions between the monomers [1]. The polyelectrolyte behaves as a massive object which migrates in sense of a large Stokes sphere. The diffusion coefficient D_{cm} is therefore proportional to [1]

$$D_{cm} \sim \frac{1}{R_g} \sim N^{-\nu} \tag{5.1}$$

depending on the radius of gyration R_g, which gives an estimate of the average distance of a single monomer N_i to the center of mass. The dynamical behaviour of polymers with hydrodynamic interactions is called *Zimm-Dynamics* [104].
The calculation of the excluded-volume parameter ν in Eqn. (5.1) for uncharged polymers was first derived by Flory who computed a $\nu = 0.6$ by free energy calculations [105]. More exact renormalisation group theories finally yield a value of $\nu = 0.588$ for uncharged polymers [7].
Instead the situation is different for polyelectrolytes, which are more swollen than the

uncharged polymers due to the repulsive electrostatic interactions between the monomers which results in $\nu > 0.588$. Renormalisation group theories cannot be simply applied for polyelectrolytes, in contrast to uncharged polymers due to the long-range character of electrostatic interactions [4].
This results in a lack of an exact theory, due to the *a priori* unknown influence of the salt concentration and the corresponding electrostatic screening effects[106, 107]. Nevertheless, scaling approaches for polyelectrolytes based on the electrostatic blob size [108, 109] and on the electrostatic persistence length [110, 111] have been published all over the years. In contrast to the complicated configurational behaviour, the dynamical properties in the presence of external electric fields are well understood.
The polyelectrolyte is surrounded by an oppositely charged ion cloud due to the Poisson-Boltzmann theory of ionic solutions (*cf.* chapter 4). An external electric force exerted on the polyelectrolyte is therefore proportional to the number of charged monomers N_c, the applied electric field $\vec{E}$ and the charge Ze of a monomer with $\vec{F} = ZeN_c\vec{E}$. Due to their charge, the polyelectrolyte and its surrounding ion cloud move in opposite directions, corresponding to the electric field such that the net momentum transferred to the solvent adds to zero.
The reason for that is a crucial screening of hydrodynamic interactions within the Debye-Hückel length κ_D^{-1} [1], given in Eqn. (4.26). As a final result, the electrophoretic mobility μ_e is length independent $\mu_e \sim N^0$ due to this electrohydrodynamic screening, which can be incorporated into the diffusion coefficient [1, 7] to

$$D_{cm} \sim \frac{1}{N} \tag{5.2}$$

where each monomer acts as a single Stokes sphere. Regarding Eqn. (5.1), it becomes clear that a totally different behaviour of the polyelectrolyte is shown. The dynamical regime for polymers in absence of hydrodynamic interactions is called *Rouse-Dynamics* [112].
The mechanisms of electrohydrodynamic screening have been discussed by Manning in [3]. Barrat and Joanny [4] and later Long and Ajdari [113] derived an expression for the modified Oseen-Tensor which incorporates the mechanisms of screening due to the decay of hydrodynamic interactions on short scales. In summary, the need of an external electric field to explain electrohydrodynamic screening is essential. A detailed description of hydrodynamic interactions and hydrodynamic screening for polymers is presented in sections 5.2 and 5.3.
Numerical results are displayed in this chapter which indicate a crossover from Zimm- to Rouse-Dynamics in absence of external electric fields for short times and certain length scales. To the best of my knowledge, this dynamical transition has not been reported and predicted before. A tentative explanation of this effect is presented. I start with a brief explanation of the properties of polyelectrolytes and polymers in general.

5.1 Static and dynamic properties of polymers

5.1.1 Static properties

As in the methodology of Dissipative Particle Dynamics inherent, the polymers are additionally simulated in a coarse-grained fashion for consistency. Coarse-graining in general means the neglect of atomistic details for specific particles or groups of particles. Coarse-grained polymers are then formed by groups of molecular monomers which are combined to N beads that are connected by $N-1$ stiff springs [112]. Although chemical

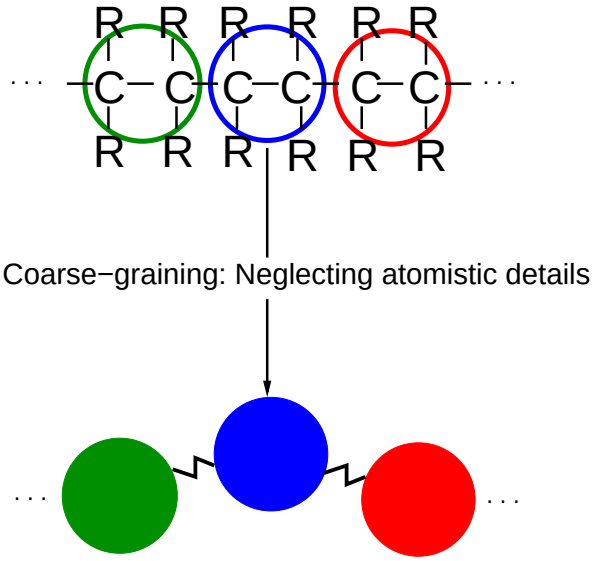

Figure 5.1: Schematic illustration: Coarse-graining a polymer.

details are disregarded, implicit scaling laws derived for long chains and for several observables are still valid [7].
The center-of-mass $\vec{R}_{cm}$ of a polymer is given by adding the bead, respectively monomer positions $\vec{R}_i$ to

$$\vec{R}_{cm} = \frac{1}{N}\sum_{i=1}^{N}\vec{R}_i \tag{5.3}$$

which is directly related to the gyration radius R_g of the chain

$$R_g^2 = \frac{1}{2N^2}\sum_{i,j=1}^{N} < (\vec{R}_i - \vec{R}_j)^2 >= \frac{1}{N}\sum_{n=1}^{N} < (\vec{R}_i - \vec{R}_{cm})^2 > \tag{5.4}$$

by insertion of Eqn. (5.3).
As it was mentioned before, the gyration radius gives an estimate of the monomers average distance to the center of mass of the chain.

The end to end distance R_e of the first and the last monomer is given by

$$R_e^2 = (\vec{R}_N - \vec{R}_1)^2 \tag{5.5}$$

which obeys as well as the gyration radius a power law behaviour

$$R_g^2 \propto R_e^2 \propto N^{2\nu} \tag{5.6}$$

with the monomer number N.
A direct measurement of the exluded-volume parameter ν and further measurements on the dynamical properties can be fulfilled by several scattering or Neutron Spin Echo spectrometry experiments [7, 114]. The static structure factor $S(k,0)$, which can be determined by these methods is given by

$$S(k,0) = \frac{1}{N}\sum_{i,j}^{N} < e^{i\vec{k}(\vec{R}_i(t_0)-\vec{R}_j(t_0))} > \tag{5.7}$$

which scales with the wavenumber $\vec{k}$

$$\vec{k} = \frac{2\pi}{L}\vec{n}, \tag{5.8}$$

where L is the size of the system and the integers of the normal vector are given by $\vec{n}$ to

$$S(k,0) \sim k^{-\frac{1}{\nu}} \tag{5.9}$$

between $1/R_g \ll k \ll 1/a_0$, where a_0 is the smallest microscopic length scale of the polymer [115]. By considering this quantity, it is possible to determine the excluded-volume parameter in experiments, as well as in computer simulations.

5.1.2 Dynamic properties

A large number of quantities can be investigated to characterise the dynamic behaviour of polymers respectively polyelectrolytes. Important methods are the displacement of the central monomer and the overall displacement of the polymer. By considering a polymer that migrates its own gyration radius, the following scaling relations can be obtained.
The longest relaxation time τ that is is needed to migrate the radius of gyration R_g for a single monomer is given by [115]

$$D_{cm}\tau \sim R_g^2 \tag{5.10}$$

with the diffusion coefficient given in Eqn. (5.1), which yields

$$\tau_Z \sim R_g^3 \tag{5.11}$$

for the longest relaxation in the Zimm-regime. If hydrodynamic interactions are absent, the diffusion coefficient D_{cm} is given by Eqn. (5.2) which can be combined with Eqn. (5.6) to

$$\tau_R \sim R_g^{2+1/\nu} \sim N^{2\nu+1} \tag{5.12}$$

for the longest relaxation in the Rouse regime. These exponents appear in the subdiffusive behaviour of the mean square displacement of the central monomer.
On intermediate time scales between microscopic times and longest relaxation times, the dynamical behaviour can then be written in a compact form to

$$g_1 :=< (\vec{R}_i(t) - \vec{R}_i(t_0))^2 >\sim t^{2/z} \tag{5.13}$$

with

$$z = 3 \quad \text{(Zimm-Regime)} \tag{5.14}$$

and

$$z = 2 + 1/\nu \quad \text{(Rouse-Regime)} \tag{5.15}$$

for $t_b \ll t \ll \tau_{R/Z}$, where t_b denotes the ballistic time [116].
The central monomer motion in the center-of-mass system is given by

$$g_2 :=< [(\vec{R}_i(t) - \vec{R}_{cm}(t)) - (\vec{R}_i(t_0) - \vec{R}_{cm}(t_0))]^2 > \tag{5.16}$$

with $g_2 \sim t^0$ for $g_2 \gg R_g^2$.
The overall motion of the polymer is finally defined by the center of mass displacement

$$g_3 :=< (\vec{R}_{cm}(t) - \vec{R}_{cm}(t_0))^2 >= 6D_{cm}t \tag{5.17}$$

with the diffusion constant D_{cm} for consistency. The diffusion constant gives a rough estimate for the Zimm-, respectively the Rouse time by

$$\tau_{R/Z} = \frac{R_g^2}{6D_{cm}} \tag{5.18}$$

as the longest relaxation time in polymer dynamics.
Further investigation of chain dynamics is possible by applying a Rouse-Mode analysis. The Rouse-Function is defined by [7, 117]

$$\vec{X}_p = \frac{1}{N}\sum_{i=1}^{N} \vec{R}_i \cos\left(\frac{p\pi}{N}\left(i - \left(\frac{1}{2}\right)\right)\right) \tag{5.19}$$

with the Rouse-Mode p, whose time autocorrelation function is given by

$$< \vec{X}_p(t)\vec{X}_q(t_0) >=< \vec{X}_p(t_0)\vec{X}_q(t_0) > \delta_{pq}\, e^{-\Gamma(p)t} \tag{5.20}$$

under the assumption that the motion is diffusive [112]. The decay factor $\Gamma(p)$ is proportional to

$$\Gamma^Z(p) \sim \left(\frac{p}{N}\right)^{3\nu}, \tag{5.21}$$

for Zimm-Dynamics, whereas Rouse-Dynamics is given for

$$\Gamma^R(p) \sim \left(\frac{p}{N}\right)^{2\nu+1} \tag{5.22}$$

which is shown in appendix B. Comparing the exponents of Eqns. (5.21) and (5.22), it is obvious that for a detailed distinction of dynamical regimes using the Rouse modes, the exluded volume parameter ν has to be small with $\nu \ll 1$.
The dynamic version of the structure factor (Eqn. (5.7)) is finally defined by

$$S(k,t) = \frac{1}{N}\sum_{i,j} < e^{i\vec{k}(\vec{R}_i(t)-\vec{R}_j(t_0))} > . \tag{5.23}$$

For the inverse length scale $1/R_g \ll k \ll 1/a_0$ and the finite time interval $t_b \ll t \ll \tau_{R/Z}$, the dynamic structure factor obeys the following scaling relation [115, 26]

$$S(k,t) = S(k,0)f(k^z t) \tag{5.24}$$

after the ballistic time t_b, where z has been defined in Eqns. (5.14) and (5.15). Again, for a detailed distinction of the dynamical regimes, the excluded-volume parameter has to obey $\nu \ll 1$.

5.2 Hydrodynamic interactions and screening

Particles immersed in a solvent interact, in addition to interparticle forces, due to indirect hydrodynamic interactions as a dominant factor influencing their dynamics. A schematic

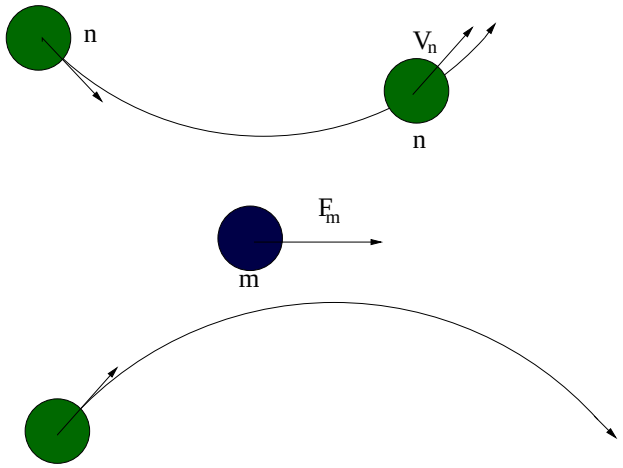

Figure 5.2: Schematic illustration of hydrodynamic interactions of a particle m by creating a flow field that influences other particles in the vicinity.

illustration of this situation is shown in Fig. 5.2. The blue particle m starts to move and

creates a velocity field. This velocity field influences the motion of other particles in the vicinity. The mathematical description of hydrodynamic interactions is given in terms of the Stokes equation

$$\eta_s \Delta \vec{v} = \vec{\nabla} P - \sum_n \vec{F} \delta(\vec{r} - \vec{R}_n) \tag{5.25}$$

with the condition of $\vec{\nabla}\vec{v} = 0$. Solving by transformation into Fourier-Space yields

$$\vec{v}(\vec{k}) = \mathbf{H}(\vec{k})\vec{F}(\vec{k}) \tag{5.26}$$

with the Oseen-Tensor

$$\mathbf{H}(\vec{k}) = \frac{1}{\eta_s k^2}\left(\mathbf{1} - \hat{k}\hat{k}\right) \tag{5.27}$$

or by back transformation

$$\mathbf{H}(\vec{r}) = \frac{1}{8\pi\eta_s r}(\mathbf{1} + \hat{r}\hat{r}) \tag{5.28}$$

into the corresponding cartesian space with $\hat{k} = \vec{k}/k$ respectively $\hat{r} = \vec{r}/r$ [7].
It is obvious in Eqn. (5.28), that hydrodynamic interactions, whose strength is given by the Oseen tensor, decay inversely proportional to the distance between the objects.
If now a highly charged object like a polyelectrolyte is placed in salty solution, the surrounding ions form an atmospheric cloud. The width of this cloud can be roughly estimated by means of the Debye-Hückel screening length κ_D^{-1} (Eqn. (4.26)). In absence of external electric fields, standard theories indicate [1] that the polyelectrolyte builds up hydrodynamic interactions which decay as $1/r$, like it was shown in Eqn. (5.28) and which massively determine the dynamical behaviour.
Fig. 5.3 presents this situation in a schematic illustration. As the diffusion coefficient indicates (Eqn. (5.1)), the polymer behaves as a single rigid sphere. Standard theories predict for this case, that even external non-electrostatic forces cannot perturb this characteristic dynamical behaviour. The situation is completely different if an external electric field is switched on.
In presence of this field, the polyelectrolyte migrates in an effect called *electrophoresis* in the direction of the electric field. In addition, the surrounding counterion cloud is disturbed by the external force and starts to move in the opposite direction, called *electroosmosis* (*cf.* chapter 4).
Both effects achieve two rivaling directions of the particles in the counterion cloud which erase each other effectively by a zero net momentum transfer (Fig. 5.4). This results in a screening of hydrodynamic interactions between the monomers. The polyelectrolyte behaves as a combination of N rigid spheres and the diffusion coefficient D_{cm} is given by Eqn. (5.2).
A similar screening behaviour, but with different origins can be observed for immersed particles with surrounding obstacles [113] or polymers in dense polymeric solutions [118].
The results of this chapter focus on the dynamics of polyelectrolytes in absence of external electric fields. Approaches to describe hydrodynamic screening for polymers in general are presented in the next section.

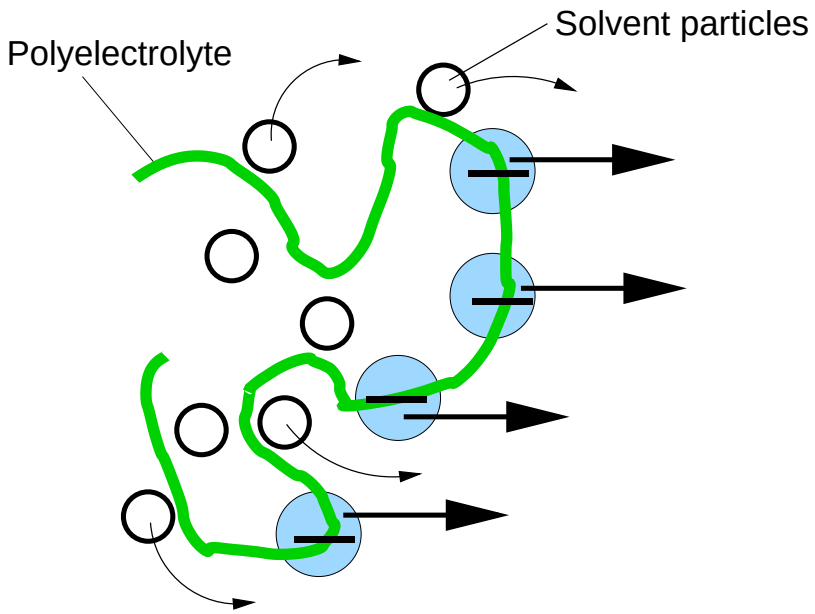

Figure 5.3: Schematic illustration of hydrodynamic interactions of a polyelectrolyte in absence of external electric field by neglecting the surrounding counterions. Hydrodynamic interactions in the solvent build up which lead to a diffusive behaviour $D_{cm} \sim R_g^{-1}$.

5.3 Hydrodynamic screening in polymeric solutions

Much analytical and numerical work on the topic of hydrodynamic screening for polymers has been published over the years. In general two main screening effects for polyelectrolytes are known, which are related to dense polymeric solutions and polyelectrolytes in external electric fields. The origins of electrohydrodynamic screening in electrophoresis have been explained in the last section, whereas the fundaments of this theory have been published in [3, 4].
A description of hydrodynamic screening in dense polymer solutions was first explained in terms of the *effective-medium theory* by S. F. Edwards [7].
Taking only one polymer into account, the surrounding polymeric solution is described by an unknown response function which acts on the considered polymer. The presence of various polymers change the intrinsic viscosity of the solvent

$$[\eta] = \lim_{\phi \to 0} \frac{\eta - \eta_s}{\eta_s \phi}, \tag{5.29}$$

which in first order corresponds to

$$\eta^* = \eta_s(1 + \phi[\eta]) \tag{5.30}$$

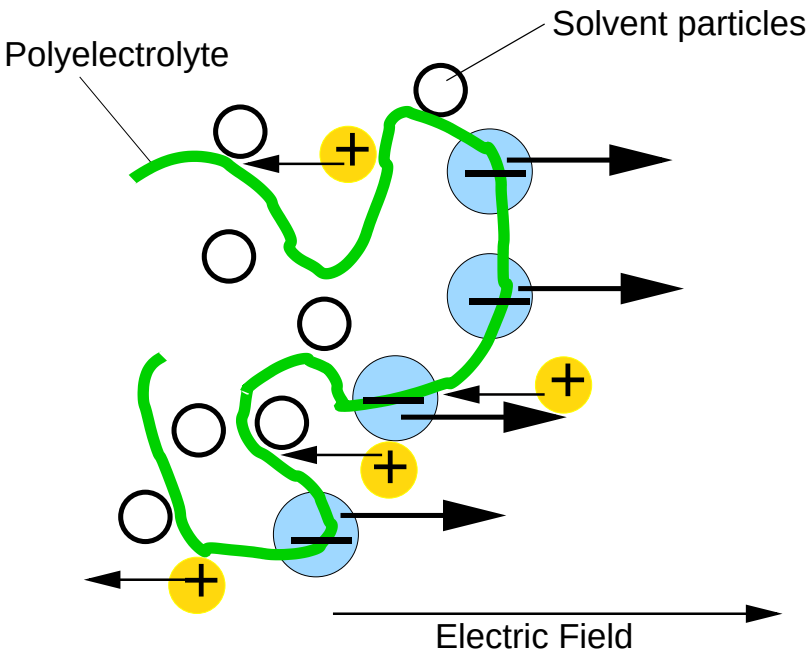

Figure 5.4: Schematic illustration of screening of hydrodynamic interactions of a polyelectrolyte in presence of external electric fields with counterions. Hydrodynamic interactions are screened in the solvent which leads to a diffusive behaviour $D_{cm} \sim N^{-1}$.

with the *a priori* unknown function $\phi[\eta]$. The general perturbed velocity of the single polymer $\tilde{v}(\vec{r})$ due to the presence of other polymers in close vecinity, can be expressed by

$$\tilde{v}(\vec{r}) = \vec{v}_0(\vec{r}) + \delta\tilde{v}(\vec{r}) = \vec{v}_0(\vec{r}) - \frac{c}{N}\int d\vec{r}'\Sigma(\vec{r}-\vec{r}')\tilde{v}(\vec{r}') \tag{5.31}$$

with the concentration of polymers c and the unknown response function $\Sigma(\vec{r}-\vec{r}')$, which includes the effect of the surrounding medium due to a perturbation $\delta\tilde{v}(\vec{r})$.
This can be written in terms of a Fourier-transformation to

$$\tilde{v}(\vec{k}) = \frac{\vec{v}_0(\vec{k})}{1+\frac{c}{N}\Sigma(\vec{k})} = \tilde{\mathbf{H}}(\vec{k})\vec{F} \tag{5.32}$$

with the modified Oseen-Tensor

$$\tilde{\mathbf{H}}(\vec{k}) = \frac{1}{\left(1+\frac{c}{N}\Sigma(\vec{k})\right)}\mathbf{H}(\vec{k}) \tag{5.33}$$

under the assumption that the Stokes equation is valid. Eqn. (5.33) can be combined with Eqn. (5.27) to

$$\tilde{\mathbf{H}}(\vec{k}) = \frac{1}{\eta^*(\vec{k})k^2}\left(\mathbf{1}-\hat{k}\hat{k}\right). \tag{5.34}$$

Comparison with Eqn. (5.30) gives

$$\eta^*(\vec{k}) = \eta_s \left(1 + \frac{c}{N}\Sigma(\vec{k})\right) \tag{5.35}$$

for the local varying viscosity. This leads to a faster exponential decay of hydrodynamic interactions which can be seen by back transformation into the corresponding cartesian space.
Although this attempt explains hydrodynamic screening in polymer solutions, computer simulations [118] have shown that a more complicated time-dependent behaviour arises in this specific topic.
Ahlrichs *et al.* [118] have simulated dense polymeric solutions in a Lattice-Boltzmann fluid. They found ordinary hydrodynamic behaviour for short times, whereas the screened behaviour sets in after a characteristic time. An important criterion for this transition is the hydrodynamic blob size ζ_H [117]. The concentration dependence of the blob size is expressed by

$$c \sim \zeta_H^{-3}(\zeta_H/a_0)^{1/\nu} \tag{5.36}$$

where a_0 is the smallest length scale in the polymer and c is the concentration of the polymeric solution.
Hydrodynamic screening was reported in [118] to set in after the polymer migrates its own blob size. Scaling relations in comparison to the numerical results have shown, that the interaction with the surrounding polymers takes place beyond this limit. Due to the collisions of the polymer chains, hydrodynamic interactions between the monomers are screened which results in a faster decay of hydrodynamic interactions, in agreement to the effective-medium theory.
A mathematical analogy of this effect can be given in terms of the Darcy flow equation

$$\rho\frac{\partial}{\partial t}\vec{v} = \eta_s\Delta\vec{v} - \xi c\vec{v} \tag{5.37}$$

with the friction coefficient ξ, that can be applied if fixed obstacles exert additional friction on a fluid flow. The following identity $\xi c = \eta_s\zeta_H^{-2}$ was shown for consistency in [118]. The screened Oseen Tensor can then be calculated by the phenomenological Brinkmann equation [113]

$$\eta_s\Delta\vec{v} = \vec{\nabla}P - \rho\vec{F} + \eta_s\zeta_H^{-2}\vec{v} \tag{5.38}$$

with a modified Oseen Tensor in the Fourier space

$$\mathbf{H}(\vec{k}) = \frac{1}{\eta_s(k^2 + \zeta_H^{-2})}(\mathbf{1} - \hat{k}\hat{k}). \tag{5.39}$$

Back transformation into the cartesian space yields an exponentially screened decay of hydrodynamic interactions by

$$\mathbf{H}(\vec{r}) = \frac{1}{8\pi\eta_s r}e^{-\frac{r}{\zeta_H}}(\mathbf{1} + \hat{r}\hat{r}) \tag{5.40}$$

beyond the blob size ζ_H. Summarising the results, the effective-medium theory is applicable if time-dependent screening is neglected. Otherwise it turns out, that the screening of polymeric solutions is much more complicated than assumed and includes all the characteristics of time-dependency.
Turning to polyelectrolytes and hydrodynamic screening in external electric fields, the mathematical framework was first published in [4]. The combined effects of electroosmosis and electrophoresis can be again expressed in terms of the Stokes equation with

$$\eta_s \Delta \vec{v} = \nabla P - (Z_M e \delta(\vec{r}) + \rho_c(\vec{r}))E, \tag{5.41}$$

where the external electric field $\vec{E}$ acts on the monomers with charge $Z_M e$ and on the counterion cloud with charge density ρ_c. Again solving in Fourier space with $\vec{\nabla}\vec{v} = 0$ and inserting the counterion charge density in terms of the Debye-Hückel theory

$$\rho_c(\vec{k}) = -Ze\frac{\kappa_D^2}{\vec{k}^2 + \kappa_D^2} \tag{5.42}$$

into Eqn. (5.41) yields

$$\mathbf{H} = \frac{1}{\eta_s(k^2 + \kappa_D^2)}(\mathbf{1} - \hat{k}\hat{k}) \tag{5.43}$$

which leads to

$$\mathbf{H}(\vec{r}) = \frac{1}{8\pi\eta_s r}e^{-\kappa_D r}(\mathbf{1} + \hat{r}\hat{r}) \tag{5.44}$$

in coincidence to Eqn. (5.40). The reciprocal decay of the hydrodynamic interactions of Eqn. (5.28) is replaced by a faster Yukawa-like decay. Thus, hydrodynamic interactions are effectively screened on length scales $r \gg \kappa_D^{-1}$ and this effect is called *electrophoretic effect*.
In addition to electrohydrodynamic screening, another coupled electrohydrodynamic effect can be observed for polyelectrolytes in salt solution. If a polyelectrolyte sets into motion, the surrounding ion cloud is polarised and slightly distorted due to a delayed movement. This *relaxation effect* [3] acts on the polyelectrolyte and decelerates its motion due to an additional electrostatic friction, where the electric field and its influence on the polyelectrolyte dynamics has to be calculated. The description is independent of the electrophoretic effect and occurs also in absence of external electric fields with the mathematical theory presented in [4].
The surrounding equilibrated ion cloud is assumed to be described in terms of the Debye-Hückel theory with Eqn. (5.42). The dynamical behaviour of the ion cloud can be calculated at long times by a diffusion equation. Neglecting the effects of ballistic motion, the diffusive movement is then given by

$$\xi_0 \frac{\partial}{\partial t}\rho_\pm(\vec{r}, t) = \vec{\nabla}(k_B T \vec{\nabla}\rho_\pm(\vec{r}, t) \mp \rho_\pm(\vec{r}, t)\vec{E}(\vec{r}, t)) \tag{5.45}$$

with the ionic friction coefficient ξ_0, the actual charge ion density $\rho_\pm$ corresponding to their valency, the electric field $\vec{E}$, which is the sum of the field created by the moving

polyelectrolyte and the electric field created by the ionic charge density, which obeys the Poisson equation (Eqn. (4.5)) to finally interact with the polyelectrolyte. The solution of the diffusion equation (Eqn. (5.45)) is given by

$$\rho_{\pm}(\vec{r},t) = \rho_{\pm}^{eq}(\vec{r}-\vec{v}t) + \delta\rho_{\pm}(\vec{r}-\vec{v}t) \tag{5.46}$$

in its stationary form. Linearising with respect to the velocity $\vec{v}$, respectively $Z_M e$ and insertion of the solution of Eqn. (4.6) for $\vec{E}$ by applying Eqn. (5.45), yields the following equation for the perturbed ion density

$$(\delta\rho_+(r) - \delta\rho_-(r)) = \frac{1}{(2\pi)^3}\int d\vec{k}\left(\frac{\xi_0 Z e^2 \kappa_D^2}{k_B T}\right)\frac{i\vec{k}\vec{v}}{(k^2+\kappa_D^2)^2}e^{-i\vec{k}\vec{r}} \tag{5.47}$$

which can be inserted into the general equation of the electric field

$$\vec{E}(\vec{r}) = -\mathbf{T}(\vec{r}-\vec{R})\vec{v} \tag{5.48}$$

where the components $T_{\alpha\beta}$ of the tensor $\mathbf{T}(\vec{R})$ are given by

$$T_{\alpha\beta}(\vec{R}) = \frac{1}{(2\pi)^3}\int d^3k\,\frac{k_\alpha k_\beta}{k^2}\left(\frac{\xi_0 Z e \kappa_D^2}{k_B T(k^2+\kappa_D^2)^2}\right)e^{-i\vec{k}\vec{R}} \tag{5.49}$$

which effectively computes the electric field in terms of the velocities. In contrast to the electrophoretic effect, an explicit time dependent motion is assumed in this approach.
Another attempt to describe polyelectrolyte motion with screening effects under several conditions is presented in [119]. A main assumption in the theory of Muthukumar [119] and in nearly all other theories, is the instantaneous movement of the solvent in comparison to the movement of the polyelectrolyte. Explicit time-dependent effects of hydrodynamic screening can therefore be only investigated by considering the dynamical behaviour of the polyelectrolyte instead of the solvent, like it has been shown in [118].
Nevertheless, general conditions in terms of the effective-medium theory are assumed *e. g.* for dense polyelectrolyte solutions, where several limiting cases are presented in [119] for polyelectrolytes in special situations. The cases of varying salt concentrations and dilute, respectively semi-dilute polyelectrolyte solutions are additionally combined to a general theory.
Muthukumar consideres the following fact, which, in various publications is claimed to be correct [119]. The mobility of a polyelectrolyte is given by

$$\mu = \frac{D_{cm}}{k_B T} \tag{5.50}$$

with the general relation

$$\vec{v}_P = \mu\vec{F}. \tag{5.51}$$

for the velocity $\vec{v}_P$. Applying an external electric field $\vec{E}$, which acts on the polyelectrolyte with charges $Z_M e N$ leads to

$$\frac{k_B T}{D_{cm}}\vec{v}_P = Z_M e N \vec{E} \tag{5.52}$$

where Eqns. (5.50) and (5.51) have been combined. With the definition of the electrophoretic mobility

$$\mu_e = \frac{\vec{v}}{\vec{E}}, \tag{5.53}$$

this gives

$$\mu_e \sim ZeND_{cm} \tag{5.54}$$

where Muthukumar assumes [119], that in infinitely dilute polymer solutions the diffusion coefficient is proportional to the gyration radius $D_{cm} \sim 1/R_g$ with $R_g \sim N^{\nu}$ instead of $D_{cm} \sim N^{-1}$. Inserting these relations into Eqn. (5.54) yield

$$\mu_e \sim Ze\frac{N}{N^{\nu}} \tag{5.55}$$

where the chain only should be fully extended with $\nu = 1$ in low salt concentration due to inefficient screened repulsive electrostatic interactions.
This yields $D \sim 1/N$ in the low salt regime, which is a Rouse-like behaviour and $D \sim 1/N^{3/5} \sim 1/R_g$ in the high salt regime, which yields a Zimm-like behaviour in contrast to the experimentally observed results. Muthukumar states [119], that there are several erroneous claims in the literature which assume $D_{cm} \sim N^{-1}$ in infinitely dilute solution at all salt concentrations without any derivation, but in agreement to the experimental results.
To show that the electrophoretic mobility is indeed length independent, a sophisticated approach with the final result $\mu_e \sim N^0$ is presented. Using the Poisson equation (Eqn. (4.6)) in combination with the Debye-Hückel theory for the ions (Eqn. (5.42)) and together with preaveraging condition [7] of the Oseen tensor, the following function can be defined

$$A(r) = \frac{1}{6\pi\eta_s\vec{r}}(e^{-\kappa_D r} - 1) \tag{5.56}$$

with

$$A_{00} = \frac{1}{N}\sum_{i=0}^{N-1}\sum_{j=0}^{N-1} < A(\vec{R}_{ij}) > \tag{5.57}$$

where $\vec{R}_{ij}$ denotes the distance between the i-th and the j-th monomer. Explicit calculation gives

$$A_{00}(r) = \frac{1}{6\pi\eta_s R_g}(\mathcal{M}(\kappa_D R_g) - \mathcal{M}(0)) \tag{5.58}$$

with the function

$$\mathcal{M}(\kappa_D R_g) = \frac{R_g}{N^2}\sum_{i=0}^{N-1}\sum_{j=0}^{N-1}\left\langle\frac{e^{-\kappa_D R_{ij}}}{R_{ij}}\right\rangle \tag{5.59}$$

which can be expressed in terms of the static structure factor

$$\mathcal{M}(\kappa_D R_g) = \frac{2R_g}{\pi N}\int_0^{\infty} dk\ \frac{k^2}{k^2+\kappa_D^2}\ S(kR_g). \tag{5.60}$$

The electrophoretic mobility can finally be expressed by the above function to

$$\mu_e = \frac{ZeN}{6\pi\eta_s R_g}\mathcal{M}(\kappa_D R_g) \tag{5.61}$$

where $\mathcal{M}(\kappa_D R_g)$ can be rigorously calculated in terms of the excluded-volume parameter ν, depending on the salt concentration to

$$\mathcal{M}(\kappa_D R_g) = \frac{2}{\pi}\left(\frac{3}{2\nu}\right)^{1/2}\int_0^\infty dt\ \frac{t^2}{\left(t^2+\frac{2\nu}{3}\kappa_D^2 R_g^2\right)}\frac{1}{(1+t^2)^{1/2\nu}} \tag{5.62}$$

where the limiting cases $\kappa_D = 0$ and $\kappa_D R_g \gg 1$ can be computed.
It has been shown [119], that $\mathcal{M}(\kappa_D R_g)$ changes with increasing salt concentration from a constant to a value $(\kappa_D R_g)^{1/\nu-1}$. This gives for the electrophoretic mobility by insertion into Eqn. (5.61)

$$\mu_e \sim \frac{N^0}{\eta_s \kappa_D^\alpha} \tag{5.63}$$

a length independent behaviour depending on the electrostatic screening constant κ_D with $\alpha \to 0$ for low salt concentrations and $\alpha \to 2/3$ for high salt concentrations. Despite the contradictionary results for the diffusion coefficient, the electrophoretic mobility remains independent of the polyelectrolyte size.
Based on the same derivation as the electrophoretic effect [4], the specific solutions rely on the time independent Stokes equation. Thus, explicit time dependent behaviour of polyelectrolyte dynamics can only be considered by taking all force contributions into account and investigating the specific chain dynamics instead of the solvent. An explicit time dependent crossover effect of electrohydrodynamic screening due to charge-charge correlations, like it will be shown in the numerical results of this chapter, has not been reported in the literature before.

5.4 Simulation details

The polyelectrolyte is modeled by a simple bead-spring model. Every second bead is charged with $Ze = -1$ and the monomers interact by a FENE-potential

$$U_{FENE} = \frac{1}{2}kr_0^2 \ln\left(1-\left(\frac{r^2}{r_0^2}\right)\right) \tag{5.64}$$

with its neighbour monomers. The values for the spring constant are $k = 25k_BT/\sigma^2$ and for the equilibrium distance $r_0 = 1.5\sigma$. A hard core potential

$$U_{ij}^{hc} = \begin{cases} 4\epsilon\left[\left(\frac{\sigma_{hc}}{r}\right)^{12}-\left(\frac{\sigma_{hc}}{r}\right)^{6}\right] & r < \sigma_{hc} \\ 0 & r \geq \sigma_{hc} \end{cases} \tag{5.65}$$

mimics the excluded-volume effect with standard parameters $\epsilon = 1k_BT$, $\sigma_{hc} = 1.0\sigma$ and the mass m is set to unity. Applying the potential of Eqn. (5.65) to all charged particles

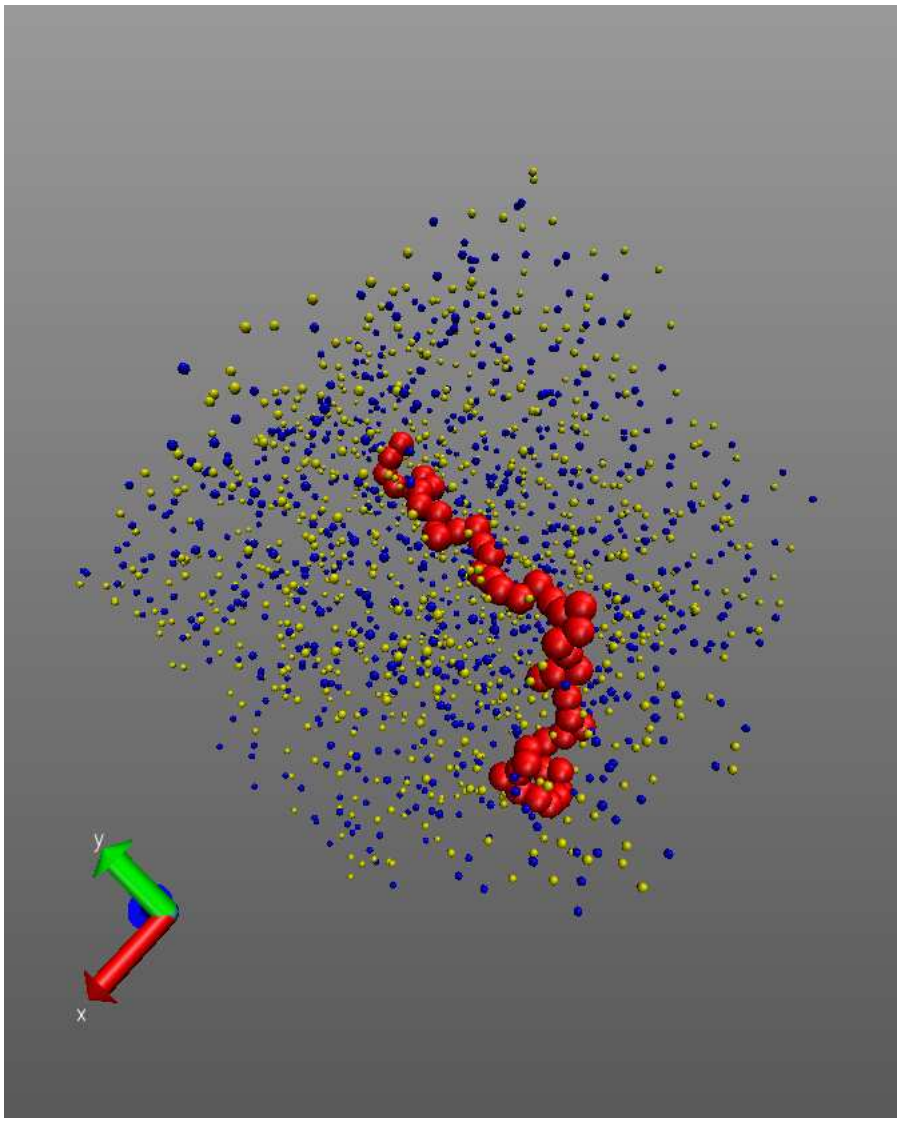

Figure 5.5: Snapshot of a negatively half charged polyelectrolyte ($N = 50$) in salty solution with anions (yellow) and cations (blue) of salt concentration $\rho_s = 0.05\sigma^{-3}$. The solvent particles have been neglected.

prevents a collapse. System charge neutrality is guaranteed. Salt ions are modeled by monovalent charges $Ze = \pm 1$. Electrostatics are calculated by the P3M-Algorithm [33]. The Bjerrum length λ_B is 1σ. The system is periodic in all directions and the box size is $l = 25\sigma$, which is around five times larger as the radius of gyration to keep finite-size effects small.
The solvent density is $\rho = 3.0\sigma^{-3}$ with a friction coefficient $\gamma_{DPD} = 5.0\sigma^{-1}(m\epsilon)^{1/2}$. The

shear viscosity was determined to $\eta_s = (1.2471 \pm 0.0082)\sigma^{-2}(m\epsilon)^{1/2}$. The cut-off radius of the DPD interactions is $r_c = 1.0\sigma$. In all simulations the timestep was chosen to $\delta t = 0.01\tau$ with a short hand notation $\tau = \sigma(m/\epsilon)^{1/2}$. The salt concentration in nearly all simulations was $\rho_s = 0.05\sigma^{-3}$, if not otherwise mentioned.
No external electric fields are applied in all presented results.

5.5 Mapping the simulation parameters to experimental conditions

In this section the simulation parameters are matched to experimental conditions. The natural unit in the simulations is the Bjerrum length which defines the strength of the electrostatic interactions in comparison to the thermal energy. For water at room temperature with $T = 300$K and dielectric constant $\epsilon_r = 80$, the Bjerrum length is given by $\lambda_B \approx 0.7$ nm [1].
For the calculation of the solvent conditions, the number density of water at room temperature has to be mapped to the simulation parameters. Taking this into account, the number of charges can be compared to the number of apparent fluid particles to calculate the salt concentration.
The mass density of water at $T = 300$ K is $\rho_m = 997.7735$ kg/m^3 [120]. The molar mass of water is $M_M = 18.015$ g/mol [83]. With the mass density $\rho_m = m/V$ and the relation $n = m/M_M$, the following equation can be derived

$$\frac{n}{V} = \frac{\rho_m}{M_M} \tag{5.66}$$

by insertion. With the above given parameters, this yields $n/V = c = 55385.7$ mol/m^3 as the molar concentration.
The Bjerrum length is given in the simulations by $\lambda_B = 1\sigma$ in a periodic box of $V = 25^3\sigma^3$. Equating $1\sigma = 0.7$ nm per definition, this gives for the periodic box a real volume of $V = 25^3\sigma^3 = (25 \cdot 0.7\text{nm})^3 = 5.359 \cdot 10^{-24}$ m^3. Solving for the molarity n of present solvent particles in that volume yields $n = c \cdot V = 55385.7$ mol/m$^3 \cdot 5.359 \cdot 10^{-24}$ m^3 $= 2.968 \cdot 10^{-19}$ mol.
Together with the Avogadro number $N_B = 6.022 \cdot 10^{23}$ mol^{-1} [83], the actual number of present solvent particles is

$$N_f = n \cdot N_B = 2.968 \cdot 10^{-19} \text{ mol} \cdot 6.022 \cdot 10^{23} \text{ mol}^{-1} = 178753 \tag{5.67}$$

in the mapped realistic volume. The number of DPD particles in that simulation volume with number density $\rho_{DPD} = 3.0\sigma^{-3}$ is $N_{DPD} = \rho_{DPD} \cdot V = 3.0\sigma^{-3} \cdot 25^3\sigma^3 = 46875$. Thus, the ratio is $N_f/N_{DPD} \approx 4$, which means that one DPD particle roughly represents 4 solvent particles.
The salt concentration of a monovalent salt like sodium chloride Na^+Cl^- in the simulation varies from $\rho_s = 0.02 - 0.075\sigma^{-3}$. Calculating the actual number of salt particles in the simulation volume yields $624 - 2342$ ions which means that the ions are dissociated by $N_C = 312 - 1171$ salt molecules in the simulation volume. With the relation $c =$

Value	Simulation	Experiment
Volume	$(25\sigma)^3$	$5.359 \cdot 10^{-24}\mathrm{m}^3$
Salt concentration	$(0.02 - 0.075)\sigma^{-3}$	$(0.0966 - 0.362)$ mol/l
Bjerrum length	1σ	0.7 nm
Gyration radius ($N = 50$)	5.35σ	3.75 nm

Table 5.1: Summary of simulation parameters in comparison to mapped experimental conditions.

$n/V = N_C/(N_B \cdot V)$ the molarity is given by $c = N_C/(6.022 \cdot 10^{23}\ \mathrm{mol}^{-1} \cdot 5.359 \cdot 10^{-24}\ \mathrm{m}^3)$ to $c = 96.67\ \mathrm{mol/m}^3$ respectively $c = 362.83\ \mathrm{mol/m}^3$.
Although these values seem to be very high, the calculation for the concentration in mol/l shows that these are moderate experimental values with $c = 0.0966$ mol/l, respectively $c = 0.362$ mol/l. Comparison of the values show that the simulation parameters reflect experimental conditions, which are often used in buffer solutions around 0.1 mol/l molar NaCl concentration [121, 122]. Thus, the numerical results can be tested by experiments.
Due to electroneutrality of the system, the counterions of the charged monomers have also to be taken into account. For a half charged chain with $N = 50$ monomers this yields $N_+ = 25$ additional positive charges which define the pH value of the solution. The molar charge concentration of the counterions is $c = N_+/(6.022 \cdot 10^{23}\ \mathrm{mol}^{-1} \cdot 5.359 \cdot 10^{-24}\mathrm{m}^3) = 0.007746$ mol/l. With the definition of the pH-value [83] for a strong electrolyte, this gives

$$pH = -\log_{10}(c(N_+)) = 4.86 \tag{5.68}$$

if the self autoprotolysis of water is neglected. Thus the solution is slightly acidic in contrast to experimental conditions where often higher pH-Values are taken into account [121, 122]. Table 5.1 displays all relevant values together with the determined radius of gyration for a half charged chain with $N = 50$ monomers.

5.6 Numerical results

5.6.1 Mean-square displacement of the center-of-mass

The mean-square displacement (Eqn. (5.17)) of the center-of-mass of polymer chains is shown in Fig. 5.6. The monomer number is $N = 50$ for all chains and the solvent parameters are identical. The uncharged chain with the same solvent conditions serves as a reference.
It is obvious that the polyelectrolyte chains at all salt concentrations have a lower diffusion coefficient than the uncharged polymers. This fact is explanable due to the relaxation effect mentioned in section 5.3 [3, 4].
A polyelectrolyte is surrounded by its ion cloud which is electrostatically bound to the chain. A migrating polyelectrolyte has to drag this ion cloud along although the move-

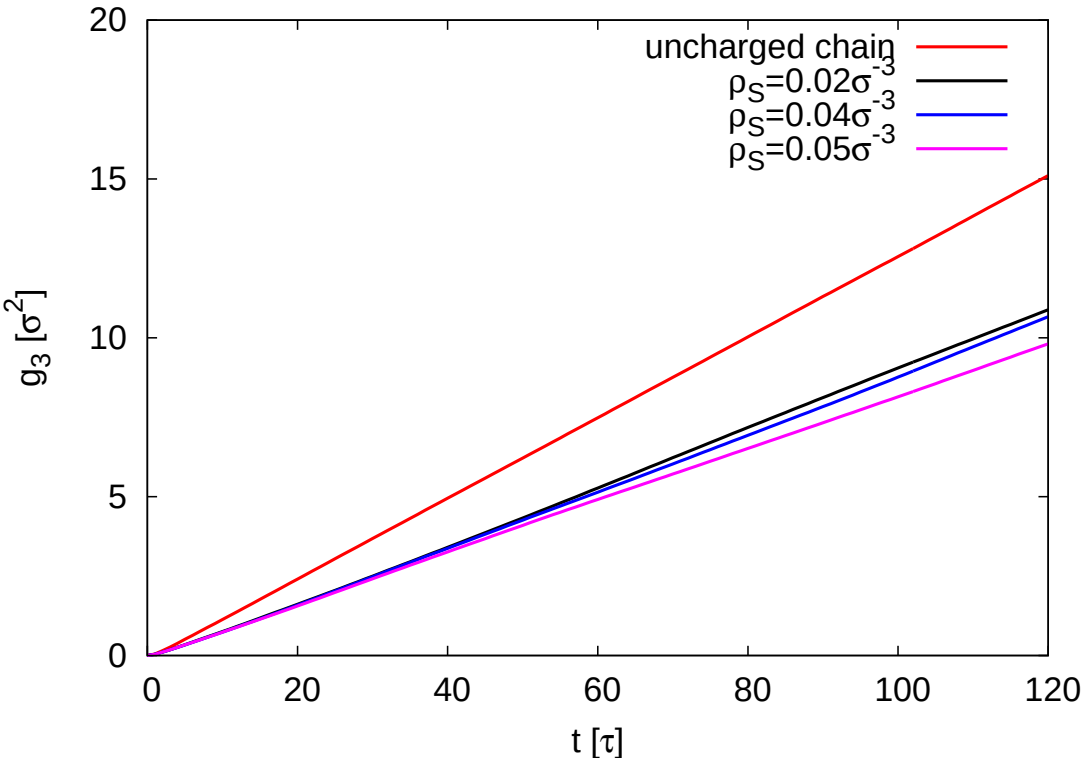

Figure 5.6: Mean-square-displacement of polyelectrolytes for various salt concentrations and $N = 50$ monomers. An uncharged chain with the same monomer number and the same solvent conditions is shown as a reference.

ment of the ions is delayed. Electrostatic forces build up which lead to a electrostatic friction force that decelerates the motion of the chain. This shows that the overall motion of polyelectrolytes is mainly influenced by electrostatic interactions which dominate the diffusive behaviour of the chains massively.

5.6.2 Mean-square displacement of monomers in the center-of-mass system

In addition to the overall motion of the chain, it can also be shown that the single monomer motion in the center-of-mass system (Eqn. (5.16)) is dominated as well by electrostatic interactions. The diffusion coefficients for the uncharged chain are given by $D^u_{cm} = 0.0211 \pm 0.0001\sigma(m/\epsilon)^{-1/2}$ and for the polyelectrolyte with salt concentration $\rho_s = 0.05\sigma^{-3}$ by $D^c_{cm} = 0.0137 \pm 0.0001\sigma(m/\epsilon)^{-1/2}$.
Fig. 5.7 presents the results for a polyelectrolyte with salt concentration $\rho = 0.05\sigma^{-3}$ together with the reference system of an uncharged chain, scaled both with their center-of-mass diffusion coefficients.
The nearly identical results corresponding to $D_{cm}t$ between 0.1 and $1\sigma^2$ show, that the

single monomer motion follows the overall diffusive motion of the chain in agreement. Thus the relative displacement of a single monomer is as well as the overall motion

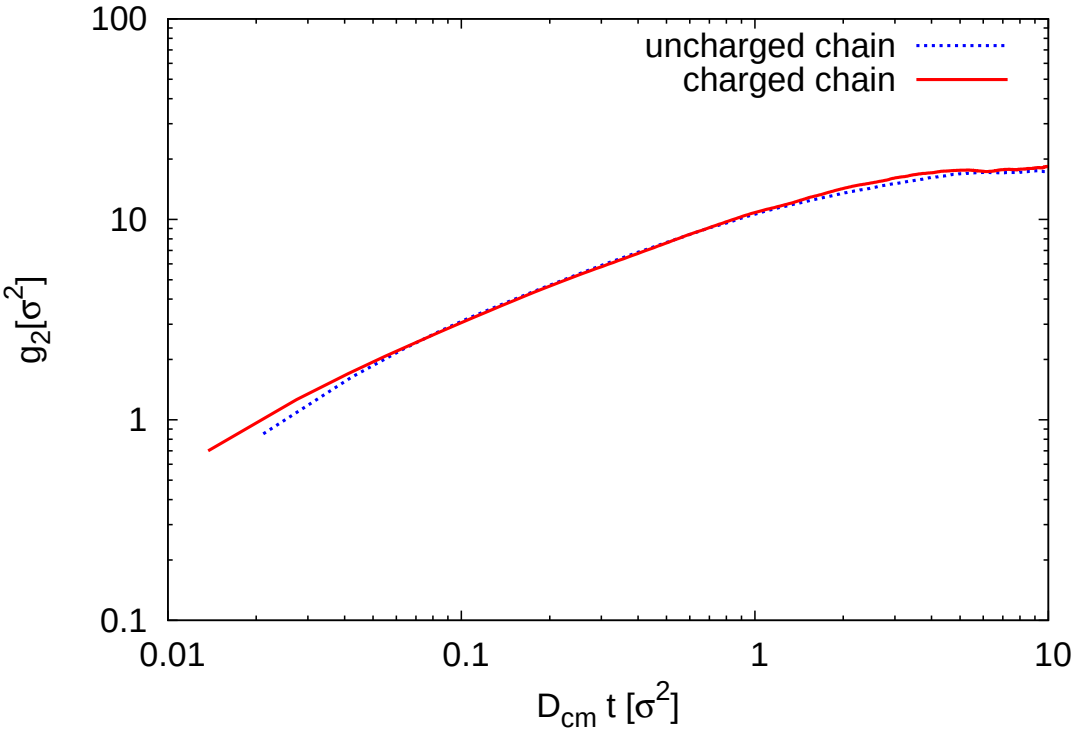

Figure 5.7: Mean-square-displacement of a monomer in the center-of-mass system of a polyelectrolyte with salt concentration $\rho_s = 0.05\sigma^{-3}$ (blue line). An uncharged chain with the same monomer number and the same solvent conditions is shown as a reference (red line).

influenced by the underlying center of mass diffusion coefficient which is dominated by the relaxation effect (*cf.* Fig. 5.6). It turns out, that electrostatic interactions therefore dominate the dynamics even on the monomer scale.

5.6.3 Radius of gyration

To determine the excluded-volume parameter ν, simulations have been performed with varying monomer number for an uncharged chain and a half charged polyelectrolyte with salt concentration $\rho_s = 0.05\sigma^{-3}$. The values for the uncharged chain are shown on the left side of Fig. 5.8.
By a fit of the form

$$F(N) = \gamma \cdot N^{\nu} \tag{5.69}$$

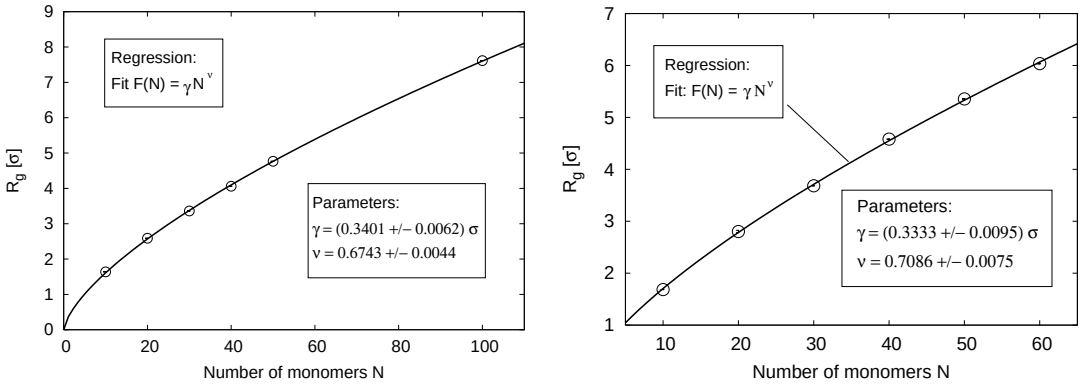

Figure 5.8: **Left:** Radius of gyration R_g for an uncharged chain with varying monomer number. **Right:** Radius of gyration R_g for a half charged chain with varying monomer number and salt concentration $\rho_s = 0.05\sigma^{-3}$.

which is equivalent to the universal scaling relation [7]

$$R_g \sim N^{\nu} \tag{5.70}$$

the following excluded-volume parameter was determined

$$\nu = 0.6743 \pm 0.0044 \tag{5.71}$$

which is higher than the theoretical prediction for uncharged infinite chains of $\nu = 0.588$ [123]. This is explanable due to the finite length ($N = 50$) of the polymer chain in agreement to the results reported in the literature [26].
The values for the charged chain are shown on the right side of Fig. 5.8. The scaling relation of Eqn. (5.70) gives

$$\nu = 0.7086 \pm 0.0075 \tag{5.72}$$

which differs only minimally to the excluded-volume parameter of the uncharged chain. Electrostatic interactions for half charged chains are therefore in contrast to fully charged chains [125, 126] not that dominant in the presence of salt. This is obvious due to the slight increase of ν. For the investigation of the dynamic properties, the half charged chains are therefore more suited to distinguish between different dynamical regimes as it has been mentioned in section 5.1.2.

5.6.4 Static structure factor

As it was mentioned in section 5.1.1, it is possible to determine the excluded-volume parameter of the chains together with the scaling relation of Eqn. (5.9) by the static structure factor.
Fig. 5.9 presents the static structure factor for an uncharged, respectively a half charged chain with a salt concentration of $\rho_s = 0.05\sigma^{-3}$. Due to the inner-chain electrostatic

interactions, the half charged chain is slightly swollen ($\nu = 0.7$) in contrast to the uncharged chain ($\nu = 0.67$), which is in a good correspondence to the results derived in section 5.6.3. The relatively large excluded-volume parameter of the uncharged polymer

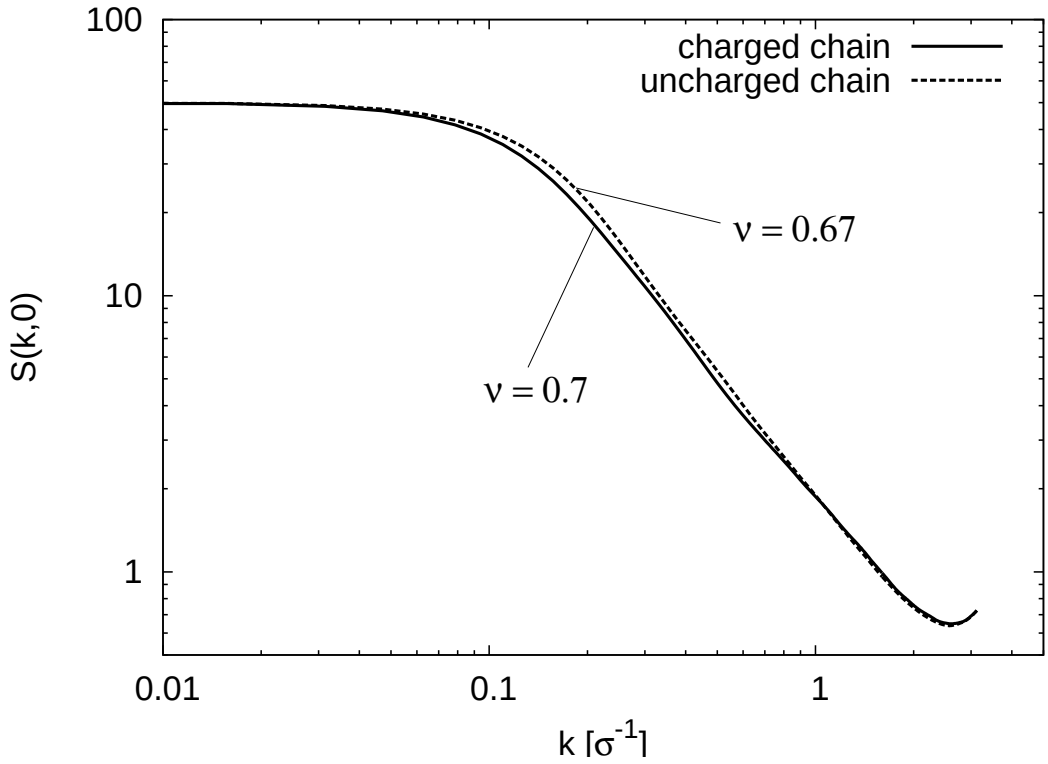

Figure 5.9: Static structure factor S(k,0) for an uncharged chain with $N = 50$ monomers in correspondence to a half charged chain with the same monomer number and salt concentration $\rho_s = 0.05\sigma^{-3}$.

is due to the finite size of the chain. Thus both chains do not differ crucially from each other.

5.6.5 Mean-square displacement of a single monomer

The results for the single monomer diffusion are shown in Fig. 5.10 and Fig. 5.11. The movement of the end monomers is dominated by diffusive motion as an analysis has shown ($\sim t$). Thus only the movement of the central monomer is taken into investigation to avoid end effects reported in [26].
Fig. 5.10 presents the results for an uncharged chain with 50 monomers. As standard theories indicate, the dynamical behaviour is given by Zimm-Dynamics with $g_1 \sim t^{2/3}$ (Eqn. (5.13) with $z = 3$) which is shown by the red line.
The results for a half charged chain with 50 monomers with a salt concentration of

$\rho_s = 0.05\sigma^{-3}$ are shown in Fig. 5.11. For times $t < 60\sigma\sqrt{m/\epsilon}$, the dynamic behaviour is described by Zimm-Dynamics. At later times $60 \leq t/\tau \leq 100$ a slight crossover to Rouse-Dynamics is observed, as the results of the inset indicate. This is indicated by the red line in the inset which corresponds to Eqn. (5.13) and the dynamic exponent $z = 3.5$ (Eqn. (5.15)). The results for $t < 60\tau$ are therefore in coincidence with

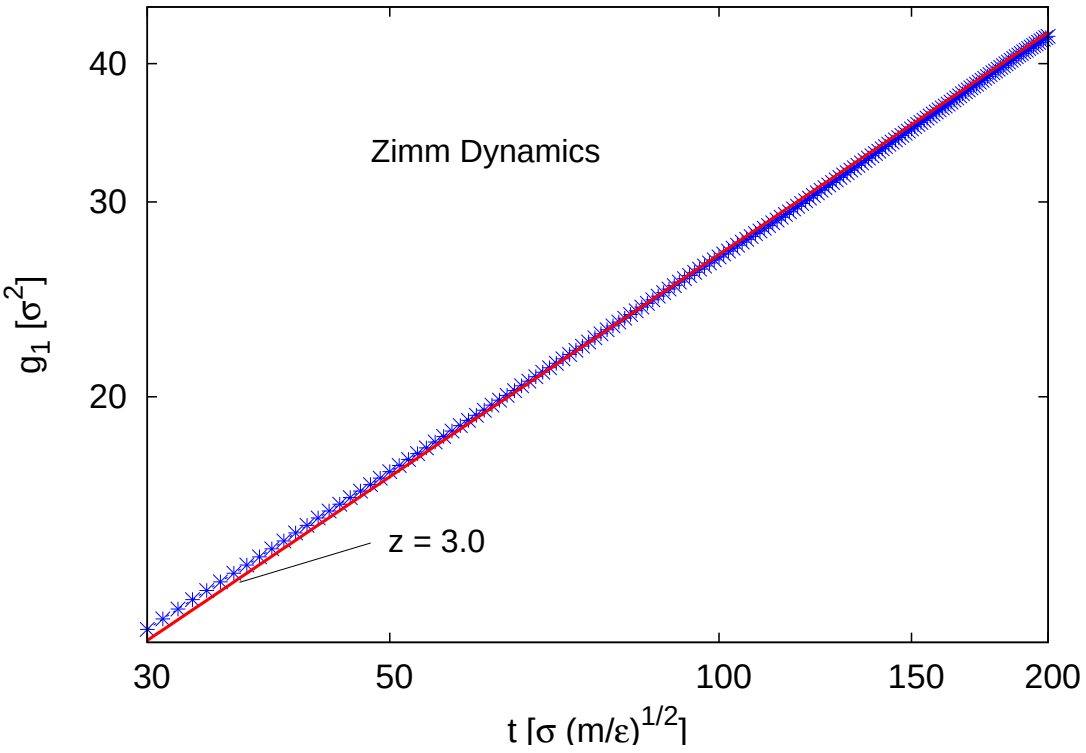

Figure 5.10: Mean-square-displacement of the central monomer for an uncharged chain with 50 monomers. The red line corresponds to $t^{2/z}$ with $z = 3.0$ for the exponent of Zimm-Dynamics.

the previous results of the uncharged chain with an unexpected, but short crossover to Rouse-Dynamics for $t > 60\sigma\sqrt{m/\epsilon}$.

5.6.6 Rouse-Mode analysis

The decay of the Rouse-Modes (Eqn. (5.20)) is plotted for a half charged polyelectrolyte with salt concentration $\rho_s = 0.05\sigma^{-3}$ for the modes $p = 3 - 10$ in Fig. 5.12.
On the left side, the decay is scaled with a Zimm-scaling $p^{3\nu}r(p)$ by Eqn. (5.21) with the finite-size correction function $r(p)$, which was first published in [26]. The Zimm-scaling does not well apply, whereas on the right side of Fig. 5.12, the same function is scaled with $p^{2\nu+1}/f(p)$ in agreement to Eqn. (5.22). The function $f(p)$ contains the finite-size

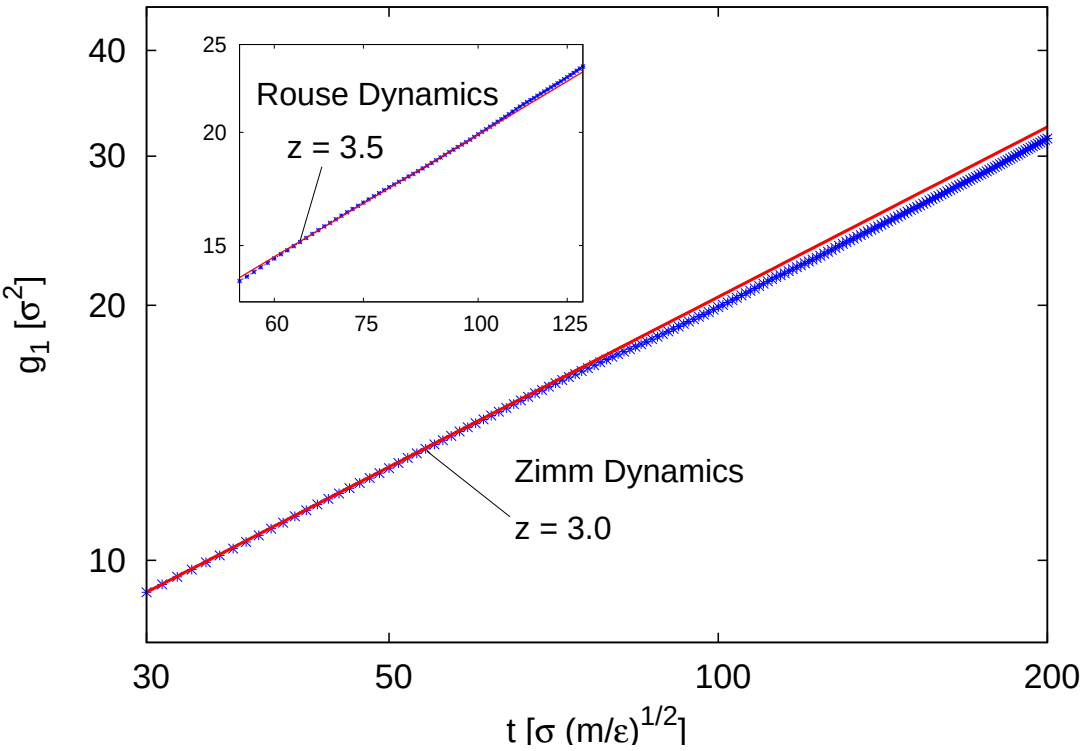

Figure 5.11: Mean-square-displacement of the central monomer for a half charged chain ($N = 50$) with salt concentration $\rho_s = 0.05\sigma^{-3}$. The red line in the main picture corresponds to $t^{2/z}$ with $z = 3.0$ for Zimm-Dynamics whereas the red line in the inset is proportional to $z = 3.5$. The inset shows a blowup for times $50 \leq t/\tau \leq 130$ with $\tau = \sigma\sqrt{m/\epsilon}$.

correction of screened hydrodynamic interactions. It is obvious that the Rouse-scaling produces a better collapse of data points. Thus, it can be concluded that hydrodynamic interactions are absent in the internal modes of the chain after a characteristic time and for a characteristic length scale in contrast to standard theories.
The opposite can be seen for an uncharged chain in Fig. 5.13. The same arguments as above are applied but the Zimm-scaling produces, as predicted, a better data collapse with an effective excluded-volume parameter of $\nu = 0.72$. This shows, that the overall behaviour of charged and uncharged polymers differ in their dynamic properties.

5.6.7 Dynamic structure factor

In Fig. 5.14 the dynamic structure factor for a half charged chain with salt concentration $\rho_s = 0.05\sigma^{-3}$ is shown for times $0 < t/\tau < 300$ and for the uncharged chain with $0 < t/\tau < 180$ on inverse length scales $0.2 < k\sigma < 0.3$. These upper times correspond to

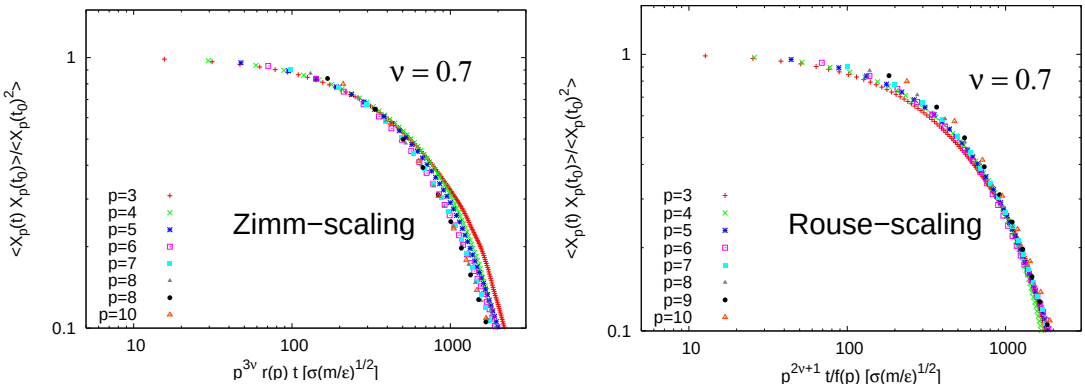

Figure 5.12: Left side: Autocorrelation function (Eqn.(5.20)) of the Rouse-modes $p = 3-10$ plotted by Zimm-scaling ($p^{3\nu}$ and finite-size correction function $r(p)$ [26]) for a half charged polyelectrolyte with salt concentration $\rho_s = 0.05\sigma^{-3}$ and $\nu = 0.7$. Right side: Autocorrelation function plotted by Rouse-scaling ($p^{2\nu+1}$ and finite-size correction function $f(p)$ for screened hydrodynamic interactions [26]).

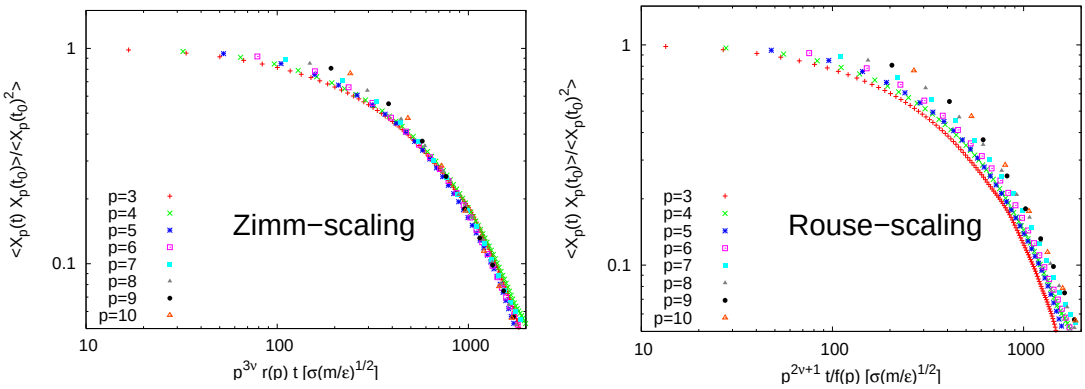

Figure 5.13: Left side: Autocorrelation function (Eqn.(5.20)) of the Rouse-modes $p = 3-10$ plotted by Zimm-scaling ($p^{3\nu}$ and finite-size correction function $r(p)$ [26]) for an uncharged chain in a DPD solvent with $\nu_{eff} = 0.72$. The same Rouse-modes plotted with Rouse-scaling ($p^{2\nu+1}$ and finite-size correction function $f(p)$ for screened hydrodynamic interactions are presented on the right side [26]).

the longest relaxation times and are roughly given by Eqn. (5.18) and the corresponding inserted values. The scaling relation (Eqn.(5.24)) is both applied for Zimm- ($z = 3$) as well as for Rouse-scaling ($z = 2 + 1/\nu \approx 3.5$). On the left side of Fig. 5.14, Zimm-scaling

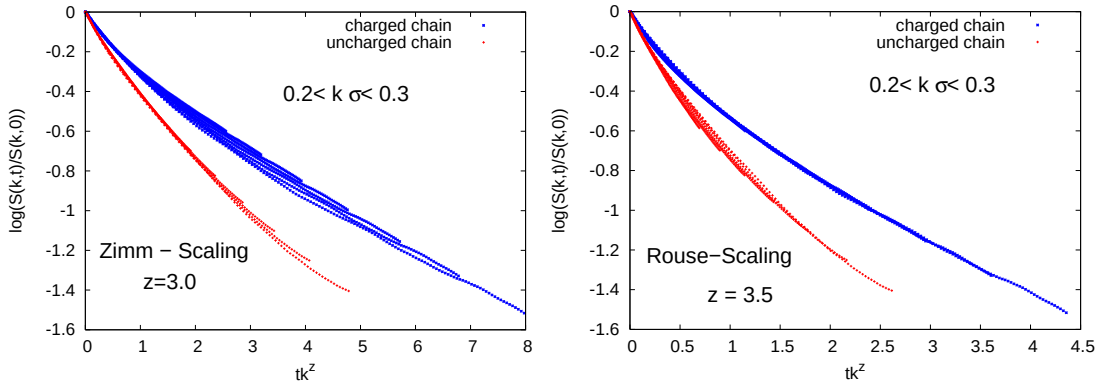

Figure 5.14: Dynamic structure factor S(k,t) for an uncharged chain (red) in correspondence to a half charged chain (blue) for $0.2 < k\sigma < 0.3$ and salt concentration $\rho_s = 0.05\sigma^{-3}$. The timescale for the uncharged chain is $0 < t/\tau < 180$ in contrast to $0 < t/\tau < 300$ for the half charged polyelectrolyte. Both chains consist of $N = 50$ monomers. Left side: Zimm-scaling with $z = 3$. Right side: Rouse-scaling with $z = 3.5$.

is applied which shows that the uncharged chain can be well described by a chain with hydrodynamic interactions due to its collapse of data points (red points). In contrast, the polyelectrolyte does not show this scaling collapse of data points (blue points).
In the opposite case, which is shown on the right side of Fig. 5.14, a Rouse-scaling with $z = 3.5$ is applied for both chains. The red points of the uncharged chain do not show a scaling at all whereas the polyelectrolyte shows a well pronounced collapse of data points.
Thus, the dynamic behaviour on inverse length scales $0.2 < k\sigma < 0.3$ seem to obey Rouse-scaling for polyelectrolytes which means an absence of hydrodynamic interactions in contrast to standard theories. The uncharged polymer instead is dominated by hydrodynamic interactions which is reflected by Zimm-Dynamics.
Focussing on polyelectrolyte dynamics at time scales below $t < 55\tau$ on the left side of Fig. 5.15, scaling can be observed by a collapse of data points for $z = 3$, obeying Zimm-Dynamics. Thus hydrodynamic interactions are present for the polyelectrolyte at short times on nearly all length scales due to the observed scaling behaviour on inverse length scales $0.2 < k\sigma < 0.5$.
In contrast to the results shown in Fig. 5.14, Zimm-Dynamics is therefore applicable for times $t_0 \sim 55\tau$ whereas Rouse-Dynamics dominate at later times. This means a full presence of hydrodynamic interactions on short time scales. After a characteristic time, the polyelectrolyte dynamics is better described by Rouse-Dynamics in absence of hydrodynamic interactions (*cf.* Fig. 5.14) on a specific length scale.
In addition to the characteristic time t_0, it is also possible to define a characteristic inverse length scale.

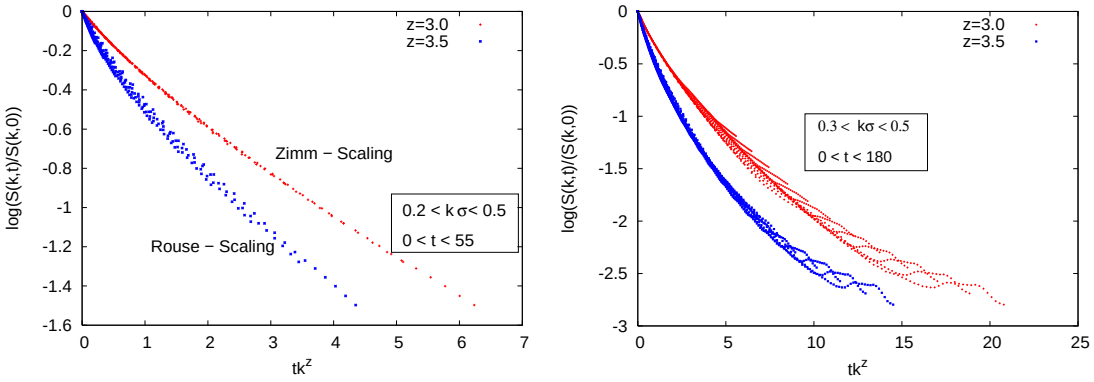

Figure 5.15: Left side: Dynamic structure factor S(k,t) of a half charged chain (N=50) with salt concentration $\rho_s = 0.05\sigma^{-3}$ for inverse wavelengths $0.2 < k\sigma < 0.5$ and time scales below $t < 55\tau$. Right side: Dynamic structure factor S(k,t) of a half charged chain (N=50) with salt concentration $\rho_s = 0.05\sigma^{-3}$ on inverse wavelengths $0.3 < k\sigma < 0.5$ and time scales $0 < t/\tau < 180$.

As the right side of Fig. 5.15 shows, the scaling relations for inverse wave lengths $0.3 < k\sigma < 0.5$ at times $0 < t/\tau < 180$ produces no pronounced data collapse for both regimes. Thus, the polyelectrolyte is neither described by Zimm- nor by Rouse-Dynamics on these length scales. Therefore the largest characteristic inverse wave length is $k_0 \approx 0.3\sigma$, on which the dynamical crossover is observable.
To summarize, the dynamical behaviour of uncharged polymers is dominated by hydrodynamic interactions. In contrast to that, polyelectrolytes with salt concentration $\rho_s = 0.05\sigma^{-3}$ show a more complicated, transient dynamical behaviour. As the results indicate, the presence of hydrodynamic interactions is given for short times. After a characteristic time on a certain length scale, hydrodynamic interactions do not influence the dynamical behaviour of the chain at all and Rouse-regime takes over.

5.6.8 Numerical results for various salt concentrations

The dynamic structure factor for half charged polyelectrolytes with $N = 50$ monomers has been further determined for various additional salt concentrations $\rho_s = 0.02, 0.04$ and $0.075\sigma^{-3}$.
As it has been reported in the last section, a characteristic screening length and time scale was observed for the salt concentration $\rho_s = 0.05\sigma^{-3}$. An inspection of the same characteristics within varying conditions offers the possiblity to investigate the influence of the salt concentration on this crossover. First, the influence of the salt concentration on the static structure factor is studied and presented in Fig. 5.16.
The static structure factor differs for low and for high salt concentration in the scaling regime $0.1 \leq k\sigma \leq 1.0$ due to the influence and strength of the inner chain electrostatic interactions. For low salt densities ($\rho_s = 0.02\sigma^{-3}$), the Debye-Hückel screening

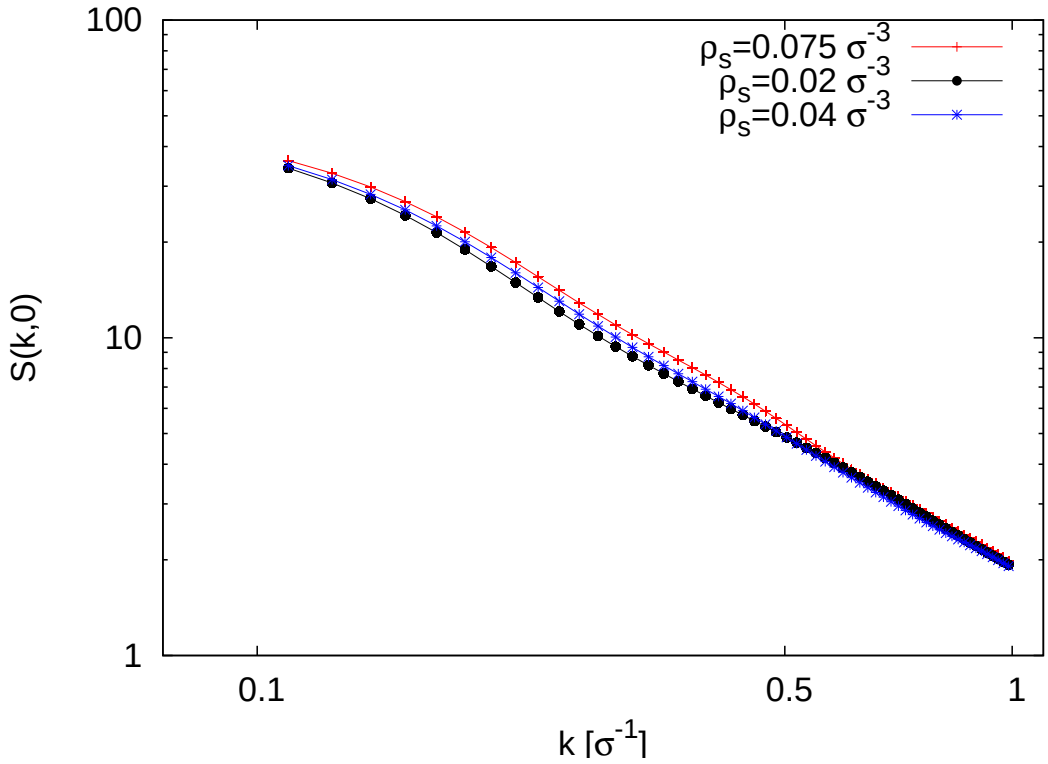

Figure 5.16: Static structure factor of a half charged chain with $N = 50$ monomers for various salt concentrations.

length κ_D^{-1} (Eqn. (4.26)) is larger. The repulsive electrostatic interactions between the monomers are therefore not so crucially screened and the chain is more swollen.
The influence of the salt concentration on static properties like the radius of gyration and the end to end radius is presented in Fig. 5.17. It is obvious, that lower salt concentrations lead to a swelling of the chain due to smaller Debye-Hückel screening lengths which results in slightly larger excluded-volume parameters ν (Table 5.2). This can be explained as before due to an uneffective screening of electrostatic interactions by larger Debye-Hückel screening lengths. The dynamic properties concerning the dynamic structure factor are investigated in more detail in the following.
Fig. 5.18 presents the dynamic structure factors for various salt concentrations within an inverse wave length $0.23 < k\sigma < 0.35$ and for a time $t < 120\tau$. It is pointed out that the screening effect becomes more pronounced for higher salt concentrations. For the salt concentration $\rho_s = 0.02\sigma^{-3}$ only very slight perturbations to Zimm-Dynamics can be observed. With increasing salt concentration, the perturbation grows crucially as it is obvious for a salt concentration $\rho_s = 0.075\sigma^{-3}$.
Furthermore, as it has been shown in Table 5.2, the corresponding excluded-volume parameters increases for lower salt concentrations, such that a distinction between the

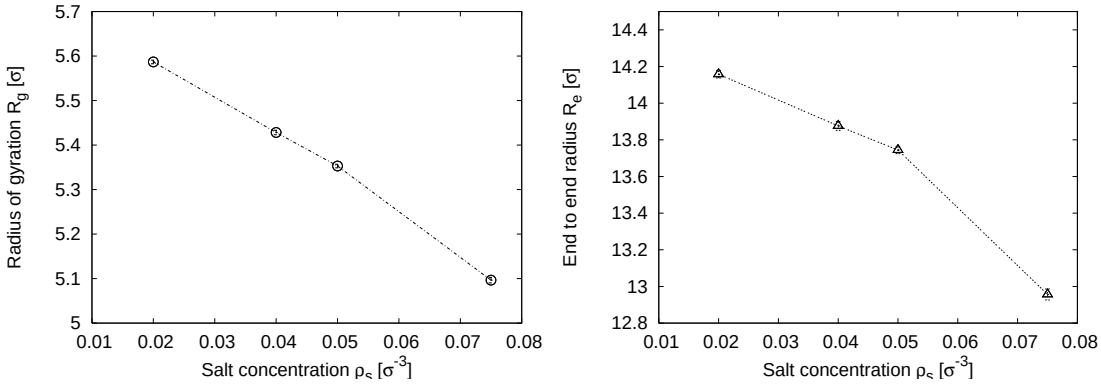

Figure 5.17: Radius of gyration R_g (left) and end to end radius R_e (right) for polyelectrolytes with $N = 50$ monomers for various salt concentrations.

$\rho_s[\sigma^{-3}]$	ν	$\kappa_D^{-1}[\sigma]$
0.02	0.80	1.38
0.04	0.73	0.99
0.05	0.70	0.89
0.075	0.67	0.72

Table 5.2: Excluded-volume parameter ν for half charged polyelectrolytes with 50 monomers and corresponding Debye-Hückel screening lengths κ_D^{-1} (Eqn. (4.26)) for different salt concentrations.

different regimes due to the different exponents z is not that obvious any more.

Salt concentration $\rho_s = 0.02\sigma^{-3}$

The dynamic structure factor for the salt concentration $\rho_s = 0.02\sigma^{-3}$ in the regime $0.2 < k\sigma < 0.3$ and for times $0 < t/\tau < 70$ (red lines) and $70 < t/\tau < 120$ (blue lines) is presented in Fig. 5.19.
As it was shown in Fig. 5.18, the crossover to Rouse-Dynamics for this low salt concentration is not that pronounced as in the opposite case for high salt concentrations. Therefore Zimm-Dynamics apply on this length scale up to a time $t = 70\tau$ until a short crossover sets in as both sides of Fig. 5.19 show.
The overall behaviour is thus more influenced by hydrodynamic interactions which is reflected by the Zimm regime.
Fig. 5.20 presents the chain dynamics for inverse length scales $0.2 < k\sigma < 0.5$ and times $t < 70\tau$ (left side) and $70 < t/\tau < 120$ (right side).
The situation is quite complex. Zimm-Dynamics is given for short times whereas Rouse-Dynamics describe the overall behaviour on all length scales at $t \approx 80\tau$ slightly better

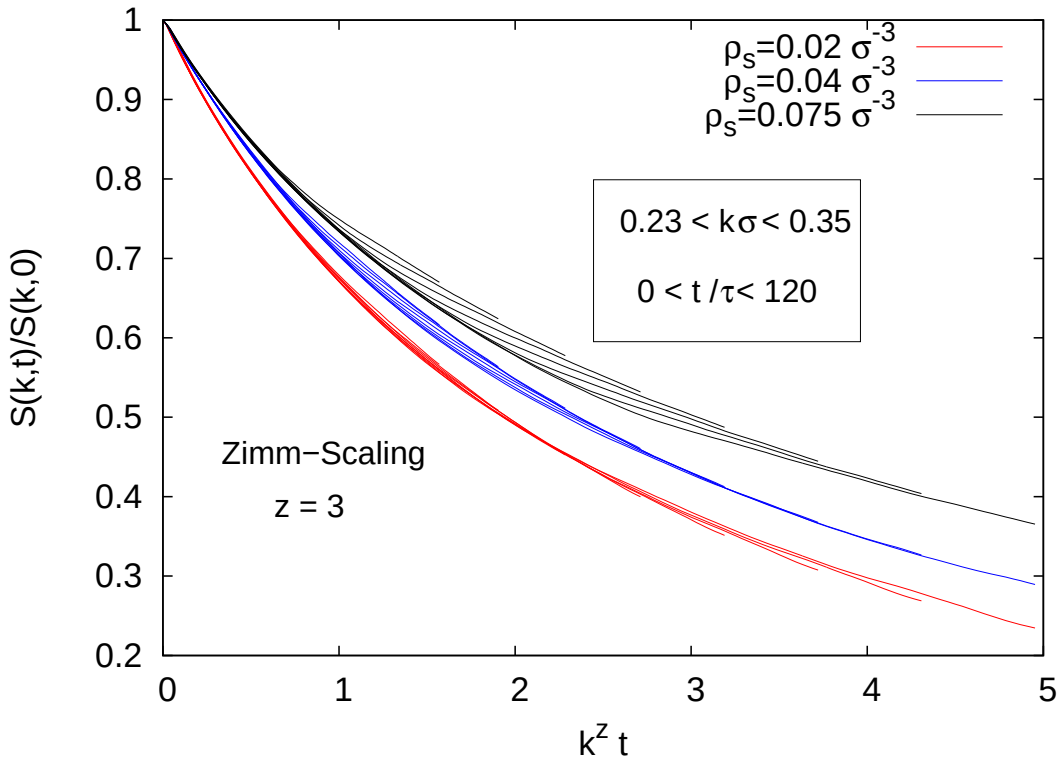

Figure 5.18: Dynamic structure factor for various salt concentrations and inverse wave lengths $0.23 < k\sigma < 0.35$ and times $t < 120\tau$ for half charged polyelectrolytes with $N = 50$ monomers. Zimm-scaling ($z = 3.0$) is applied to investigate the dynamical behvaviour.

but both approaches fail at times $t \gg 80\tau$. Thus, the same behaviour as in the former case for the salt concentration $\rho_s = 0.05\sigma^{-3}$ is observed. Nevertheless, the large excluded volume parameter $\nu \approx 0.8$ prevents a detailed investigation of the dynamic properties for this salt concentration, as it has been mentioned in section 5.1.2.

Salt concentration $\rho_s = 0.04\sigma^{-3}$

Nearly the same characteristic behaviour as for the former case is observed for the salt concentration $\rho_s = 0.04\sigma^{-3}$ on the inverse length scale $0.2 < k\sigma < 0.3$. As Fig. 5.21 indicates, a slight crossover to Rouse-Dynamics is observed at a time $t \approx 60\tau$. For times $t \ll 60\tau$ instead, Zimm-Dynamics is indicated.
The same is true for Fig. 5.22, where the dynamical behaviour for times $0 < t/\tau < 120$ on inverse length scales $0.2 < k\sigma < 0.5$ is presented. For times $0 < t/\tau < 60$, nearly Zimm-Dynamics with slight perturbations can be observed on all length scales. For times close to $t \approx 60\tau$, Rouse-Dynamics applies better to the dynamical behaviour but for later

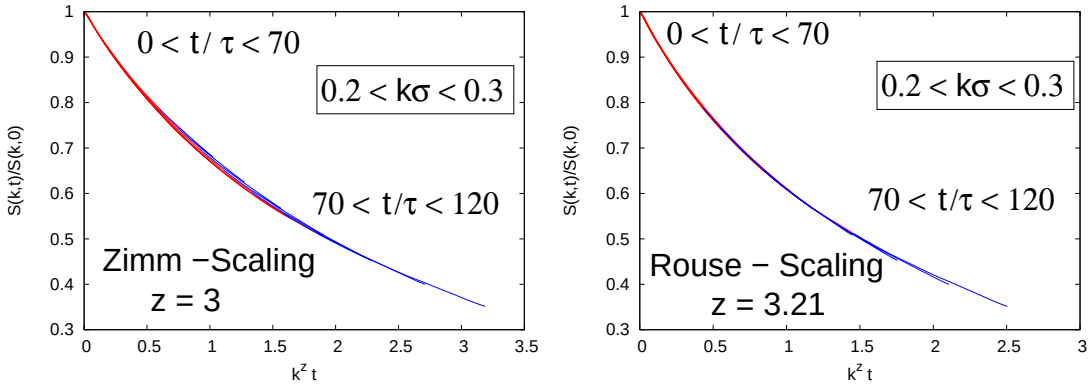

Figure 5.19: Left side: Dynamic structure factor S(k,t) of a half charged chain with 50 monomers for inverse wavelengths $0.2 < k\sigma < 0.3$ and time scales below $t < 120\tau$ for Zimm-scaling with salt concentration $\rho_s = 0.02\sigma^{-3}$, where the red and the blue lines indicate different times. Right side: Dynamic structure factor S(k,t) of a half charged chain with 50 monomers for inverse wavelengths $0.2 < k\sigma < 0.3$ and time scales between $70 < t/\tau < 120$ for Rouse-scaling with salt concentration $\rho_s = 0.02\sigma^{-3}$, where the red and the blue lines indicate different times.

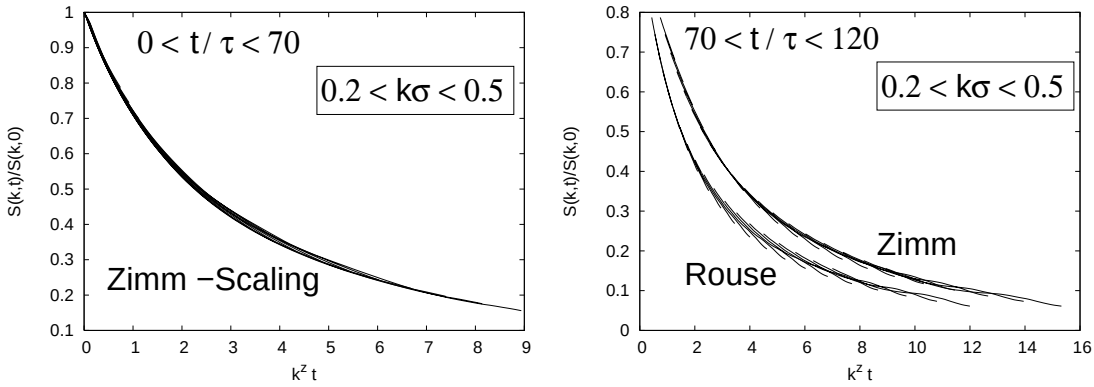

Figure 5.20: Left side: Dynamic structure factor S(k,t) of a half charged chain with 50 monomers for inverse wavelengths $0.2 < k\sigma < 0.5$ and time scales below $t < 70\tau$ with salt concentration $\rho_s = 0.02\sigma^{-3}$ scaled by $z = 3$. Right side: Dynamic structure factor S(k,t) of a half charged chain with 50 monomers for inverse wavelengths $0.2 < k\sigma < 0.5$ and time scales between $70 < t < 120\tau$ in both scaling regimes ($z = 3$ and $z = 3.21$) for a salt concentration $\rho_s = 0.02\sigma^{-3}$.

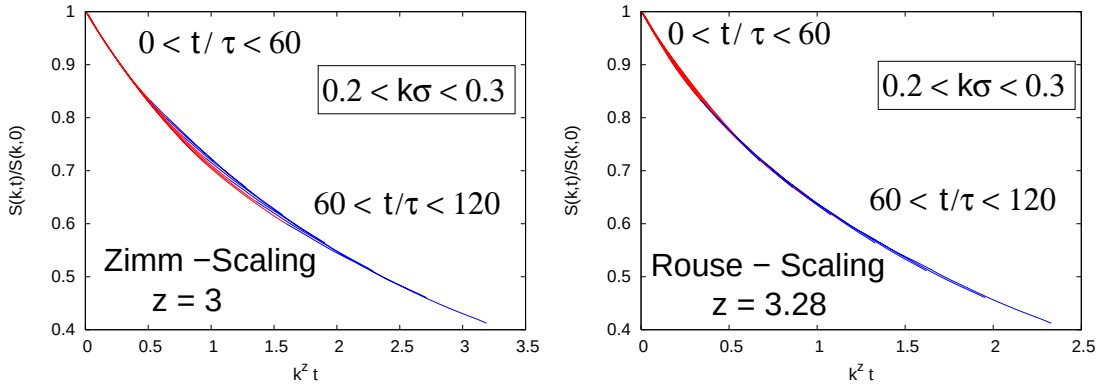

Figure 5.21: Left side: Dynamic structure factor S(k,t) of a half charged chain with 50 monomers for inverse wavelengths $0.2 < k\sigma < 0.3$ and time scales below $t < 120\tau$ with salt concentration $\rho_s = 0.04\sigma^{-3}$ scaled by Zimm-Dynamics, where the red and the blue lines indicate different times. Right side: Dynamic structure factor S(k,t) of a half charged chain for inverse wavelengths $0.2 < k\sigma < 0.3$ and time scales between $0 < t < 120\tau$ for Rouse-scaling with salt concentration $\rho_s = 0.04\sigma^{-3}$, where the red and the blue lines indicate different times.

times neither Zimm- nor Rouse-scaling can be observed. An intermediate behaviour between both dynamical regimes is therefore indicated, as it has been reported earlier in this section.

Salt concentration $\rho_s = 0.075\sigma^{-3}$

Investigating the results for a salt concentration of $\rho_s = 0.075\sigma^{-3}$ as in Fig. 5.23, indicates a pronounced screening of hydrodynamic interactions on length scales $0.2 < k\sigma < 0.3$ at times $t \approx 40\tau$. For times $t \leq 40$, Zimm-scaling is applicable in contrast to $t \gg 40\tau$ where Rouse-scaling is more favourable.
On inverse length scales $0.2 \leq k\sigma \leq 0.5$ (Fig. 5.24), Zimm scaling produces the best results for times $t < 40\tau$, which shows that hydrodynamic interactions are present on all length scales for short times in agreement to earlier derived results.
For times $t \geq 40\tau$, Rouse-Dynamics scale on a certain length scale ($0.2 < k\sigma < 0.3$) but again for $k\sigma > 0.3$ and $t \gg 40\tau$ the dynamical behaviour cannot be fully described by one of the theories. Non-scalable results are derived, which indicate an intermediate behaviour.
Summarising the results, the time inset of Rouse-Dynamics varies for different salt concentrations. Nevertheless, the transient behaviour of polyelectrolytes in contrast to uncharged chains on certain time and length scales is evident at all salt concentrations. With increasing salt concentration, the chain gets more flexible due to an effective screening of electrostatic interactions. This has been observed in Figs. 5.16, 5.17 and Table

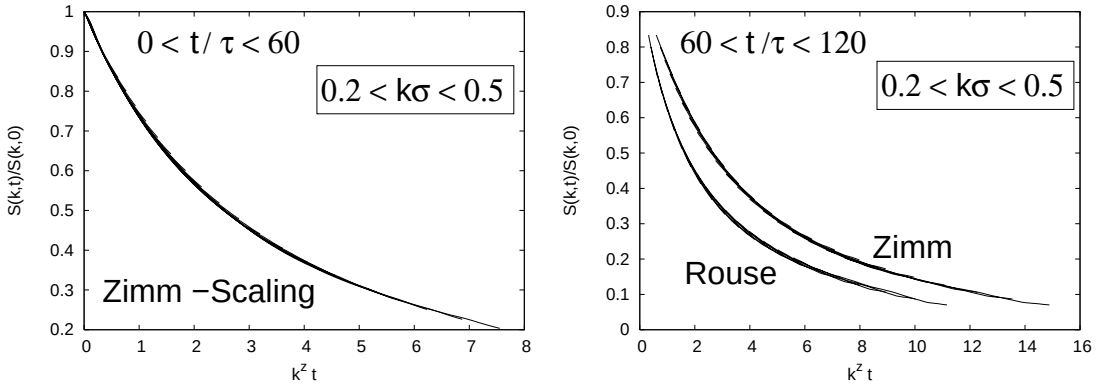

Figure 5.22: Left side: Dynamic structure factor S(k,t) of a half charged chain with 50 monomers for inverse wavelengths $0.2 < k\sigma < 0.5$ and time scales below $t < 60\tau$ for Zimm-scaling with salt concentration $\rho_s = 0.04\sigma^{-3}$. Right side: Dynamic structure factor S(k,t) of a half charged chain with 50 monomers for inverse wavelengths $0.2 < k\sigma < 0.5$ and time scales between $60 < t/\tau < 120\tau$ for Rouse- and Zimm-scaling ($z = 3.0$ and $z = 3.28$) with a salt concentration of $\rho_s = 0.04\sigma^{-3}$.

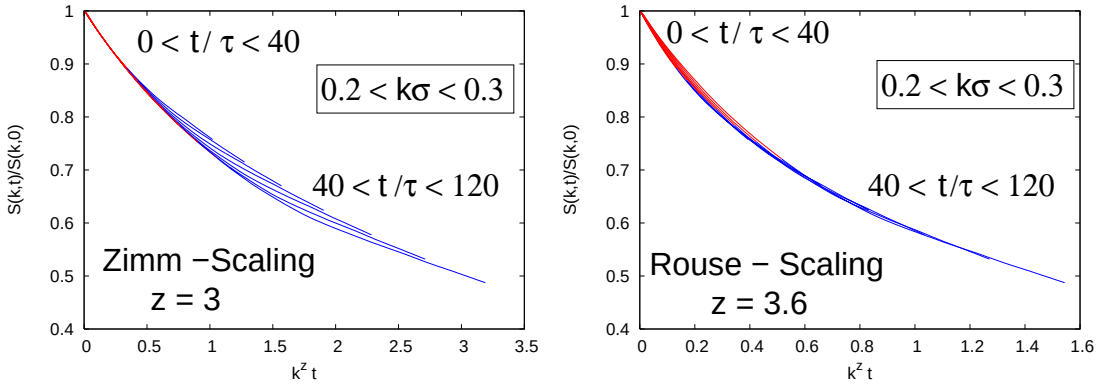

Figure 5.23: Left side: Dynamic structure factor S(k,t) of a half charged chain with 50 monomers for inverse wavelengths $0.2 < k\sigma < 0.3$ and time scales below $t < 120\tau$ for Zimm-scaling with salt concentration $\rho_s = 0.075\sigma^{-3}$ where the red and the blue lines indicate different times. Right side: Dynamic structure factor S(k,t) of a half charged chain with 50 monomers for inverse wavelengths $0.2 < k\sigma < 0.3$ and time scales between $0 < t/\tau < 120$ for Rouse-scaling with salt concentration $\rho_s = 0.075\sigma^{-3}$, where the red and the blue lines indicate different times.

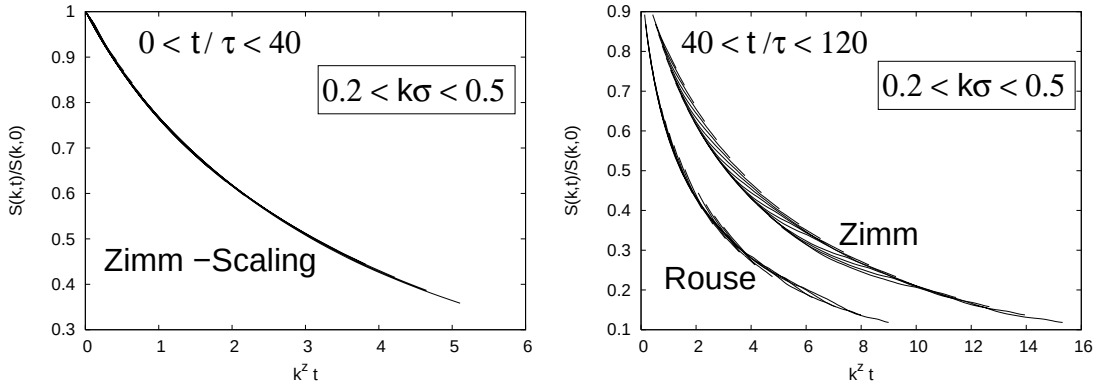

Figure 5.24: Left side: Dynamic structure factor S(k,t) of a half charged chain on inverse wavelengths $0.2 < k\sigma < 0.5$ and time scales below $t < 40\tau$ for Zimm-scaling with salt density $\rho_s = 0.075\sigma^{-3}$. Right side: Dynamic structure factor S(k,t) of a half charged chain for inverse wavelengths $0.2 < k\sigma < 0.5$ and time scales between $40 < t/\tau < 120$ for Rouse-scaling and Zimm-scaling ($z = 3.0$ and $z = 3.6$) with salt concentration $\rho_s = 0.075\sigma^{-3}$.

5.2, where more swollen chains are derived at lower salt concentrations corresponding to larger Debye-Hückel lengths κ_D^{-1}. It can be concluded, that the distinction between the dynamical regimes for these concentrations is not that well pronounced due to a larger excluded-volume parameter.
The various results for the appearance of the screening time may result on different relaxation times, which scale after Eqn. (5.22) and Eqn. (5.21) to $\tau_{R/Z} \sim p^{\nu}$. Thus, the flexibility and the full chain relaxation strongly depends on the salt concentration and the corresponding excluded-volume parameter. To summarise, the crossover into Rouse-Dynamics is a fact whose strength depends on the salt concentration. As Table 5.1 has shown, a salt concentration of $\rho_s = 0.02\sigma^{-3}$ corresponds to a molar salt concentration of $\rho_s = 0.0966$ mol/l which is moderate in experimental buffer solutions.
Experiments have been undertaken to investigate the dynamical behaviour of DNA in a 0.1 molar salty buffer solution [121, 122]. The authors of [122] have studied the kinetic behaviour by fluorescence correlation spectroscopy and found a Rouse like behaviour for double stranded DNA. In addition, Petrov *et al.* [121] have repeated identical experiments but with a different technique to produce the samples of DNA fragments. In contrast to [122], the results have shown a clear Zimm like behaviour. Petrov *et al.* [121] conjecture, that the method of producing double stranded DNA samples proposed in [122], could yield a considerable amount of unlabeled non-fluorescent DNA molecules which has not been taken into consideration. This could result in a semidilute solution characterised by Rouse-Dynamics [7, 118], as explained in section 5.3.
Nevertheless, the low salt concentration may be an additional important criterion as the numerical results of this work indicate. Neither Rouse- nor Zimm-Dynamics are fully

applicable for a salt concentration of $\rho_s = 0.02\sigma^{-3}$, which roughly corresponds to the salty solution used in [122, 121], as Table 5.1 indicates. Only slight perturbations to Zimm-scaling have been observed for this salt concentrations in the numerical results, which are not that obvious as the corresponding results for high salt concentrations.
Increasing the salt concentration may therefore help to clarify the experimental results and to fully indicate the dynamical behaviour of polyelectrolyte chains in aqueous buffer solutions.

5.7 Theoretical modelling of the screening effect

Summarising the previous results, it is obvious that polyelectrolyte dynamics in salty solution are mainly dominated by electrostatic interactions. This is true for the diffusion coefficient (section 5.6.1) which is massively lowered in contrast to uncharged chains. Not only the overall chain motion, but also the inner-monomer motion is influenced by the relaxation effect [4] (section 5.6.2). In addition, analysing the inner-monomer motion shows slight deviations to Zimm-Dynamics (section 5.6.5). After a characteristic time, the single monomer dynamics can be described by Rouse-Dynamics which means an absence of hydrodynamic interactions. The same is true for the Rouse-Mode analysis (section 5.6.6) as well as for the scaling results of the dynamic structure factor (section 5.6.7 and 5.6.8). Thus, a crossover from Zimm- to Rouse-Dynamics on a characteristic inverse length scale and for a characteristic time can be observed in nearly all analytical methods in contrast to standard theories.
The crossover therefore appears due to the influence of the electrostatic interactions as the results for the uncharged chains have shown. In contrast to electrophoresis, the present electric fields are created by the charged particles themselves. The absence of any external electric forces leads to extremely inhomogeneously distributed electric fields which are created by the polyelectrolyte and its surrounding ion cloud. A straightforward calculation scheme as in electrophoresis [3, 4, 113] is therefore not applicable. The timescale has explicitly to be considered for this dynamic effect as the numerical results have shown. Therefore, the motion of the charged particles has to be investigated first. It turns out, that a description in terms of the Debye-Hückel theory is valid. Based on this fact, a tentative explanation of the crossover will be presented in the next sections.

5.7.1 Dynamics of the ion cloud

The motion of the surrounding ion cloud can be calculated and investigated by studying the behaviour of the dynamic charge structure factor

$$S_q(k,t) = \langle |I_q(\vec{k},t) I_q(-\vec{k},0)| \rangle \tag{5.73}$$

with

$$I_q = \sum_i Z_i e \; e^{i\vec{k}\cdot\vec{r}_i} \tag{5.74}$$

where the sum runs over all charged particles in the simulation box and $Z_i e$ denotes their charge. The mobility of the ions can be calculated by the mean-square displacement of

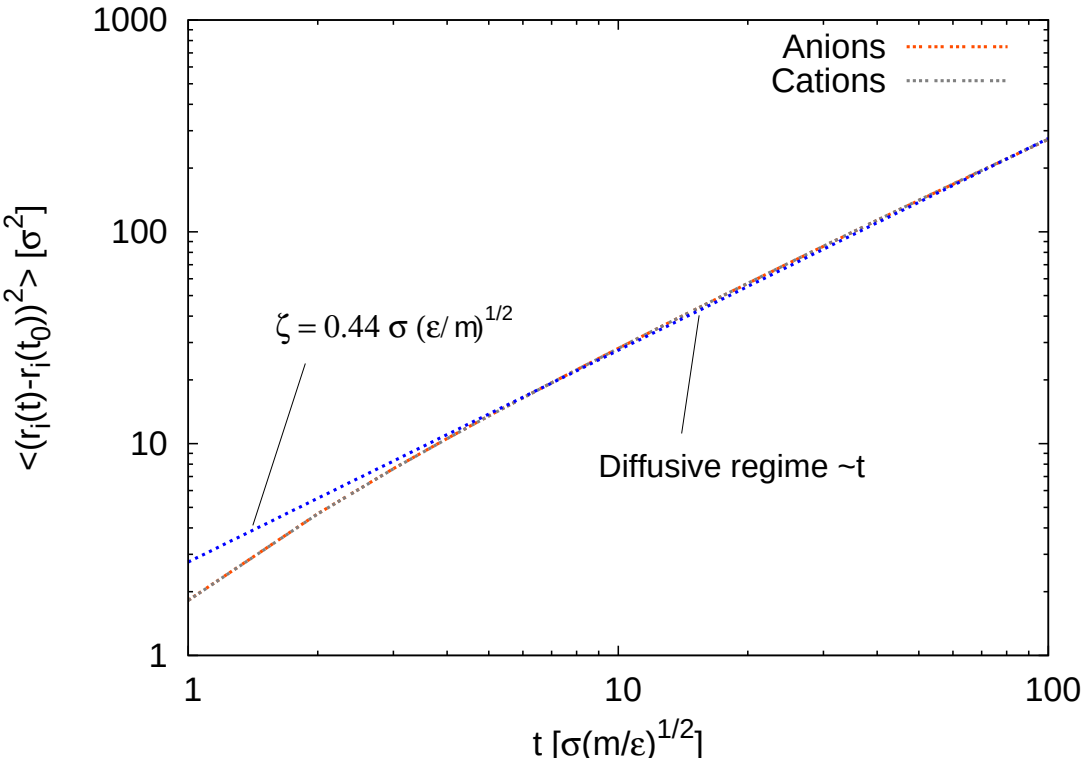

Figure 5.25: Mean-square displacement of ions in free solution in absence of external fields with solvent density $\rho = 3.0\sigma^{-3}$ and friction coefficient $\gamma_{DPD} = 5.0\sigma^{-1}(m\epsilon)^{1/2}$.

a single ion which is shown in Fig. 5.25. The migration becomes diffusive ($\sim t$) after a time $t \approx 10\sigma(m/\epsilon)^{1/2}$. The corresponding mobilities are calculated by a linear fit to $\zeta_a = (0.4424 \pm 0.0003)\sigma(m/\epsilon)^{-1/2}$ for the anions and $\zeta_c = (0.4427 \pm 0.0004)\sigma(m/\epsilon)^{-1/2}$ for the cations.

Fig. 5.26 presents the characteristic self relaxation of the ion motion for times $t < 10\sigma\sqrt{(m/\epsilon)}$ and $t \geq 10\sigma\sqrt{(m/\epsilon)}$ indicated by the charge structure factor $S_q(k,t)$. In agreement to the results of Fig. 5.25, ballistic motion is present for times $t < 10\sigma\sqrt{(m/\epsilon)}$ while diffusive behaviour ($\sim k^2 t$) [7] takes over at later times. Thus the dynamics of the ions can be effectively described on a longer time scale by the proposed diffusion equation of Eqn. (5.45) in agreement to [4].

Details can be found in the appendix C.1. At this point, only the final diffusion equation is presented

$$\left(\frac{\partial}{\partial t} + \frac{1}{\tau_D(\vec{k})}\right) \sum_i Z_i e \rho_i(\vec{k},t) = \frac{\rho_c^{eq}(\vec{k},t)}{\tau_D(\vec{k})}, \tag{5.75}$$

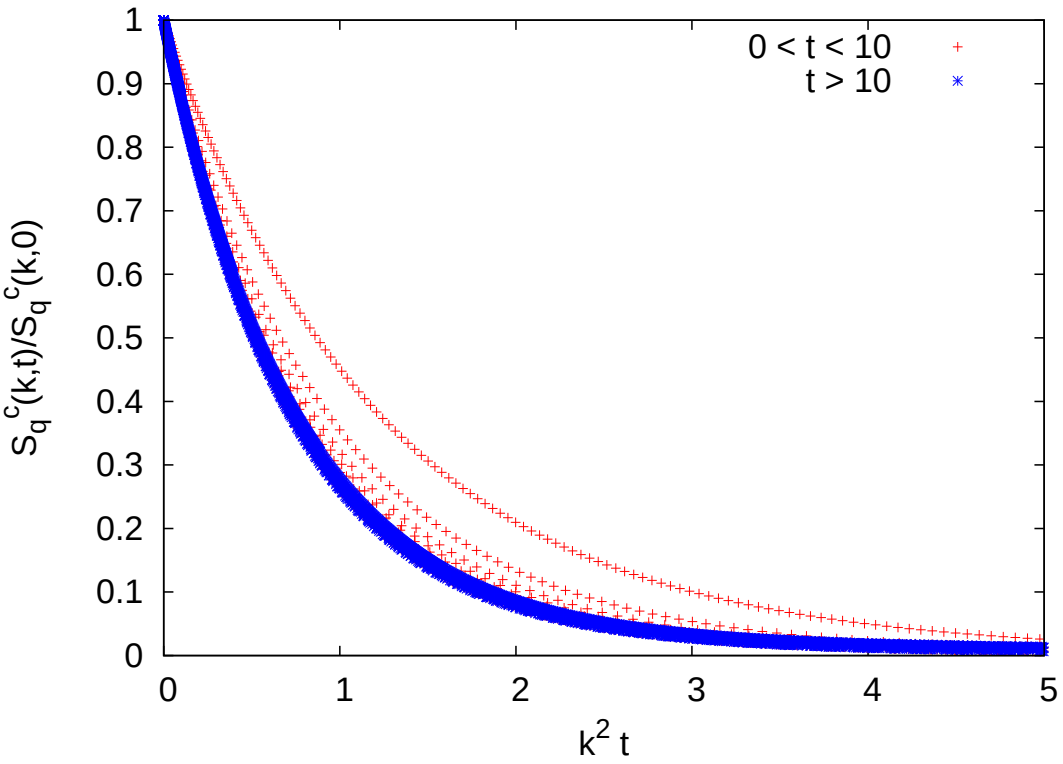

Figure 5.26: Characteristic self relaxation of the ion motion for times $t < 10\sigma(m/\epsilon)^{1/2}$ and $t \geq 10\sigma(m/\epsilon)^{1/2}$ indicated by the charge structure factor $S_q(k,t)$.

which indicates that the actual ionic charge distribution $\sum_i Z_i e \rho_i(\vec{k},t)$ relaxes against a Debye-Hückel distribution ρ_c^{eq} around the polyelectrolyte in a time

$$\tau_D(\vec{k}) = \frac{1}{\zeta k_B T(k^2 + \kappa_D^2)} \tag{5.76}$$

which strongly depends on κ_D and the ionic mobility coefficient $\zeta = \zeta_a = \zeta_c$.
Fig. 5.27 finally presents this relaxation of the ion distribution in agreement to Eqn. (5.75) for a salt concentration of $\rho_s = 0.05\sigma^{-3}$ with the inserted values of Table 5.2 in terms of Eqn. (5.75). Although the ion motion does not follow the expontial decay exactly, the distribution has clearly relaxed on times $t \geq 10\tau$ towards a Debye-Hückel distribution around the polyelectrolyte. Deviations appear in accordance to the ballistic regime, which is dominant for these small times.
Therefore as a main result, the ions follow the chain adiabatically after the above mentioned characteristic time. The theoretical modelling of the dynamical transition within the Debye-Hückel theory is therefore valid.

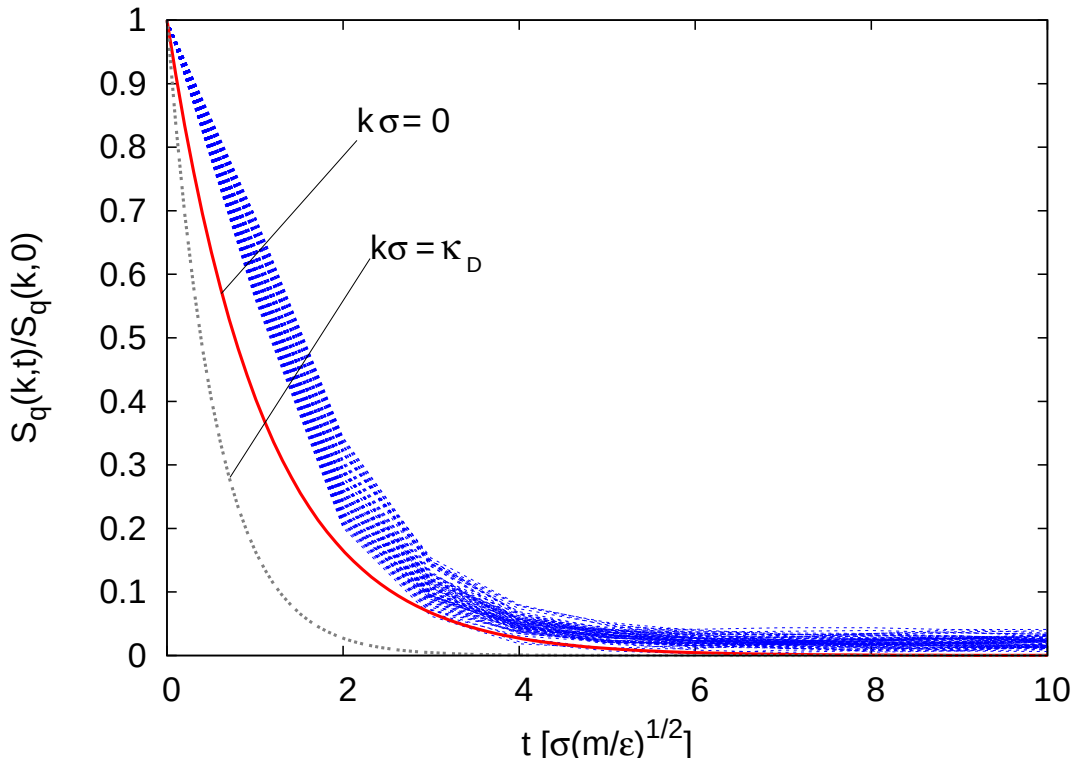

Figure 5.27: Characteristic exponential relaxation of the actual ion distribution against a Debye-Hückel distribution. The lower line shows the theoretical relaxation time for $k = \kappa_D = 1.1236\sigma^{-1}$ and the upper for $k = 0\sigma^{-1}$, calculated by the corresponding values of Eqn. (5.76).

5.7.2 Force contributions on the dynamical chain behaviour

As it was mentioned before, the polyelectrolyte is massively dominated by electrostatic interactions. Even the electrostatic relaxation effect acts on the monomers, as it has been discussed in section 5.6.2. Considering the forces that act on the chain, both electrostatic and non-electrostatic contributions have to be taken into account. Instead of external forces, only the inherent forces in the system should lead to a screening of hydrodynamic interactions.
To investigate the influence of the different force contributions on the dynamical behviour of the chain, the Fourier-transformed Stokes equation (Eqn. (5.26) with Eqn. (5.27)) has to be solved and explicitly calculated for the corresponding contributions of the forces. The detailed calculation (*cf.* appendix C.2) with the assumption that the Debye-Hückel theory is valid and consideration of a single monomer velocity $\vec{v}^{(i)}$ yields the following

expression

$$\begin{aligned}\vec{v}^{(i)}(\vec{k}) &= \frac{1}{\eta_s k^2}\sum_l (\mathbf{1}-\hat{k}\hat{k})\left[\hat{d}_{il}\left(U'(d_{il})-\frac{(Z_M e)^2}{2}\,\kappa_D^2\,I'(\kappa_D d_{il})\right)\right]\\ &+\frac{1}{\eta_s k}\sum_l (\mathbf{1}-\hat{k}\hat{k})\left[-i\hat{d}_{il}(\hat{k}\vec{d}_{il})\frac{(Z_M e)^2}{2}\,\kappa_D^2\,I'(\kappa_D d_{il})\right]\\ &+\mathcal{O}(k)\end{aligned} \tag{5.77}$$

with $\vec{d}_{ij}=\vec{R}_{i+l}-\vec{R}_i$ and $\hat{d}_{il}=\vec{d}_{il}/d_{il}$, which is splitted into its single contributions. The corresponding definitions of the parameters are given in Eqns. (C.24), (C.25) and (C.26), which are derived in appendix C.2. Ignoring the explicit parameters, the dynamical behaviour can be defined by studying the prefactors $\mathcal{O}(1/k)$. Back transformation into the coordinate space allows to identify the underlying dynamics.
Thus, it can be shown that the first line of Eqn. (5.77) with $\sim 1/\eta_s k^2$ is proportional to

$$\vec{v}^{(i)}(\vec{r}) \sim \frac{1}{r} \tag{5.78}$$

whereas the second line with $\sim 1/\eta_s k$ is poportional to

$$\vec{v}^{(i)}(\vec{r}) \sim \frac{1}{r^2} \tag{5.79}$$

while the other contributions lead to

$$\vec{v}^{(i)}(\vec{r}) \sim \frac{1}{r^3} \tag{5.80}$$

and higher order.
It can be shown (*cf.* appendix C.2) that Eqn. (5.78) includes mixed force contributions of the non-electrostatic and the electrostatic interactions. Those contributions lead to a $1/r$ behaviour which is proportional to the unscreened Oseen-Tensor (Eqn. (5.28)).
This explains the fact, that uncharged polymers are dominated by Zimm-Dynamics due to solely non electric forces, which is in coincidence with the earlier derived results and standard theories.
Hydrodynamic screening is given instead, if the hydrodynamic interactions decay faster than $1/r$ [113], which is obvious for the exponentially screened Oseen tensor

$$\mathbf{H} \sim \frac{1}{r} e^{-\kappa_D r} \tag{5.81}$$

(Eqn. (5.44)) or higher order corrections like

$$\mathbf{H} \sim \frac{1}{r^n} \tag{5.82}$$

with $n \geq 2$. Investigating the contributions of the electrostatic forces acting in Eqn. (5.79) in detail, it turns out that the pure electrostatic interactions lead to a screened Oseen-Tensor which decays with $\sim 1/r^2$. Although this is only a very weak decay, the consequences can be investigated in detail as the numerical results of this chapter have shown.

Further numerical evidence for this explanation can be found in the appendix C.2, where it will be shown, that for a time averaged polyelectrolyte chain the monopole contributions (Eqn. (5.78)) decay faster in time than the dipole contributions of Eqn. (5.79). This indicates that the dipole contributions dominate over the monopole contributions after a characteristic time which roughly corresponds to the crossover time t_0. Thus, the behaviour of the polyelectrolyte is mainly influenced by screened hydrodynamic interactions after a time t_0, that decay with $1/r^2$ and higher order.
The characteristic upper transition length scale $k_0 \approx 0.3\sigma$, as shown in section 5.6.7 is roughly given for $k_0^{-1} \approx 3.4\sigma$. Above this limit, a crossover cannot be observed. Mapping this length scale to the polyelectrolyte length scale, it is obvious that 3.4σ coincides with the double average distance between two charged monomers of a half charged polyelectrolyte. The microscopic distance between two charged monomers was found to be $a_{ii} \approx 1.7\sigma$. Comparing the results for the Debye-Hückel lengths κ_D^{-1} in Table 5.2, it can be seen that for all cases $\kappa_D^{-1} < a_{ii}$ is guaranteed. This corresponds well with the fact that the Rouse-scaling breaks down for large length scales $k < k_0 \sim \kappa_D^{-1}$. Thus, the relevant length scales are directly related to the length scales defined by the electrostatic interactions within the chain.
The results of this chapter have shown that the dynamics of polyelectrolyte chains in salty solution in absence of external electric fields are more complicated than expected. Standard theories have not predicted this behaviour before, although experimental evidences have been published in [122]. A lot of standard theories assume a time independent behaviour and are therefore not applicable to explain the numerical results. Explicit time dependent behaviour has instead been observed for the crossover from Zimm- to Rouse-Dynamics. Evaluating the underlying force contributions on the chain and the time averaged contributions, yields the possibility to model a screening mechanism. The effect of the salt concentration on this crossover is evident.

6 Modelling electrophoresis: Polyelectrolytes in microchannels

Schluss mit Kontinentendrift - Pangea wieder her!
- Blixa Bargeld (1996)

As it has been mentioned in the introduction, the ultimate goal of this work focusses on the simulation of polyelectrolyte dynamics in microchannels in the presence of external electric fields. In this chapter, the boundary and electrokinetic effects of microchannels are combined with polyelectrolyte electrophoresis in salt solution. The scope of this chapter stands in contrast to recent publications [125, 126], where polyelectrolyte electrophoresis in free salt solution has been investigated.
As it was reported in [1] and shown in chapter 5, the electrophoretic mobility is length independent. Thus a pure size separation of polyelectrolytes in free solution without geometrical confinement is not possible. Recent experimental and theoretical work [127, 128] has shown a length dependent separation technique in so called micro-structured devices. Steric hindrance of the polyelectrolyte in a specially formed microstructure (*cf.* Fig. 3.1) or in entropic traps [1] allows to alter the migration dynamics to finally separate polyelectrolytes by their length. Although the fabrication of these structured microdevices has become nowadays realisable, further research focusses on polyelectrolyte separation in flat and narrow microchannels. This approach has been considered in various ways, where it has been shown that DNA confined in microchannels, whose channel width is smaller than the gyration radius, shows significant length dependent electrophoretic mobilities [6, 129, 130]. Tentative explanations of this effect have been published in [6, 130], although an exact analytical theory is still missing. In addition to the presented separation method, a negative electrophoretic mobility of the polyelectrolyte has been reported [6] which has been explained by a combination of electroosmotic and electrophoretic effects.
Combining these effects leads to a total mobility of the polyelectrolyte which can effectively be described by a local force picture, first introduced in [131]. The global force $\vec{F}$ on the polyelectrolyte has to be balanced by the electroosmotic drag force $\vec{F}_{EOF}$ as well as by the electrophoretic force $\vec{F}_e$. Introducing the global friction coefficient ξ, the electrophoretic force is proportional to $\sim \xi\mu_e\vec{E}$ whereas the corresponding electroosmotic friction force is proportional to the polyelectrolyte velocity $\vec{v}_P$ in combination with the global friction coefficient.
The global force balance equation in general form [131] can then be written by a combination of both forces to

$$\vec{F} - \xi \cdot \left(\vec{v}_P - \frac{\mu_e}{ZeN} \cdot ZeN_c\vec{E}\right) = 0 \tag{6.1}$$

which can be solved for the polyelectrolyte velocity $\vec{v}_P$ to

$$\vec{v}_P = \left(\frac{1}{\xi} + \frac{\mu_e}{ZeN_c}\right) \cdot \vec{F} \tag{6.2}$$

with $\vec{F} = ZeN_c\vec{E}$ where ZeN_c denotes the total charge of the polyelectrolyte. By comparison with the total velocity of the chain

$$\vec{v}_P = \mu_t \vec{E}, \tag{6.3}$$

it can be shown that the friction coefficient is proportional to the inverse electroosmotic mobility with

$$\frac{1}{\xi} = \frac{\mu_{EOF}}{ZeN_c}. \tag{6.4}$$

Insertion into Eqn. (6.2) yields for the total mobility

$$\mu_t = \mu_{EOF} + \mu_e \tag{6.5}$$

which combines both electrophoretic and electroosmotic mobilities. The total velocity of the polyelectrolyte can then be written after Eqn. (6.3)

$$\vec{v}_P = (\mu_{EOF} + \mu_e)\vec{E} \tag{6.6}$$

which can result in a negative net velocity of the polyelectrolyte if $\mu_{EOF} < 0$ and $|\mu_{EOF}| \gg |\mu_e|$, as it has been reported in [6].
Taking into account the nearly constant plug like flow profile for present salt ions (*cf.* Fig. 4.2), the electroosmotic mobility can be assumed to be constant in the middle of the channel with $\mu_{EOF}(0) = \mu_{EOF}$. The corresponding expression of the electroosmotic mobility with no slip boundary conditions is given in Eqn. (4.30).
Following the assumptions of the local force picture, the total mobility is then strongly dependent on the channel geometry and the boundary characteristics which alter the migration dynamics of polyelectrolytes in small channels drastically.
This chapter focusses on the influence of the electroosmotic mobility on the total mobility of the polyelectrolyte. By varying the hydrodynamic boundary conditions, it will be shown that a negative total mobility can be derived in agreement to the results reported in [6]. It turns out that this effect is mainly caused due to slippage.

6.1 Simulation details

Simulations have been performed in the weak-coupling Poisson-Boltzmann regime. The cubic simulation box ($12\sigma \times 12\sigma \times 12\sigma$) is periodic in x- and y-direction and confined by impermeable walls in z-direction. The positions of the walls are at $z_{wall} = 0\sigma$ and $z_{wall} = 10\sigma$. Electrostatics are calculated by P3M [33] and the ELC-algorithm [39] for $2D + h$ slabwise geometries.
The remaining difference of 2σ in z-direction is due to the electrostatic gap size of

the ELC-algorithm. The walls act on the fluid particles, respectively the ions and the polyelectrolyte *via* a WCA-potential [73] of Eqn. (4.38) with the energy parameter ϵ and the cut-off distance $r_{WCA} = 2^{1/6}\sigma$. The Coulomb potential is expressed in terms of the Bjerrum length with $\lambda_B = 1.0\sigma$.
The effective density of the solvent particles is given by $\rho = 3.75\sigma^{-3}$ with a friction coefficient $\gamma = 5.0\sigma^{-1}(m\epsilon)^{1/2}$ and a mass m set to unity. The temperature is $T = 1.0\epsilon/k_B$ and the DPD timestep is $\delta t = 0.01\sigma(m/\epsilon)^{1/2}$. Tunable-slip boundary conditions are in use with friction coefficients $\gamma_L = 1.0\sigma^{-1}(m\epsilon)^{1/2}$ and $\gamma_L = 0.1\sigma^{-1}(m\epsilon)^{1/2}$. The range of the viscous layer is $z_c = 2.0\sigma$.
The Poisson-Boltzmann limit is given for a counterion density of $\rho_c = 0.0525\sigma^{-3}$ with a unit charge $Ze = 1$ and a surface charge density of $\sigma_A = -0.208e\sigma^{-2}$, which yields a coupling constant of $\Xi = 1.307$. The added salt has a concentration of $\rho_s = 0.05625\sigma^{-3}$. Half charged polyelectrolyte chains with harmonic interactions of the form

$$U_{harmonic} = \frac{1}{2}k(r_{ij} - r_0)^2 \tag{6.7}$$

with a spring constant $k = 25k_BT/\sigma^2$ and $r_0 = 1.0\sigma$, combined with WCA-interactions are used to model the monomers and the corresponding bonds. The polyelectrolyte contains of $N = 20$ monomers with monomeric charge $Ze = -1$ in all simulations. An external electric field of $E_x = -1.0\epsilon/e\sigma$ is applied on all charged particles. The walls and the polyelectrolyte are equally charged with the requirement of overall system charge electroneutrality. Charges in the wall are given in agreement to chapter 4 by randomly placed particles. Only the fluid particles are influenced by the tunable-slip boundaries. A schematic representation of the simulation setup is shown in Fig. 6.1.

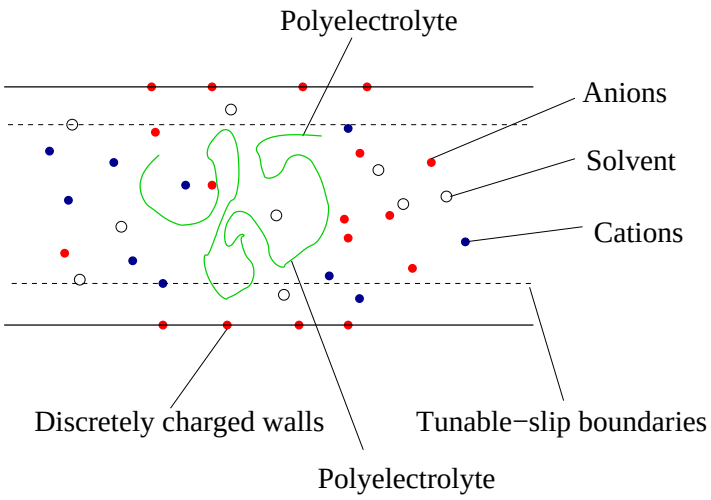

Figure 6.1: Schematic illustration of the simulation box.

6.2 Numerical results

Applying an external electric field of $E_x = -1.0\epsilon/e\sigma$ on all charged particles leads, as assumed, to a combination of electroosmotic and electrophoretic effects. The theoretical slip lengths after Eqn. (3.32) are given by $\delta_B = 1.19\sigma$ ($\gamma_L = 1.0\sigma^{-1}(m\epsilon)^{1/2}$) and $\delta_B = 14.00\sigma$ ($\gamma_L = 0.1\sigma^{-1}(m\epsilon)^{1/2}$) for a shear viscosity of $\eta_s = (1.334 \pm 0.003)\sigma^{-2}(m\epsilon)^{1/2}$. Thus the boundary conditions should alter the total mobility of the polyelectrolyte drastically due to the strong influence of the electroosmotic flow. Spurious artefacts of perturbed ion concentrations due to the presence of the polyelectrolyte can be ignored as Fig. 6.2 indicates.

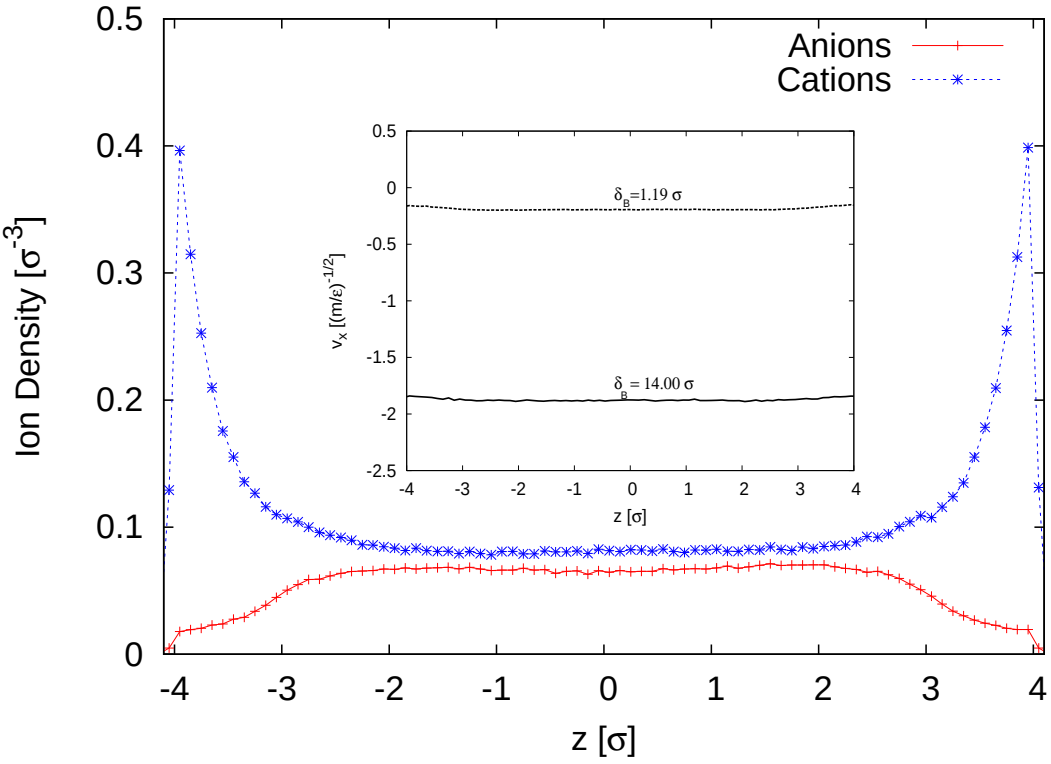

Figure 6.2: Ion density in the channel in presence of the polyelectrolyte. Inset: Corresponding plug like solvent flow profile for different slip lengths δ_B.

The system can be described in terms of the weak coupling regime by the Poisson-Boltzmann equation. Thus, the description of the electroosmotic flow in terms of coupled electrohydrodynamic equations, as it has been shown in chapter 4 is valid.
The surplus of cations in the vicinity of the channel walls due to the negatively charged surface cause a net negative electroosmotic mobility of the fluid. This is presented in the inset of Fig. 6.2, where the negative flow profiles of the fluid, depending on the slip length are shown. The drastic increase of the flow profile magnitude can be explained

Geometry	$R_e[\sigma]$	$R_g[\sigma]$
free	7.1001 ± 0.0151	2.7907 ± 0.0031
confined	7.7669 ± 0.0316	3.0352 ± 0.0069

Table 6.1: End to end Radius R_e and radius of gyration R_g for a half charged polyelectrolyte with $N = 20$ monomers in free and confined solution with a salt concentration of $\rho_s = 0.05625\sigma^{-3}$.

in terms of the slip length with $\delta_B = 14.00\sigma$ in contrast to $\delta_B = 1.19\sigma$. This is in correspondence to the analytical results of Eqns. (4.29) and (4.31).
It turns out, that the polyelectrolyte has to overcome a velocity of roughly $v_p \approx 2.0(m/\epsilon)^{-1/2}$ for a slip length of $\delta_B = 14.00\sigma$ to migrate in the corresponding direction of the applied field.
Taking the polyelectrolyte into account, the monomer probability inside the channel is presented in Fig. 6.3. As it can be seen by the fit, the distribution is dominated by a peak in the middle of the channel with a variance of $\sim 1.51\sigma$. In addition, the polyelec-

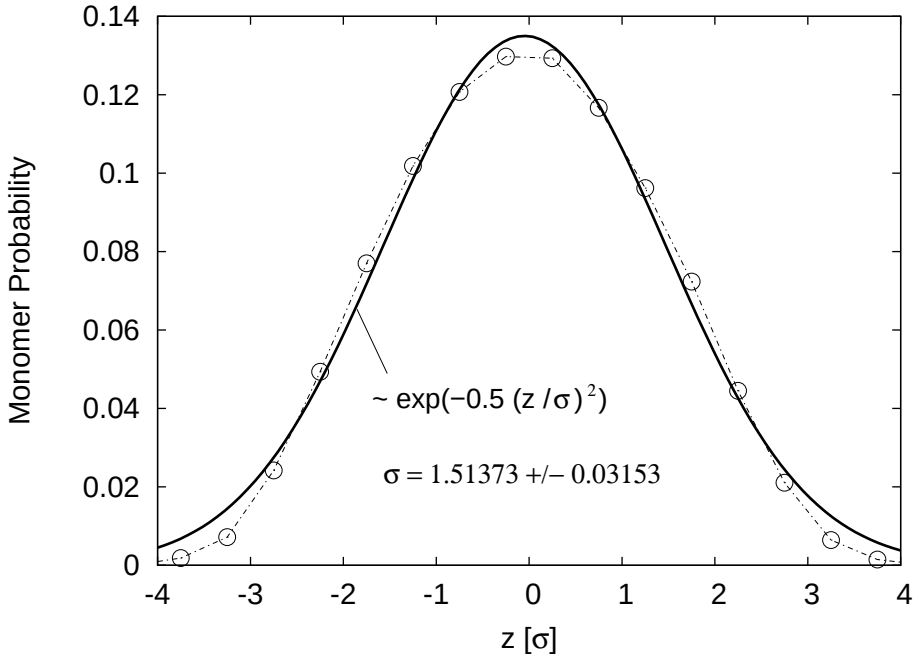

Figure 6.3: Monomer probability inside the channel.

trolyte chain is slightly stretched in contrast to a polyelectrolyte in free salt solution. This becomes obvious by studying the end to end and the gyration radius of the chain in Table 6.1. Investigating the detailed reason for this elongation is future work. Tentative

explanations are based on a possible shear-induced elongation [95], as well as on a direct squeezing due to the presence of the channel walls [117, 132]. Nevertheless, in all cases the average end to end and gyration radius is smaller than the channel length with 12σ. The total displacement of the polyelectrolyte is shown in Fig. 6.4. As it was proposed for

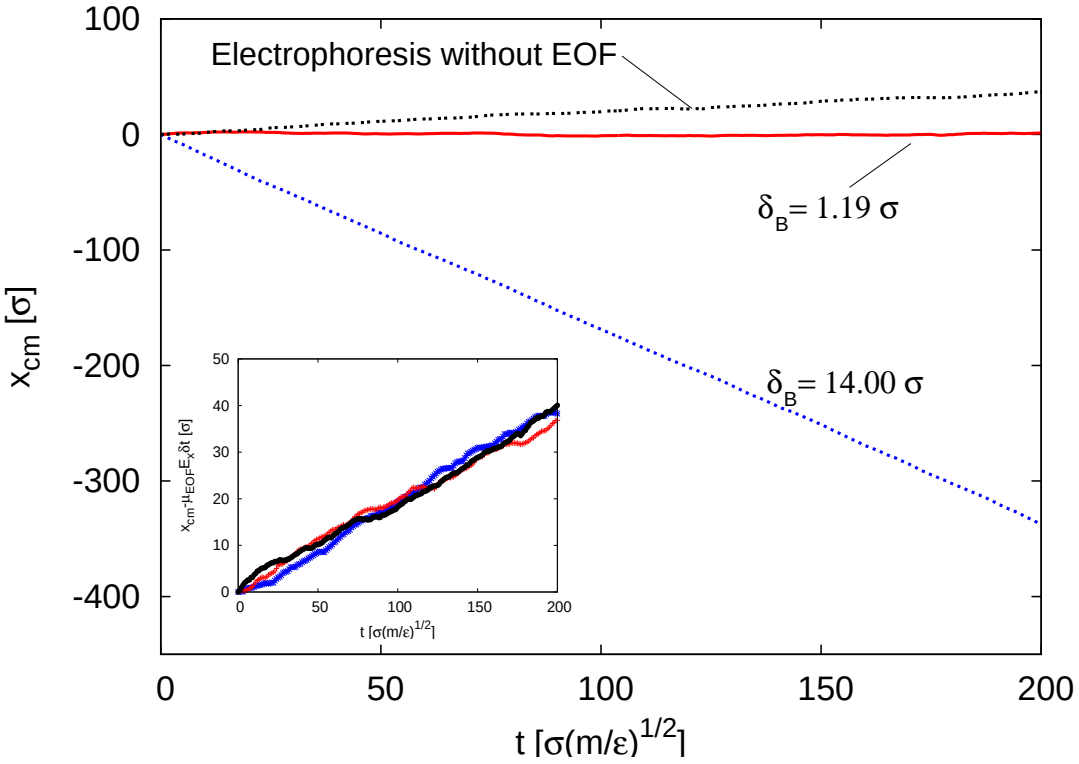

Figure 6.4: Movement of the center-of-mass of a half charged chain with $N = 20$ monomers for different slip lengths and in absence of the electroosmotic flow (black line). Inset: Movement of the center of mass subtracted by the underlying solvent velocity for identical boundary conditions as in the main figure.

the case $|\mu_{EOF}| \gg |\mu_e|$ and $\mu_{EOF} < 0$, the total mobility is reversed in the presence of varying slip lengths. Large negative total mobilities are observed for large slip lengths. Even in the case of $\delta_B = 1.19\sigma$ (red line), a small net negative total mobility can be indicated.

As it has been proposed and shown in [6], surpressing the electroosmotic flow by coating the surfaces should lead to a positive total mobility. This situation has been studied in the simulations by applying uncharged walls. The corresponding total displacement of the polyelectrolyte in absence of the electroosmotic flow is shown in Fig. 6.4 as the dotted black line. According to the displacement of the polyelectrolyte, the total mobility has to be constant with $\mu_t = \mu_e$ for $\mu_{EOF} = 0$.

EOF	$\delta_B[\sigma]$	$\mu_t[e\sigma(m\epsilon)^{-1/2}]$	$\mu_{EOF}[e\sigma(m\epsilon)^{-1/2}]$	$\mu_e[e\sigma(m\epsilon)^{-1/2}]$
yes	1.19	-0.014 ± 0.003	-0.194 ± 0.001	0.180 ± 0.004
yes	14.00	-1.694 ± 0.007	-1.880 ± 0.001	0.186 ± 0.008
no	–	0.178 ± 0.001	–	0.178 ± 0.001

Table 6.2: Various mobilities for different boundary conditions.

Calculating the total mobility of the polyelectrolyte and assuming a constant plug-like flow profile for the fluid in the middle of the channel from $z = -1.52\sigma$ to $z = 1.52\sigma$ due to the variance of the monomer distribution (Fig. 6.3), gives the possibility to compare the electrophoretic mobilities against the total mobilities.
The inset of Fig. 6.4 presents the corresponding results due to the calculated $\mu_e = \mu_t - \mu_{EOF}$. For all boundary conditions, the displacements are in good agreement with each other leading to a universal electrophoretic mobility $\mu_e \approx 0.18e\sigma(m\epsilon)^{-1/2}$ shown in Table 6.2. This quantity is independent of the boundary conditions as it has been reported in [6]. It is further possible to calculate the electroosmotic mobility for the slip length $\delta_B = 0.00\sigma$ by linear regression of the simulated flow profiles to $\mu_{EOF} = (-0.037 \pm 0.002)e\sigma(m\epsilon)^{-1/2}$.
This shows, that the total mobility of the polyelectrolyte is indeed positive for no-slip boundary conditions. Thus, the total negative mobilities of the polyelectrolye are purely related to slippage effects with slip lengths around $\delta_B \gg 1\sigma$. The presence of an electroosmotic flow in dependency of the boundary conditions therefore crucially alters the migration dynamics of the polyelectrolyte. The counter-intuitive behaviour of negative mobilities, as it has been reported in [6] can therefore be reproduced. Applying different slip lengths allows to enhance the effect drastically due to the fact that the electroosmotic mobility is strongly depending on the boundary characteristics. Thus a reversed movement of the chain in microchannels can effectively be derived and the applicability of the local force picture in Eqn. (6.1) is justified.
This shows significant deviations to ordinary electrophoretic mobilities in free solution reported in [125, 126], where electroosmotic effects have been neglected. As the numerical results indicate, for small channel widths, the electroosmotic flow profiles and the boundary characteristics have to be explicitly taken into account for a correct description of the corresponding polyelectrolyte dynamics.

7 Conclusions and outlook

Nur die Liebe und das Wetter hören nimmer, nimmer auf.
- Blixa Bargeld (1996)

Several hydrodynamic and electrokinetic effects in microchannels have been investigated in this work. It has been demonstrated that the coupling of electrostatic and hydrodynamic effects dominates the behaviour of ionic solutions on the micrometer scale in various ways. The effect of slippage in pure uncharged fluid flows has been considered. The question how to model a microchannel in a mesoscopic simulation method was the starting point. An efficient method to model the hydrodynamic boundary conditions in mesoscopic simulations, the tunable-slip boundaries approach has been presented.
Within this approach, it is possible to derive an analytic equation for the slip length. This allows to tune the slip length systematically from full- to no-slip. A viscous layer mimicks the surface friction on the fluid. This approach has been used to investigate electrohydrodynamic flow phenomena in microchannels. The counterion-induced electroosmotic flow serves as a special test case due to its analytical solubility.
Analytical equations for the flow profiles of the counterion-induced EOF in the weak-coupling regime in presence of partial- as well as no-slip boundary conditions have been derived which are in good agreement with the numerical results. A mapping scheme to match mesoscopic simulation methods, namely DPD and Lattice-Boltzmann method has been presented and tested by the counterion-induced flow. It has been shown that numerical results validate the proposed mapping scheme. The effect of electrofriction by homo- respectively inhomogeneously charged walls has been considered and the corresponding results have been shown. In the weak-coupling, as well as in the intermediate coupling regime, electrofriction plays no significant role. Furthermore it has been shown that the calculation of the flow profile by a test function in terms of standard theories in the intermediate regime is valid and produces the correct results. Even the boundary parameters, derived by studying pure uncharged fluids are identical in both investigated regimes and thus not influenced by the electrostatic interactions of the ions in the fluid.
The effects of coupled electrohydrodynamic interactions on the dynamics of polyelectrolytes in free salt solution have been investigated in detail in chapter 5.
It has been shown, that the dynamics differ to standard theories on certain length and time scales, depending on the parameters of the Debye-Hückel theory. After a characteristic time, the hydrodynamic interactions of the polyelectrolyte are effectively screened which leads to a Rouse-like behaviour. Standard theories do not predict this crossover due to a neglect of higher order corrections of the hydrodynamic forces on the polyelectrolyte. A tentative explanation has been presented which includes this higher order correction scheme. The numerical results have shown that the chain is massively dom-

inated by electrostatic interactions, whose effects cause spurious artefacts in several dynamical observables. This sheds a new light on polyelectrolyte simulations which neglect hydrodynamic interactions, *e. g.* diffusion of DNA through nanopores which could be closer to reality than assumed.
Furthermore the results of polyelectrolyte electrophoresis in confined geometries have been presented. It turned out, that the experimental results of a recent publication [6] are reproducible by computer simulations. Thus the corresponding underlying local force picture [131] is valid. The results have shown that in small confined geometries the combined effects of electrophoresis and electroosmosis cannot be neglected and lead to a varying total mobility of the polyelectrolyte, depending on the boundary conditions.
Future work may include structured microchannels to investigate the Brownian Dynamics results of [127] with a full combination of hydrodynamic and electrostatic interactions. The interaction of the polyelectrolyte with the surface is therefore of main interest due to an efficient modelling of modern experimental devices.
Further experimental work on dielectrophoresis raised questions which can not be answered fully by Brownian Dynamics simulations [133]. The reported combined effects of polarisabilty and present obstacles in the channel can only be investigated in detail by incorporating electrohydrodynamic phenomena in the simulations.
The reported size separation techniques for polyelectrolytes in flat narrow geometries have to be investigated in detail [6]. First steps in this direction have been undertaken where interesting results in different electrostatic coupling regimes have been derived [134].
An application of the tunable-slip boundaries approach has recently been used [135] to investigate the behaviour of chiral molecules in shear- and pressure driven flows. Chiral separation has been demonstrated and slippage was crucial to reproduce this effect.
Work still in progress is the simulation of long polyelectrolyte chains up to 500 monomers to investigate the dynamic crossover from Zimm- to Rouse dynamics in the long chain limit. Although the presented results are validated by the comparison with uncharged polymers, large polyelectrolyte chains allow to investigate even longer timescales in detail.
Further attempts on investigating the repulsive DPD-forces on the tunable-slip boundary interactions have recently been undertaken [75]. The results may help to understand the results of mesoscopic simulation methods with conservative interactions under the conditions of slippage.
Full understanding of polyelectrolyte behaviour in several electrostatic regimes and in different geometries is the ultimate future goal for polymer scientists. A combination of various methods, mesoscopic as well as microscopic simulation techniques will hopefully lead to a promising way of understanding biomolecular and solvent behaviour on the microscale in detail.

A Calculation of the slip length and the hydrodynamic boundary positions

A.1 Hydrodynamic boundary positions

Assuming that the fluid density is constant in the absence of conservative interparticle forces (*cf.* Fig. 3.5), the Stokes equation for a flow in x-direction is given by Eqn. (3.13) with

$$F_x = -\gamma_L \omega_L(z) v_x(z) + F_x^{ext} \tag{A.1}$$

by comparison with Eqn. (3.7) in presence of the viscous layer, where the first moment of the random force $< F^R >= 0$ vanishes. With a constant density ρ_0, Eqn. (3.13) can be rewritten to

$$\eta_s \frac{\partial^2}{\partial z^2} v_x(z) = \gamma_L \omega_L(z) \rho_0 v_x(z) - \rho_0 F_x^{ext}. \tag{A.2}$$

The boundary conditions of the fluid-solid surface at $z_0 = 0$ imply [50]

$$\eta_s \frac{\partial}{\partial z} v_x(z_0) = 0 \tag{A.3}$$

which means that the derivative of the fluid velocity at this position vanishes. As it was mentioned in chapter 3, a phenomenological description of the atomistic friction is needed. Therefore the microscopic description of the boundaries is replaced by an effective description of the boundary conditions.
Neglecting the presence of the viscous layer and assuming an unperturbed flow profile $v_x^{(0)}$, the effect of slippage can be described by the effects of the viscous stresses given by Eqn. (3.2) and Eqn. (3.3). Neglecting for a moment the presence of the viscous layer, the equality of the viscous stresses is even valid for an unperturbed flow profile $v_x^{(0)}$. The viscous stress of the boundaries exerted by microscopic friction on the fluid particles which is proportional to the mean force $< F_x >$ per area at the hydrodynamic boundary conditions z_B is then given by

$$\sigma_{xz}^B = -\frac{< F_x >}{A} = \zeta_B v_x^{(0)}(z) \tag{A.4}$$

and proportional to an *a priori* unknown boundary friction coefficient ζ_B. The viscous stress arising from the bulk fluid acting on the boundary fluid particles σ_{xz}^F yields

$$\sigma_{xz}^F = -\frac{< F_x >}{A} = \eta_s \frac{\partial}{\partial z} v_x^{(0)}(z) \tag{A.5}$$

with the gradient of the unperturbed fluid velocity $\partial_z v_x^{(0)}(z_B)$. At the hydrodynamic boundary positions z_B both forces are exactly equal. Comparison with Eqn. (3.4) shows that the slip length can be identified to

$$\delta_B = \frac{\eta_s}{\zeta_B} \tag{A.6}$$

which is the ratio of the shear viscosity η_s and the friction coefficient ζ_B.
The calculation of the slip length is possible if an expression for the unknown ζ_B can be derived. Following this approach the extended Stokes equation for low Reynolds numbers and incompressible fluids is given by Eqn. (A.2). The theory is based on one crucial assumption: The Navier-Stokes equations are taken to be valid on the length scale z_c of the cutoff. This assumption may seem bold, given that z_c will typically be chosen of the order of one particle diameter. The coordinate system is chosen such that the surface is at rest and located at $z = 0$. It is assumed that the fluid viscosity does not change in the vicinity of the walls. Furthermore it is stated that the viscous force $\gamma_L\, \omega_L(z)\, v_x(z)$ is only active within a layer of finite thickness z_c. The total friction force per surface area generated in this layer is given by

$$-\frac{< F_x >}{A} = \rho_0\, \gamma_L \int_0^{z_c} \mathrm{d}z\, \omega_L(z)\, v_x(z). \tag{A.7}$$

This expression has to be replaced by an effective boundary between a solid and an unperturbed fluid, *i.e.*, a hypothetical fluid not subjected to the additional viscous forces in the layer. The friction force per surface area, F_x/A, is then equal to the frictional stress on the solid, and to the shear stress on the unperturbed fluid at the position $z = z_B$ of the boundary. This yields the effective boundary conditions

$$-\frac{< F_x >}{A} = \zeta_B v_x^{(0)}(z_B) = \eta_s \frac{\partial}{\partial z} v_x^{(0)}(z_B). \tag{A.8}$$

First it is shown that the hydrodynamic boundary must be identical with the physical boundary

$$z_B = 0. \tag{A.9}$$

To this end, Eqn. (A.2) has to be taken for a partial integration which has to be performed by taking advantage of the boundary condition Eqn. (A.3), to obtain

$$-\frac{< F_x >}{A} = \eta_s \frac{\partial}{\partial z} v(z_c) + \rho F_x^{ext} z_c. \tag{A.10}$$

According to Eqn. (A.8), this must be equal to $\eta_s \partial_z v_x^{(0)}(z_B)$. The unperturbed velocity profile $v_x^{(0)}$ solves the Stokes equation at $\gamma_L = 0$ with the boundary conditions

$$v_x^{(0)}(z_c) = v_x(z_c); \quad \frac{\partial}{\partial z} v_x^{(0)}(z_c) = \frac{\partial}{\partial z} v_x(z_c). \tag{A.11}$$

The following relation can be obtained

$$v_x^{(0)}(z) = v_x(z_c) + \frac{\partial}{\partial z} v_x(z_c)(z - z_c) - \frac{\rho_0}{2\eta_s} F_x^{ext} (z - z_c)^2 \tag{A.12}$$

and hence

$$\eta_s \frac{\partial}{\partial z} v_x^{(0)}(z_B) = \eta_s \frac{\partial}{\partial z} v_x(z_c) + F_x^{ext} \rho_0 (z_c - z_B). \tag{A.13}$$

Comparing Eqs. (A.13) and (A.10) gives Eqn. (A.9) which can be stated to

$$z_B = z_0 \tag{A.14}$$

if $z_0 = 0$ which is in agreement. Thus the theory should hold for not too drastic pertubations such that the Stokes equation is nearly valid in the viscous layer.

A.2 Slip length

The slip length is calculated as shown in the following. This is most conveniently done for the case $F_x^{ext} = 0$. Eqn. (A.2) is integrated for given $v_x(0) =: v_0$ and $\partial_z v_x(0) = 0$ (Eqn. (A.3)) to get $v_x(z_c)$ and $\partial_z v_x(z_c)$ *via* Eqn. (A.12). Then the values $v_x^{(0)}(z_B)$ and $v_x^{(0)\prime}(z_B)$ of the unperturbed profile at the hydrodynamic boundary have to be determined. This finally allows to calculate the slip length from

$$\delta_B = v_x^{(0)}(z_B) / \partial_z v_x^{(0)}(z_B) \tag{A.15}$$

(*c. f.*) Eqn. (A.8)). All profiles scale linearly with v_0, hence the final expression for the slip length does not depend on v_0 any more. More generally, the result depends only on the dimensionless quantity α defined in Eqn. (3.31), in the sense that the slip length in units of z_c, *i.e.*, the quantity δ_B / z_c, can be written as a function of α only. If $\omega_L(z)$ drops linearly to zero, $\omega_L(z) = 1 - z/z_c$, the profile can be written as given in Eqn. (3.33). This will be shown in the following. In the absence of an external force ($F_x^{ext} = 0$), the general solution of Eqn. (A.2) for a linear weight function reads

$$v_x(z) = A\,\mathrm{Ai}(c(1 - z/z_c)) + B\,\mathrm{Bi}(c(1 - z/z_c)) \tag{A.16}$$

with $c = -(-\alpha)^{1/3}$, where Ai and Bi are the Airy functions and α has been defined in Eqn. (3.31). The boundary conditions $v_x(0) = v_0, \partial_z v_x(0) = 0$ determine the coefficients

$$A = v_0 \mathrm{Ai}'(c) / (\mathrm{Ai}'(c)\mathrm{Bi}(c) - \mathrm{Ai}(c)\mathrm{Bi}'(c)) \tag{A.17}$$

$$B = v_0 \mathrm{Bi}'(c) / (\mathrm{Ai}'(c)\mathrm{Bi}(c) - \mathrm{Ai}(c)\mathrm{Bi}'(c)). \tag{A.18}$$

The unperturbed profile is linear, $v_x^{(0)}(z) = v_x(z_c) + \frac{\partial}{\partial_z} v_x(z_c)(z - z_c)$, and the hydrodynamic boundary is located at $z_B = 0$ according to Eqn. (A.9), hence the equation (A.15) for the slip length can be written as

$$\frac{\delta_B}{z_c} = \frac{v_x(z_c)}{z_c \partial_z v_x(z_c)} - 1. \tag{A.19}$$

Inserting this in Eqns. (A.16) with (A.17) and (A.18) and using the identities $\mathrm{Ai}(0) = 1/(3^{2/3}\Gamma(\frac{2}{3}))$, $\mathrm{Ai}'(0) = -1/(3^{1/3}\Gamma(\frac{1}{3}))$, $\mathrm{Bi}(0) = \sqrt{3}\mathrm{Ai}(0)$, and $\mathrm{Bi}'(0) = -\sqrt{3}\mathrm{Ai}'(0)$, where Γ is the Euler gamma function, one obtains

$$\frac{\delta_B}{z_c} = -1 - \frac{1}{3^{1/3} c} \frac{\Gamma(\frac{1}{3})}{\Gamma(\frac{2}{3})} \frac{\mathrm{Ai}'(c)\sqrt{3} - \mathrm{Bi}'(c)}{\mathrm{Ai}'(c)\sqrt{3} + \mathrm{Bi}'(c)}. \tag{A.20}$$

To get rid of the complex argument c, the series expansion of the Airy functions [136, 137] is used. The functions of interest can be written as $\mathrm{Ai}'(z)\sqrt{3} = I_1 - I_2$ and $\mathrm{Bi}'(z) = I_1 + I_2$ with

$$\begin{aligned} I_1 &= \frac{z^2}{3\,3^{1/6}} \sum_k \frac{1}{\Gamma(k+5/3)\,k!} \left(\frac{z^3}{9}\right)^k \\ I_2 &= 3^{1/6} \sum_k \frac{1}{\Gamma(k+1/3)\,k!} \left(\frac{z^3}{9}\right)^k . \end{aligned}$$

Comparing this with the series representation of the modified Bessel function of the first kind,

$$I_\nu(z) = \left(\frac{z}{2}\right)^\nu \sum_k \frac{1}{\Gamma(k+\nu+1)\,k!} \left(\frac{z}{2}\right)^{2k}, \tag{A.21}$$

one easily verifies the identities

$$I_1 = -\frac{\alpha^{1/3}}{\sqrt{3}}\, I_{-2/3}\left(\frac{2\sqrt{\alpha}}{3}\right)$$

and

$$I_2 = \frac{\alpha^{2/3}}{\sqrt{3}c}\, I_{2/3}\left(\frac{2\sqrt{\alpha}}{3}\right).$$

Inserting this into Eqn. (A.20) gives Eqn. (3.33). The slip length can become zero (corresponding to no-slip) or even negative. The no-slip boundary condition is obtained at $\alpha = 3.973$ for a linear weight function. Negative slip lengths are encountered at even larger α. In this case, the hypothetical unperturbed profile $v_x^{(0)}$ changes sign close to the boundary. As it was mentioned in chapter 3 the true velocity profile, $v_x(z)$, never changes sign which indicates that negative slip lengths do not correspond to unphysical situations.

In the regime of positive slip lengths, α is small and can be used as an expansion parameter. Expanding Eqn. (A.19) in powers of α gives Eqn. (3.32). More generally, one can derive a useful expression for arbitrary weight functions. Note that the true velocity profile and the unperturbed profile are identical at the order α^0, *i.e.*, $v_x(z) = v_x^{(0)}(z) + \mathcal{O}(\alpha)$. Furthermore, the derivative of the velocity profiles is of order α, by virtue of Eqns. (A.7), (A.3), and (A.13), hence one even has $v_x(z) = v_x^{(0)}(z_B) + \mathcal{O}(\alpha)$. Applying once more Eqs. (A.7), (A.3), and (A.12), Eqn. (3.30) is obtained. This equation allows to estimate the slip length reasonably accurately for arbitrary choices of the weight function $\omega_L(z)$.

B Calculation of the decay factor for the Rouse modes

It can be shown [26] that the decay factor $\Gamma(p)$ of the Rouse modes is given by

$$\Gamma(p) = -\frac{d}{dt}\left(\frac{< \vec{X}_p(t)\vec{X}_p(t_0) >}{< \vec{X}_p^2(t_0) >}\right) \tag{B.1}$$

which can also be written in terms of the Linear-response theory [7] or based on the Smoluchowski equation to

$$\Gamma(p) = -\frac{d}{dt}\left(\left\langle \frac{\partial X_{p\gamma}}{\partial r_{i\alpha}} D_{ij\beta\alpha} \frac{\partial X_{p\gamma}}{\partial r_{j\beta}} \right\rangle\right) \tag{B.2}$$

with the diffusion tensor $D_{ij\beta\alpha}$. Evaluating this expression gives

$$\Gamma(p) = \frac{1}{N^2 < \vec{X}_p^2(t_0) >} \sum_{i,j} \cos\left(\frac{p\pi}{N}\left(i - \frac{1}{2}\right)\right) \cos\left(\frac{p\pi}{N}\left(j - \frac{1}{2}\right)\right) Tr < \mathbf{D}_{ij} > \tag{B.3}$$

with the trace of the pre-averaged diffusion tensor $Tr < \mathbf{D}_{ij} >$. The direct calculation of the decay factor for the Zimm-Dynamics is given in [26]. In this publication, the following finite-size corrected expression has been derived

$$\Gamma(p) = A\frac{2}{\pi^2}\frac{k_B T}{\eta_s b^3}\left(\frac{p\pi}{N}\right)^{3\nu} r(p) \tag{B.4}$$

with the bond length b, a constant A and the finite-size correction $r(p)$. The uncharged chain with Zimm Dynamics therefore behaves as

$$-\log\left(\frac{< \vec{X}_p(t)\vec{X}_p(t_0) >}{< \vec{X}_p^2(t_0) >}\right) = \Gamma^Z(p)t \sim \left(\frac{p\pi}{N}\right)^{3\nu} r(p)t \tag{B.5}$$

for the Rouse modes of a single chain with full consideration of hydrodynamic interactions.
The decay factor behaves differently in absence of hydrodynamic interactions. The finite size expression relies on the calculation of the trace of the pre-averaged Diffusion tensor $Tr < \mathbf{D}_{ij} >$. The following expression [26] for the time-independent $< \vec{X}_p^2(t_0) >$ relies on scaling arguments and can be directly evaluated by

$$< \vec{X}_p^2(t_0) >= \frac{b^2 N^{2\nu}}{2(p\pi)^{1+2\nu}} f(p) \tag{B.6}$$

with a finite size correction $f(p)$. Calculating the trace of the pre-averaged diffusion tensor with the assumption of hydrodynamic screening yields

$$Tr < \mathbf{D}_{ij} > \sim N^{-1} \tag{B.7}$$

which can be inserted into Eqn. (B.3) together with Eqn. (B.6). This gives the following scaling relation

$$-\log\left(\frac{< \vec{X}_p(t)\vec{X}_p(t_0) >}{< \vec{X}_p^2(t_0) >}\right) = \Gamma(p)^R t \sim \frac{\left(\frac{p\pi}{N}\right)^{2\nu+1}}{f(p)} t \tag{B.8}$$

as it is used in chapter 5.

C Polyelectrolyte dynamics in free salt solution

C.1 Relaxation of the ion distribution around a polyelectrolyte

It is assumed that the ion distribution in equilibrium is given by the Debye-Hückel theory. The timescale on which this distribution is reached will be calculated in the following. The corresponding inverse Debye-Hückel length can be written after Eqn. (4.26)

$$\kappa_D^2 = \sum_i \frac{(Z_i e)^2 \rho_{i,0}^{eq}}{\epsilon_r k_B T} \tag{C.1}$$

where the equilibrium distribution of each ion density $\rho_{i,0}^{eq}$ is used. The ion charge distribution in the system is given by

$$\rho_c(\vec{k}) = \sum_i Z_i e \rho_i(\vec{k}) + Z_M e \sum_j e^{i\vec{k}\vec{R}_j} \tag{C.2}$$

where $Z_i e$ denotes the charge of ion density ρ_i and $Z_M e$ denotes the monomeric charge at positions $\vec{R}_j$.
With the assumption

$$\vec{v}\vec{\nabla}\rho_i \approx 0, \tag{C.3}$$

the diffusion equation (Eqn. (5.45)) for each ion species can be written

$$\xi_0 \frac{\partial}{\partial t}\rho_i(\vec{r},t) = \vec{\nabla}(k_B T \vec{\nabla}\rho_i(\vec{r},t) + \rho_i(\vec{r},t) Z_i e \vec{E}(\vec{r},t)) \tag{C.4}$$

which is valid after the ballistic time t_b with the friction coefficient ξ_0.
The Fourier transformed ionic Debye-Hückel charge distribution is given by [113]

$$\rho_c^{eq}(\vec{k}) = -Z_M e \frac{\kappa_D^2}{k^2 + \kappa_D^2} \sum_j e^{i\vec{k}\vec{R}_j} \tag{C.5}$$

which is the equilibrium distribution of the ionic charge around the charged monomers of the polyelectrolyte. One can assume, that after a characteristic time Eqn. (C.2) has to be replaced by Eqn. (C.5) in the simplest mean-field approach. Applying

$$\vec{\nabla}(Z_i e \rho_i \vec{E}) \approx Z_i e \rho_i^{eq} \vec{\nabla}\vec{E}, \tag{C.6}$$

which should be valid in the Debye-Hückel limit for the dynamical as well as the static behaviour of the ions, together with Eqns. (C.1), (C.6) and the Poisson equation

$$\vec{\nabla}\vec{E}_i = \sum_i \frac{Z_i e \rho_{i,0}^{eq}(\vec{r})}{\epsilon_r}, \tag{C.7}$$

a modified diffusion equation can be identified by

$$\left(\frac{\partial}{\partial t} + \frac{1}{\tau_D(\vec{k})}\right) \sum_i Z_i e \rho_i(\vec{k},t) = \frac{\rho_c^{eq}(\vec{k},t)}{\tau_D(\vec{k})} \tag{C.8}$$

which shows that the actual ionic charge distribution $\sum_i Z_i e \rho_i(\vec{k})$ relaxes against a Debye-Hückel charge distribution $\rho_c^{eq}(\vec{k},t)$ in a time

$$\tau_D(\vec{k}) = \frac{\xi_0}{k_B T(k^2 + \kappa_D^2)} \tag{C.9}$$

which strongly depends on κ_D and the ionic friction coefficient ξ_0 which is inverse proportional to the ionic mobility $\xi_0^{-1} = \zeta$.

C.2 Force contributions on the chain dynamics

To investigate the influence of the different force contributions on the dynamics, the Fourier-transformed Stokes equation (Eqn. (5.26)) with Eqn. (5.27) is calculated with the corresponding contributions of the present forces. Mainly two force contributions are present in the investigated chain. In general these contributions can be written as

$$\vec{F}(\vec{r}) = \rho_c(\vec{r})\vec{E}(\vec{r}) - \sum_i \delta(\vec{r} - \vec{R}_i)\, \frac{\partial U(\vec{R}_i)}{\partial \vec{R}_i} \tag{C.10}$$

with the underlying potential energy $U(\vec{R}_i)$ on a monomer at $\vec{R}_i$ and the charge density ρ_c together with the electric field $\vec{E}$. Changing into Fourier space yields for the non electrostatic forces

$$\vec{F}^{ne}(\vec{k}) = -\sum_i e^{i\vec{k}\vec{R}_i} \sum_l \frac{\partial U(\vec{R}_i)}{\partial \vec{R}_i} = \sum_i e^{i\vec{k}\vec{R}_i} \sum_l \hat{d}_{il}\, U'(d_{il}) \tag{C.11}$$

with $\vec{d}_{ij} = \vec{R}_{i+l} - \vec{R}_i$, $\hat{d}_{il} = \vec{d}_{il}/d_{il}$ and the derivative of the potential energy $U'(d_{il})$. The electrostatic force can be written after continous Fourier transformation to

$$\vec{F}^e(\vec{k}) = \frac{1}{(2\pi)^3} \int d\vec{k}'\, \rho_c(\vec{k} - \vec{k}')\, \vec{E}(\vec{k}') \tag{C.12}$$

which yields after insertion with the solution of the Poisson equation (Eqn.(4.6))

$$\vec{E}(\vec{k}') = -4\pi i \frac{\vec{k}'}{k'^2}\, \rho_c(\vec{k}') \tag{C.13}$$

the following relation

$$\vec{F}^e(\vec{k}) = -\frac{i}{2\pi^2}\int d\vec{k}'\rho_c(\vec{k}-\vec{k}')\frac{\vec{k}'}{k'^2}\,\rho_c(\vec{k}') \tag{C.14}$$

which has to be evaluated. Assuming a Debye-Hückel charge distribution ρ_c^{eq} by Eqn. (C.5) and inserting for ρ_c yields

$$\vec{F}^e(\vec{k}) = -\frac{(Z_M e)^2}{2\pi^2}\,i\,\sum_{il}\int d\vec{k}'\;e^{i(\vec{k}-\vec{k}')\vec{R}_i}\;e^{i\vec{k}'\vec{R}_l}\;\frac{(\vec{k}-\vec{k}')^2}{(\vec{k}-\vec{k}')^2+\kappa_D^2}\;\frac{\vec{k}'}{k'^2+\kappa_D^2} \tag{C.15}$$

where the definition of $\vec{d}_{il}$ can be used to rewrite Eqn. (C.15) to

$$\vec{F}^e(\vec{k}) = -\frac{(Z_M e)^2}{2\pi^2}\,i\,\sum_{i}e^{i\vec{k}\vec{R}_i}\sum_{l}\int d\vec{k}'e^{i\vec{k}'\vec{d}_{il}}\;\frac{(\vec{k}-\vec{k}')^2}{(\vec{k}-\vec{k}')^2+\kappa_D^2}\;\frac{\vec{k}'}{k'^2+\kappa_D^2} \tag{C.16}$$

where the assumption $k \ll \kappa_D$ results in

$$(\vec{k}-\vec{k}')^2+\kappa_D^2 \approx k'^2+\kappa_D^2. \tag{C.17}$$

Defining $\vec{q} = (\vec{k}'-\vec{k})/\kappa_D$ together with Eqn. (C.16) gives

$$\vec{F}^e(\vec{k}) = -\frac{(Z_M e)^2}{2\pi^2}\,i\,\sum_{i}e^{i\vec{k}\vec{R}_i}\sum_{l}e^{i\vec{k}\vec{d}_{il}}\;\kappa_D^2\;\int d\vec{q}\,e^{i\vec{q}(\vec{d}_{il}\kappa_D)}\;\frac{q^2}{(q^2+1)^2}\left(\frac{\vec{k}}{\kappa_D}+\vec{q}\right) \tag{C.18}$$

where the following identities can be defined

$$\begin{aligned} I(x) &= \frac{1}{\pi^2}\int d\vec{q}\,e^{i\vec{q}\vec{x}}\frac{q^2}{(q^2+1)^2} \\ &= \frac{4}{\pi}\int_0^\infty dq\frac{q^4}{(q^2+1)^2}\frac{\sin qx}{qx} \\ &= \frac{2-|x|}{|x|}\,e^{-|x|} \\ I'(x) &= \frac{dI(x)}{d|x|} = \frac{|x|^2-2|x|-2}{|x|^2}\,e^{-|x|} \end{aligned}$$

to simplify the expressions above. Inserting these expressions in Eqn. (C.18) yields together with the identity

$$\frac{\partial I(x)}{\partial\vec{x}} = \frac{1}{\pi^2}\,i\,\int d\vec{q}\,e^{i\vec{q}\vec{x}}\frac{q^2}{(q^2+1)^2}\vec{q} = I'(x)\cdot\hat{x}. \tag{C.19}$$

the following expression

$$\vec{F}^e(\vec{k}) = -\frac{(Z_M e)^2}{2}\,i\,\sum_{i}e^{i\vec{k}\vec{R}_i}\sum_{l}e^{i\vec{k}\vec{d}_{il}}\;\kappa_D^2\;\left(\frac{\vec{k}}{\kappa_D}I(\kappa_D d_{il}) - i\hat{d}_{il}I'(\kappa_D d_{il})\right). \tag{C.20}$$

The forces on a single monomers sum up to a total force

$$\vec{F}(\vec{k}) = \sum_i \; e^{i\vec{k}\vec{R}_i} \; \vec{F}^{(i)}(\vec{k}) \tag{C.21}$$

where the force of Eqn. (C.20) together with Eqn. (C.11) finally is given by

$$\begin{aligned} \vec{F}^{(i)}(\vec{k}) \;\; &= \;\; -i \; \vec{k}\kappa_D \frac{(Z_M e)^2}{2} \sum_i \; e^{i\vec{k}\vec{d}_{il}} \; I(\kappa_D d_{il}) \\ &\quad + \sum_l \left(\hat{d}_{il} \left[U'(d_{il}) - e^{i\vec{k}\vec{d}_{il}} \; \frac{(Z_M e)^2}{2} \kappa_D^2 I'(\kappa_D d_{il}) \right] \right). \end{aligned} \tag{C.22}$$

If now the flow velocities of the single monomers are explicitly considered, Eqn. (5.26) can be rewritten with

$$\vec{v}(\vec{k}) = \sum_i e^{i\vec{k}\vec{R}_i} \; \vec{v}^{(i)}(\vec{k}) \tag{C.23}$$

and splitted into

$$\vec{v}^{(i)}(\vec{k}) \;\; = \;\; \frac{1}{\eta_s k^2} \sum_l (\mathbf{1} - \hat{k}\hat{k}) \left[\hat{d}_{il} \left(U'(d_{il}) - \frac{(Z_M e)^2}{2} \; \kappa_D^2 \; I'(\kappa_D d_{il}) \right) \right] \tag{C.24}$$

$$+ \frac{1}{\eta_s k} \sum_l (\mathbf{1} - \hat{k}\hat{k}) \left[-i\hat{d}_{il}(\hat{k}\vec{d}_{il}) \frac{(Z_M e)^2}{2} \; \kappa_D^2 \; I'(\kappa_D d_{il}) \right] \tag{C.25}$$

$$+ \mathcal{O}(k) \tag{C.26}$$

due to its distributions, where several lines indicate different dynamical behaviour as it was shown in chapter 5.
Back transformation into normal coordinates offers the possibilty to investigate the different terms in more detail. Line C.24 is proportional to $\sim \sum_l (\mathbf{1} - \hat{k}\hat{k}) \cdot \hat{d}_{il}$ whereas line C.25 is given by $\sim \sum_l (\mathbf{1} - \hat{k}\hat{k}) \cdot \hat{d}_{il}(\hat{k}\vec{d}_{il})$. The time average vanishes for $< \sum_l \hat{d}_{il}(t) >= 0$ due to its uneven character, but $< \sum_l \hat{d}_{il}(t)\vec{d}_{il}(t) > \neq 0$ does not vanish. Thus Eqn. (C.25) dominates Eqn. (C.24) and therefore the whole dynamics for times $t > t_0$ where t_0 is the proposed crossover time of chapter 5.
A more compact form to rewrite Eqns. (C.24), (C.25) and (C.26) for the central monomer α is given by

$$\vec{v}^{(\alpha)}(\vec{k}) = \frac{1}{\eta_s k^2} \sum_\gamma \left[F_{\alpha\gamma}(\vec{k}) + Z_\alpha Z_\gamma e^2 \; \kappa_D^2 g(r_{\alpha\gamma}\kappa_D) e^{i\vec{k}\cdot\vec{r}_{\alpha\gamma}} \right] (\mathbf{1} - \hat{k}\hat{k}) \cdot \hat{r}_{\alpha\gamma} \tag{C.27}$$

with

$$g(x) = e^{-x} \; \frac{x^2/2 - x - 1}{x^2} \tag{C.28}$$

where $F_{\alpha\gamma}(\vec{k})$ denotes the corresponding non electrostatic force contributions with $\vec{r}_{\alpha\gamma} = \vec{R}_\gamma - \vec{R}_\alpha$ and the central monomer charge $Z_\alpha e$. The back transformation into the cartesian

space can be splitted into the corresponding mixed non- and electrostatic force monopole term

$$\vec{v}_m^{(\alpha)}(\vec{r}) = \frac{1}{8\pi\eta_s r} \sum_\gamma \left[F_{\alpha\gamma} + Z_\alpha Z_\gamma e^2 \ \kappa_D^2 g(r_{\alpha\gamma}\kappa_D)\right] (\mathbf{1} + \hat{r}\hat{r}) \cdot \hat{r}_{\alpha\gamma} \tag{C.29}$$

and the electrostatic force dominated dipole term

$$\vec{v}_d^{(\alpha)}(\vec{r}) = \frac{1}{8\pi\eta_s} \frac{\vec{r}}{r^3} \sum_\gamma \left[Z_\alpha Z_\gamma e^2 \kappa_D^2 \ g(r_{\alpha\gamma}\kappa_D)\right] \ \vec{r}_{\alpha\gamma} \cdot (3\hat{r}\hat{r} - \mathbf{1}) \cdot \hat{r}_{\alpha\gamma} \tag{C.30}$$

where higher contributions have been neglected. The corresponding prefactors of of the expressions above show a $1/r$, respectively $1/r^3$ behaviour which correspond to non-screenend and screenend hydrodynamic interactions as explained in chapter 5.
Again for a locally straight chain, the contributions of the vectors $\vec{r}_{\alpha\gamma}$ are balanced by $\vec{r}_{\alpha\gamma'} = -\vec{r}_{\alpha\gamma}$ which is true for time-averaged chains. By defining

$$\mathbf{G}_1(t) = \sum_\gamma Z_\alpha Z_\gamma e^2 \ g(r_{\alpha\gamma}\kappa_D) \ \hat{r}_{\alpha\gamma} \tag{C.31}$$

and

$$\mathbf{G}_2(t) = \sum_\gamma Z_\alpha Z_\gamma e^2 \ g(r_{\alpha\gamma}\kappa_D) \ \vec{r}_{\alpha\gamma}\hat{r}_{\alpha\gamma} \tag{C.32}$$

the time behaviour of the different contributions can be investigated for a dynamic chain. Fig. C.1 presents the decay of the monopole contribution $\mathbf{G}_1(t)$ which corresponds to

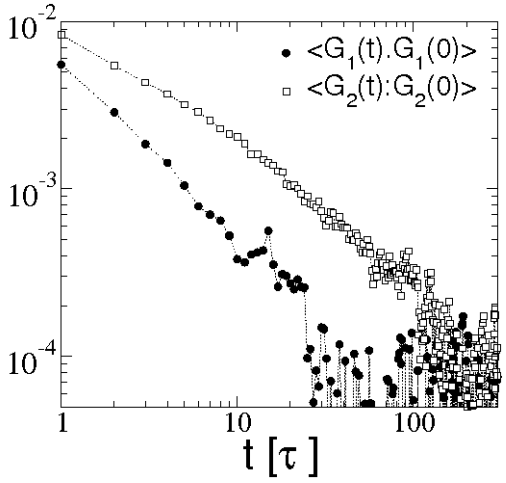

Figure C.1: Decay of contributions $\mathbf{G}_1(t)$ and $\mathbf{G}_2(t)$ by a time-averaged chain. Reproduced from [138].

the mixed non-electrostatic and electrostatic forces and the dipole contributions $\mathbf{G}_2(t)$ which represents pure electrostatic contributions.
As it is evident, the monopole contributions decay faster than the dipole contributions

which means that the electrostatic contributions dominate after a characteristic time. This contribution leads, as it was earlier discussed in chapter 5, to a hydrodynamic screening crossover. Thus the polyelectrolyte is dominated by the electrostatic contributions which massively influence the dynamics of the chain and finally lead to a screening of hydrodynamic interactions.

D Flow profiles for conservative interactions

The influence of the conservative forces (Eqn. 2.3) on uncharged fluid flows is shown in Fig. D.1.
A non monotonic behaviour of the shear viscosity calculated by the corresponding flow profiles and Eqn. (3.19) is presented in Fig. D.2. Following the calculation of the shear

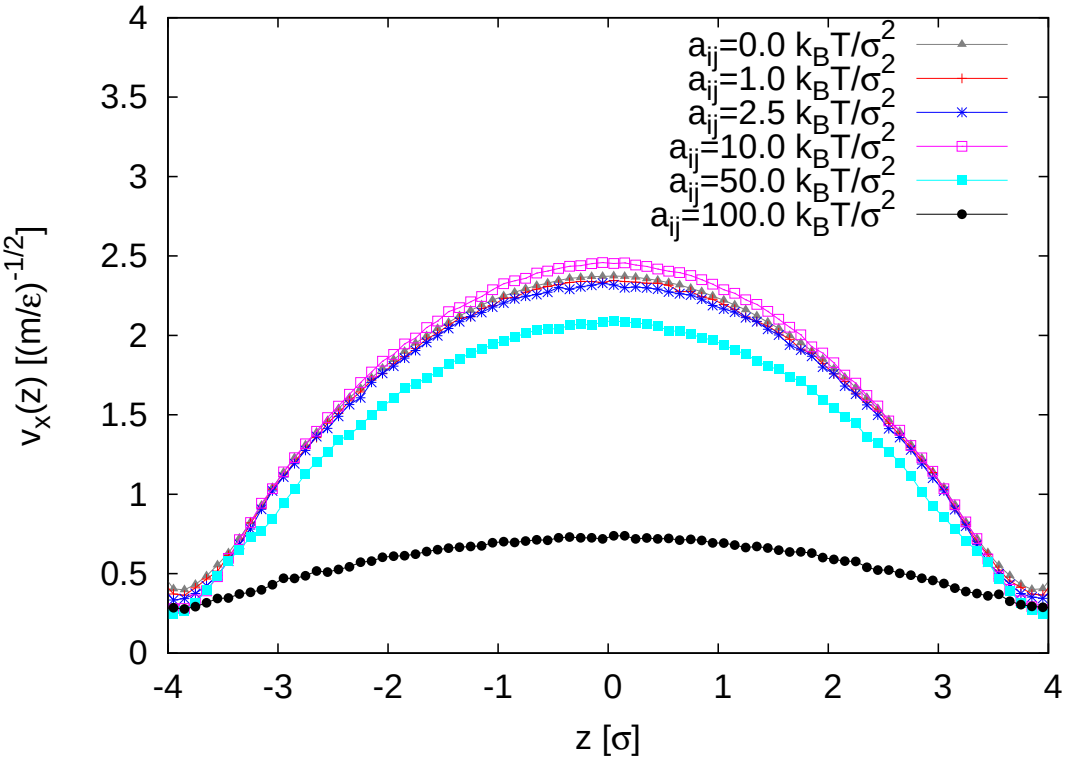

Figure D.1: Plane Poiseuille Flow profiles for an external force of $F_x = 0.1 k_B T/\sigma$, friction coefficient $\gamma_{DPD} = 5.0\sigma^{-1}(m\epsilon)^{1/2}$, fluid density $\rho = 3.75\sigma^{-3}$ and varying prefactors of the conservative force a_{ij}.

viscosity in [18] by Eqn. (3.20), it is obvious that the conservative interactions change the homogeneous density which directly influences the dissipative and kinetic contributions of the shear viscosity (Fig. (3.5)). Thus the pair distribution cannot be assumed as constant and has to be replaced in lowest order by Meyer's f-function to

$$f^{(2)} = \exp(-U(r_{ij})/k_B T) - 1 \tag{D.1}$$

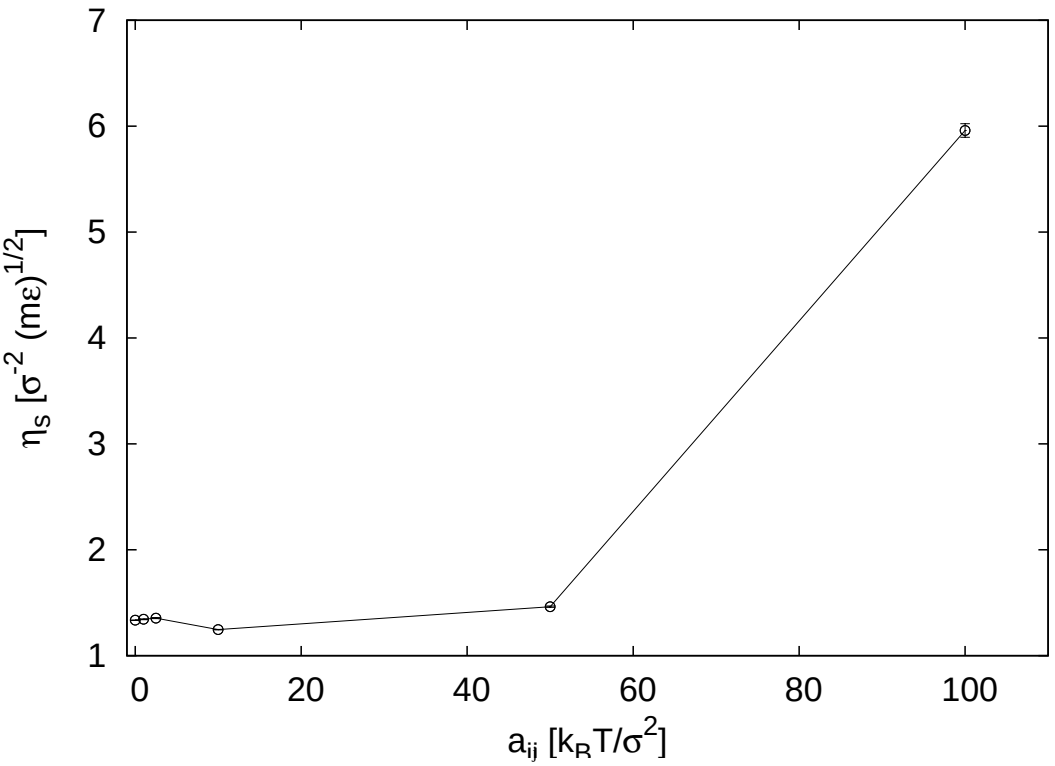

Figure D.2: Shear viscosities η_s for the flow profiles of Fig. D.1 measured by the amplitude of the Plane Poiseuille Flow.

with the potential energy $U(r_{ij})$, respectively higher order Ornstein-Zernicke equations [139]. An investigation of the conservative interactions on the hydrodynamic boundaries and the detailed explanation in terms of an analytical theory is work in progress [75].

Bibliography

[1] Viovy J.-L., *Rev. Mod. Phys.* **72**, 813 (2000)

[2] Beyer H., Walter W., *Lehrbuch der Organischen Chemie*, Hirzel Verlag Stuttgart, reprint (1984)

[3] Manning G. S., *J. Phys. Chem.* **85**, 1506 (1981)

[4] Barrat J.-L., Joanny J. F., *J. F. Adv. Chem. Phys.* **XCIV**, 1, (1996)

[5] Frenkel D., Smit B., *Understanding molecular simulation*, Academic Press, Orlando (2001)

[6] Mathe J., Di Meglio J. -M., Tinland B., *J. Colloid Interface Sci.* **316**, 831 (2007)

[7] Doi M., Edwards S. F., *The Theory of Polymer Dynamics*, Oxford Science Publications, Clarendon Press, Oxford (1986)

[8] Ermak D. L., McCommon J. A., *J. Chem. Phys.* **69**, 1352 (1978)

[9] Rotne J., Prager S., *J. Chem. Phys.* **50**, 4831 (1969)

[10] Yamakawa H., *J. Chem. Phys.* **53**, 436 (1970)

[11] Frisch U., Hasslacher B., Pomeau Y., *Phys. Rev. Lett.* **56**, 1505 (1986)

[12] McNamara G. R., Zanetti G., *Phys. Rev. Lett.* **61**, 2332 (1988)

[13] Benzi R., Succi S., Vergassola M., *Phys. Rep.* **22**, 145 (1992)

[14] Chen S., Doolen G. D.,*Annu. Rev. Fluid. Mech.* **30**, 329 (1998)

[15] Hoogerbrugge P. J., Koelman J. M. V. A., *Europhys. Lett.* **19**, 155, (1992)

[16] Koelman J. M. V. A., Hoogerbrugge P. J, *Europhys. Lett.* **21**, 363 (1993)

[17] Español P., Warren P. B., *Europhys. Lett.* **30**, 191 (1995)

[18] Groot R. D., Warren P. B., *J. Chem. Phys.* **107**, 4423 (1997)

[19] Malevanets A., Kapral R., *J. Chem. Phys.* **110**, 8605 (1999)

[20] Malevanets A., Kapral R., *J. Chem. Phys.* **112**, 7260 (2000)

[21] Warren P. B., *Curr. Op. Coll. Interf. Sci.* **3**, 620 (1998)

[22] Diu B., Guthmann C., Lederer D., Roulet B., *Grundlagen der statistischen Physik*, De Gruyter Verlag, Berlin (2000)

[23] Smiatek, J., *Untersuchung von Simulationsmethoden zur stochastischen Dynamik mit Zwangsbedingungen*, Staatsexamensarbeit, Universität Bielefeld (2005)

[24] van Kampen N. G., *Stochastic Processes in Physics and Chemistry*, NH Elsevier, Amsterdam (2003)

[25] Risken H., *The Fokker-Planck equation*, Springer Verlag, Berlin (1986)

[26] Ahlrichs P., Dünweg B., *J. Chem. Phys.* **111**, 8225 (1999)

[27] Bhatnagar, P. L., Gross E. P., Krook M., *Phys. Rev.* **94**, 511 (1954)

[28] Qian, Y. H., D'Humieres D., Lallemand P., *Europhys. Lett.* **17**, 479 (1992)

[29] Ahlrichs P., Dünweg B.,*Int. J. Mod. Phys. C***9**, 1429 (1998)

[30] Allen M. P., Tildesley D. J., *Computer Simulation of Liquids*, Oxford Science Publications, Oxford (1987)

[31] Ewald P., *Ann. Phys.* **64**, 253 (1921)

[32] Deserno M., Holm C., *J. Chem. Phys.* **109**, 7678 (1998)

[33] Hockney R. W., Eastwood J. W., *Computer simulation using Particles*, McGraw-Hill, New York (1981)

[34] Strebel R., *Pieces of software for the Coulombic m body problem*, Dissertation 13504, ETH Zürich (1999)

[35] Sperb R., *Mol. Simulation* **13**, 189 (1994)

[36] Strebel R., Sperb R., *Mol. Simulation* **27** 61, (2001)

[37] Arnold A., Holm C., *Comp. Phys. Comm.* **148**, 327 (2002)

[38] Arnold A., Holm C., *Chem. Phys. Lett.* **354**, 324 (2002)

[39] Arnold A., de Joannis J., Holm C., *J. Chem. Phys.* **117**, 2496 (2002)

[40] Arnold A., Holm C., *J. Chem. Phys.* **123**, 144103 (2005)

[41] Brödka A, *J. Chem. Phys.* **125**, 107103 (2005)

[42] ESPResSo-Homepage, http://www.espresso.mpg.de (2002-2009).

[43] Arnold A., Mann B. A., Limbach H. -J., Holm C., in *Forschung und wissenschaftliches Rechnen 2003*, Vol. 63 of *GWDG-Bericht*, edited by K. Kremer and V. Macho (Gesellschaft für wissenschaftliche Datenverarbeitung mbh, Göttingen, Germany, 2004), pp. 43–59.

[44] Arnold A., Mann B. A., Limbach H. -J., Holm C., *Comp. Phys. Comm.* **174**, 704 (2005)

[45] TCL/TK Homepage: http://tcl.activestate.com (2009)

[46] Duong-Hong D., Phan-Thien N., Fan, X. J., *Comp. Mech.* **35**, 24, (2004)

[47] Qiao R., Aluru N. R., *J. Chem. Phys.* **118**, 4692 (2003)

[48] Reproduced from: Duong T. T., Streek M., Ros R., Schmid F., Brugger J., Anselmetti D., Ros A., *Microelectronic Engineering* **67-68**, 905 (2003)

[49] Lu P. -C., *Introduction to the mechanics of viscous fluids* Holt, Rinehart and Winston Inc., New York (1973)

[50] Landau D. L., Lifshitz E. M., *Hydrodynamik. Lehrbuch der theoretischen Physik Vol. 6* 6. Auflage, Deutsch Verlag, Franfurt am Main (2007)

[51] Navier C., *Mem. Acad. Sci. Ins. Fr.* **6**, 389 (1823)

[52] Maxwell J. C., *Philos. Trans. Soc. London* **170**, 231 (1867)

[53] Kennard E. H., *Kinetic theory of gases*, McGraw-Hill, New York (1938)

[54] Vincenti W. G., Kruger C. H., *Introduction to physical gas dynamics*, Second edition, Wiley, New York (1967)

[55] Pit R., Hervet H., Leger L., *Phys. Rev. Lett.* **85**, 980 (2000)

[56] Tretheway D., Meinhart C., *Physics of Fluids* **14**, 9 (2002)

[57] Neto C., Evans D. R., Bonaccurso E., Butt H.-J., Craig V. S. J., *Rep. Prog. Phys.* **68**, 2859 (2005)

[58] Bocquet L., Barrat J. -L., *Phys. Rev. E* **49**, 3079 (1994)

[59] Harting J., Kunert C., Hermann H. J., *Europhys. Lett.* **75**, 328 (2006)

[60] Kunert C., Harting J., *Phys. Rev. Lett.* **99**, 176001 (2007)

[61] Kunert C., Harting J., *Prog. Comp. Fluid Dynamics* **8**, 197 (2008)

[62] Neto C., Craig V., Williams D., *Eur. Phys. J. E* **12**, 71 (2003)

[63] Zhu Y., Granick S., *Phys. Rev. Lett.* **87**, 096105 (2001)

[64] Zhu Y., Granick S., *Langmuir* **18**, 10058 (2002)

[65] Barrat J.-L., Boquet L., *Soft Matter* **3**, 685 (2007)

[66] Boek E. S., Conveney P. V., Lekkerkerker H. N. W., van der Schoot P., *Phys. Rev. E* **55**, 3124 (1997)

[67] Pivkin I. V., Karniadakis G. E., *J. Comput. Phys.* **207**, 114 (2005)

[68] Revenga M., Zuniga I., Español P., *Comp. Phys. Comm.* **121-122**, 309 (1999)

[69] Revenga M., Zuniga I., Español P., Pagonabarraga I., *Int. J. Mod. Phys. C* **9**, 1319 (1998)

[70] Smiatek J., Allen M. P., Schmid F., *Eur. Phys. J. E* **26**, 115 (2008)

[71] ESPResSo User's Guide, *Tunable-slip boundary interaction*, http://espressowiki.mpip-mainz.mpg.de/espresso/ug.pdf (2008)

[72] Dünweg B., *J. Chem. Phys.* **99**, 6977 (1993)

[73] Weeks J. D., Chandler D., Andersen H. C., *J. Chem. Phys.* **54**, 5237 (1991)

[74] Stark H., *Physik Journal* **6**, 31 (2007)

[75] Theis T., Smiatek J., Schmid F., work in progress

[76] Marsh C. A., Backx G., Ernst M. H. E., *Phys. Rev. E* **55**, 1676 (1997)

[77] Backer J. A., Lowe C. P., Hoefsloot H. C. J., Iedema P. D., *J. Chem. Phys.* **122**, 154503 (2005)

[78] Schiller U. D., *Dissipative Particle Dynamics - A study of the methodological background*, Diploma Thesis, Bielefeld University (2005)

[79] Ripoll M., Ernst M. H., Español P.,*J. Chem. Phys.* **115**, 7271 (2001)

[80] Ripoll Hernando M. S., *Kinetic Theory of Dissipative Particle Dynamics Models*, Dissertation, Universidad Nacional de Educacion a Distancia Madrid (2002)

[81] Allen M. P., private communication (2006)

[82] Israelachvili J., *Intermolecular and Surface Forces*, Academic Press, London (1991)

[83] Atkins P. W., *Physikalische Chemie*, 3. Edn., Wiley-VCH, Weinheim (2001).

[84] Hunter R. J., *Foundations of Colloid Science*, Clarendon Press, Oxford (1991)

[85] Lyklema J., *Fundamentals of Interface and Colloid Science*, Academic Press, New York (1995)

[86] Lyklema J., Minor M., *Colloids Surf. A* **140**, 33 (1998)

[87] Andelman D., *Proceedings of the Nato ASI and SUSSP on soft condensed matter physics in molecular and cell biology (2005)*, pp. 97 ff. Poon W., Andelman D. Eds., Taylor and Francis, New York (2006)

[88] Jackson J. D., *Classical Electrodynamics*, 3. Edn., Wiley, New York (1999)

[89] Fogolari F., Brigo A., Molinari H., *J. Mol. Recognit.* **15**, 377 (2004)

[90] Engström S., Wennerström H., *J. Chem. Phys.* **82**, 2711 (1978)

[91] Bronstein I. N., Semendjajew K. N., Musiol G., Mühlig H., *Taschenbuch der Mathematik*, 6. Auflage, Verlag Harri Deutsch, Berlin (2005)

[92] Netz R. R., Orland H., *Eur. Phys. J. E* **1**, 67 (2000)

[93] Moreira A. G., Netz R. R., *Phys. Rev. Lett.* **87**, 078301 (2001)

[94] Moreira A. G., Netz R. R., *Europhys. Lett.* **52**, 705 (2000)

[95] Boroudjerdi H., Kim Y. -W., Naji A., Nety R. R., Schlagberger X., Serr A., *Phys. Rep.* **416**, 129 (2005)

[96] Paul W., Baschnagel J., *Stochastic processes: from physics to finance*, Springer Verlag, Berlin (1999)

[97] Joly L., Ybert C., Trizac E., Bocquet L., *Phys. Rev. Lett.* **93**, 257805 (2004)

[98] Netz R. R.,*Phys. Rev. Lett.* **91**, 1381011 (2003)

[99] Hatlo M. M., Lue L., arXiv:0806.3716v1 [cond-mat.soft] (2008)

[100] Burak Y., Andelman D., Orland H., *Phys. Rev. E* **70**, 016102 (2004)

[101] Smiatek J., Sega M., Holm C., Schiller U. D., Schmid F., *Mesoscopic simulations of the counterion-induced electroosmotic flow - a comparative study*, to be published (2009)

[102] Burmeister M., Ulanovsky L., *Pulsed-Field Gel Electrophoresis: Protocols, Methods and Theories*, Humana Press, Totowa (1992)

[103] Bakajin O., Duke T. A. J., Tegenfeldt J., Chou C.-F., Chan S. S., Austin R. H., Cox E. C., *Anal. Chem.* **73**, 6053 (2001)

[104] Zimm B. H., *J. Chem. Phys.* **24**, 269 (1956)

[105] Flory P. J., *Statistical mechanics of macromolecules*, Oxford Science Publications, Clarendon Press, Oxford (1956)

[106] Dobrynin A. V., Colby R. H., Rubinstein M., *Macromolecules* **28**, 1859 (1995)

[107] Dobrynin A. V., Rubinstein M., *Prog. Polym. Sci.* **30**, 1049 (2005)

[108] de Gennes P. -G., *Macromolecules* **9**, 587 (1976)

[109] de Gennes P. -G., *Macromolecules* **9**, 594 (1976)

[110] Odijk T., *J. Polym. Sci. Polym. Phys. Ed.* **15**, 477 (1977)

[111] Skolnik J., Fixman M., *Macromolecules* **10**, 944 (1977)

[112] Rouse P. E., *J. Chem. Phys.* **21**, 1272 (1953)

[113] Long D., Ajdari A., *Europ. Phys. J. E* **4**, 29 (2001)

[114] Richter D., *Polymer Dynamics* in *Soft Matter - Complex Materials on Mesoscopic Scales*, Lecture manuscripts of the 33th. IFF winter school, Reihe Matter and Materials **10** (2002)

[115] Dünweg B., Kremer K., *J. Chem. Phys.* **99**, 6983 (1993)

[116] Dünweg B., Grest G. S., Kremer K.,*Molecular Dynamics simulations of polymer systems* in *Numerical Methods for Polymeric Systems*, IMA Volumes in Mathematics and its Applications 102, Springer Verlag, Berlin (1998)

[117] de Gennes P. -G., *Scaling concepts in polymer physics*, Cornell press, Ithaca (1979)

[118] Ahlrichs P., Everaers R., Dünweg B., *Phys. Rev. E* **64**, 040501(R) (2001)

[119] Muthukumar M., *J. Chem. Phys.* **107**, 2619 (1997)

[120] Lide D. R., *CRC Handbook of Chemistry and Physics*, 70th ed., CRC Press, Boca Raton (1990)

[121] Petrov E. P., Ohrt T., Winkler R. G., Schwille P., *Phys. Rev. Lett.* **97**, 258101 (2006)

[122] Shusterman R., Alon S., Gavrinyov T., Krichevsky O., *Phys. Rev. Lett.* **92**, 0483031 (2004)

[123] Grosberg A. Y., Khokhlov A. R., *Statistical Physics of Macromolecules*, Springer Verlag, Berlin (1997)

[124] Kremer, K., Grest, G. S., *J. Chem. Phys.* **92**, 5057 (1990)

[125] Grass K., Böhme U., Scheler U., Cottet H., Holm C., *Phys. Rev. Lett.* **100**, 096104 (2008)

[126] Frank S., Winkler R. G., *Europhys. Lett.* **83**, 38004 (2008)

[127] Streek, M., Schmid, F., Duong, T. T., Ros, A., *Phys. Rev. E* **71**, 11905 (2005)

[128] Streek, M., Schmid, F., Duong, T. T., Ros, A., *J. Biotechnology* **112**, 79 (2004)

[129] Roeraade M., Stjernström M., International Patent WO/1997/26531, 1997, avaible at *http://www.wipo.int*

[130] Iki N., Kim Y., Yeung E. S., *Anal. Chem.* **68**, 4321 (1996)

[131] Long D., Viovy J.-L., Ajdari A., *Phys. Rev. Lett.* **76**, 3858 (1996)

[132] Cannavacciuolo L., Winkler R. G., Gompper G., *Europhys. Lett.* **83**, 34007 (2008)

[133] Regtmeier J., Duong T. T., Eichhorn R., Anselmetti D., Ros A., *Anal. Chem.* **79**, 3925 (2007)

[134] Smiatek J., unpublished

[135] Meinhardt S., *Chiral separation of molecules in microfluidic devices*, Diploma thesis, Universität Bielefeld (2008)

[136] Wolfram S.,*Das Mathematica© Buch*, 3. Auflage, Addison-Wesley Verlag, Bonn (1997)

[137] http://functions.wolfram.com

[138] Smiatek J., Schmid F., arXiv:0809.5239v1 [cond-mat.soft] (2008)

[139] Hansen J. P., McDonald I. R., *Theory of simple liquids*, Academic Press, London (1976)

Through the darkness of the future past
The magician longs to see
One chants out between two worlds:
Fire walk with me.

Twin Peaks (1991)

Danksagung

An dieser Stelle möchte ich einigen Personen und Orginsationen danken, die diese Arbeit nachhaltig unterstützt haben.
Frau Prof. Dr. Friederike Schmid, für die Bereitstellung des Themas, ihr stetes Interesse am Fortschritt der Arbeit, ihre Motivation und ihr Einsatz, vor allem bei den analytischen Resultaten dieser Arbeit und ihr offenes Ohr bei allen Fragen und Problemen.
Herrn Prof. Dr. Peter Reimann, für die freundliche Übernahme des Zweitgutachtens.
Ulf D. Schiller, Burkhard Dünweg, Marcello Sega, Christian Holm und Kai Grass, für die vielen anregenden Diskussionen, die wunderbare Zusammenarbeit und die Einladungen an das Max-Planck Institut für Polymerphysik in Mainz und an das Frankfurt Institute for Advanced Research.
Herrn Prof. Dr. Michael P. Allen, für die wertvollen Hinweise auf die Bedeutung der hydrodynamischen Randbedingungen und sein Interesse an dieser Thematik.
Frau Hanne Litschewsky, für ihre schnelle Hilfe bei organisatorischen und bürokratischen Angelegenheiten.
Der Arbeitsgruppe der Theorie der Kondensierten Materie an der Universität Bielefeld und insbesondere Beate West, Martin Weinhold und Thorsten Bogner für die angenehme Arbeitsatmosphäre.
Sebastian Meinhardt und Tatiana Theis, für ihre Motivation und Diskussionsbereitschaft.
Der Volkswagen Stiftung, für die finanzielle Unterstützung im Rahmen des Projektes *Novel Simulation Methods for Electrohydrdynamics* (I/80431).
Den Entwicklern des ESPResSo-Programmpaketes für die geleistete Vorarbeit.
Dem Paderborn Center for Parallel Computing (PC2), dem NIC Computer Center in Jülich, Prof. Dr. Jürgen Schnack und den Rechnern an der Universität Osnabrück und dem HLRS in Stuttgart, auf deren Rechnern ein Grossteil der Simulationen und der anschliessenden Analysen durchgeführt wurde.
Jan Christoph Schöning, Caterina Bentele und meinem Cousin Mark Spicer, für ihre Bereitschaft und Mühe diese Arbeit genau unter die Lupe zu nehmen.
Meinen Eltern, ohne deren liebe Hilfe und Unterstützung diese Arbeit überhaupt nicht entstanden wäre.
Steffi, für all ihre Liebe und ihr Verständnis. Für die Vergangenheit, Gegenwart und die Zukunft. Ohne Dich kann ich mir ein Leben nicht vorstellen.

Hiermit versichere ich, Jens Smiatek, geb. am 13. 04. 1978 in Lemgo, die vorliegende Arbeit selbständig angefertigt zu haben und keine anderen Hilfsmittel als die angegebenen verwendet zu haben.
Alle Stellen, die dem Wortlaut oder dem Sinne nach anderen Werken entnommen sind, habe ich in jedem Falle unter genauer Angabe der Quelle deutlich als Entlehnung kenntlich gemacht.
Die Berechnungen in den Anhängen A und C, ausser der Herleitung von Gleichung (3.30), wurden ausschliesslich von Frau Prof. Dr. Friederike Schmid durchgeführt bzw. entwickelt.

Bielefeld, den 28. Januar 2009